

AD-A 117435

LIBRARY  
RESEARCH REPORTS DIVISION  
NAVAL POSTGRADUATE SCHOOL  
MONTEREY, CALIFORNIA 93940

NRL Memorandum Report 4808

## **A Synchronous Phase-Detection System for an Optical Interferometric Sensor**

I. J. BUSH

*Development Section  
Transducer Branch  
Underwater Sound Reference Detachment  
P.O. Box 8337  
Orlando, Fl 32856*

**May 15, 1982**



**NAVAL RESEARCH LABORATORY**  
Washington, D.C.

Approved for public release; distribution unlimited.

UNCLASSIFIED

SECURITY CLASSIFICATION OF THIS PAGE (When Data Entered)

REPORT DOCUMENTATION PAGE		READ INSTRUCTIONS BEFORE COMPLETING FORM
1. REPORT NUMBER NRL MEMORANDUM REPORT 4808	2. GOVT ACCESSION NO.	3. RECIPIENT'S CATALOG NUMBER
4. TITLE (and Subtitle) (U) A SYNCHRONOUS PHASE DETECTION SYSTEM FOR AN OPTICAL INTERFEROMETRIC SENSOR		5. TYPE OF REPORT & PERIOD COVERED Interim report on a continuing problem
		6. PERFORMING ORG. REPORT NUMBER
7. AUTHOR(s)  I. J. Bush		8. CONTRACT OR GRANT NUMBER(s)
9. PERFORMING ORGANIZATION NAME AND ADDRESS Underwater Sound Reference Detachment Naval Research Laboratory PO Box 8337, Orlando, FL 32856		10. PROGRAM ELEMENT, PROJECT, TASK AREA & WORK UNIT NUMBERS 62711N RF11-125-800 F101-A
11. CONTROLLING OFFICE NAME AND ADDRESS Physical Acoustics Branch Naval Research Laboratory Washington, DC 20375		12. REPORT DATE May 15, 1982
		13. NUMBER OF PAGES 77
14. MONITORING AGENCY NAME & ADDRESS (if different from Controlling Office)		15. SECURITY CLASS. (of this report)  UNCLASSIFIED
		15a. DECLASSIFICATION/DOWNGRADING SCHEDULE
16. DISTRIBUTION STATEMENT (of this Report) Approved for public release; distribution unlimited.		
17. DISTRIBUTION STATEMENT (of the abstract entered in Block 20, if different from Report)		
18. SUPPLEMENTARY NOTES Work was sponsored by the FOSS Program of ONR via NRL's Physical Acoustics Branch, Dr. J. A. Bucaro.		
19. KEY WORDS (Continue on reverse side if necessary and identify by block number) Synchronous interferometric sensor Interferometric measurement system Active interferometric stabilization		
20. ABSTRACT (Continue on reverse side if necessary and identify by block number) A system has been developed to accurately detect phase produced in optical in- terferometric sensors. The system employs optical heterodyning, and it synchronously detects optical phase by feeding an error signal back to a phase modulator in the reference leg of the interferometer. This system is seen to have properties similar to a phase-locked loop used for the demodulation of FM signals. The system model is second order and nonlinear, but a linear approxi- mation serves to accurately describe the system in synchronous operation and (over)		

UNCLASSIFIED

SECURITY CLASSIFICATION OF THIS PAGE (When Data Entered)

20. ABSTRACT (cont'd.)

is corroborated with well-matched empirical data. The complete model is simulated via computer techniques and is needed to describe the system's parameters that lead to loss and reacquisition of synchronization.

UNCLASSIFIED

SECURITY CLASSIFICATION OF THIS PAGE(When Data Entered)

## CONTENTS

REVIEW OF INTERFEROMETRIC SENSORS . . . . .	1
General Interferometric Phase Measurement . . . . .	1
Fiber-Optic Interferometric Sensors . . . . .	3
<u>The Acoustic Sensor</u> . . . . .	3
<u>The Rate Gyroscope</u> . . . . .	3
SYSTEM DESCRIPTION AND OPERATION . . . . .	7
System Introduction . . . . .	7
System Operation . . . . .	8
Optical Modulation . . . . .	12
<u>Bragg Diffraction</u> . . . . .	12
<u>Optical Phase Modulation</u> . . . . .	13
LINEAR ANALYSIS . . . . .	14
The Model . . . . .	14
<u>General Development</u> . . . . .	14
<u>Linearization of the Model</u> . . . . .	20
Application and Verification of the Linear Model . . . . .	23
<u>System Analysis</u> . . . . .	23
<u>Verification of the Linear Model</u> . . . . .	30
<u>The Solution to the Step Response and Its</u> <u>Effects on System Damping</u> . . . . .	32
A Compensation Technique for Increasing System Damping When Large Loop Gains are Involved . . . . .	38
NONLINEAR ANALYSIS . . . . .	46
The Nonlinear Model Approximated with Discrete Modeling . . . . .	47
<u>Development of the Nonlinear Discrete Model</u> . . . . .	47
Verification of the Nonlinear Discrete Model . . . . .	48

CONTENTS (cont'd.)

Application of the Nonlinear Discrete Model . . . . .	58
<u>The Step Response</u> . . . . .	58
<u>The Ramp Response</u> . . . . .	58
<u>The Sinusoidal Response</u> . . . . .	68
CONCLUDING REMARKS . . . . .	71
REFERENCES . . . . .	72

# A SYNCHRONOUS PHASE-DETECTION SYSTEM FOR AN OPTICAL INTERFEROMETRIC SENSOR

## REVIEW OF INTERFEROMETRIC SENSORS

### General Interferometric Phase Measurement

Real time measurement of optical phase fluctuations provides information in the areas of: 1) measuring refractive index variations in plasmas or gasses, 2) fiber-optic sensors used for hydroacoustic sensing, and 3) fiber-optic sensors used for determining rates of rotation.

All of these processes involve interferometric detection of optical phase to produce the measurement. A schematic representation of a Mach-Zehnder interferometer [1] is shown in Fig. 1. Light from a single frequency laser is split up into two beams via beamsplitter BS 1. The upper beam is denoted as the signal leg while the lower beam inherits the name of reference leg. The sensor leg experiences optical phase modulation while the reference leg maintains a constant optical phase. The two optical beams are recombined with beamsplitter BS 2, and the interference pattern is detected with an optical "square-law" detector. If assumptions of collinear, plane-wave propagation and parallel polarizations for the recombined beams are made, the output of the detector (current or voltage response) produces a signal  $s(t)$  that is proportional to the relative optical phase difference between the signal and reference legs of the interferometer.

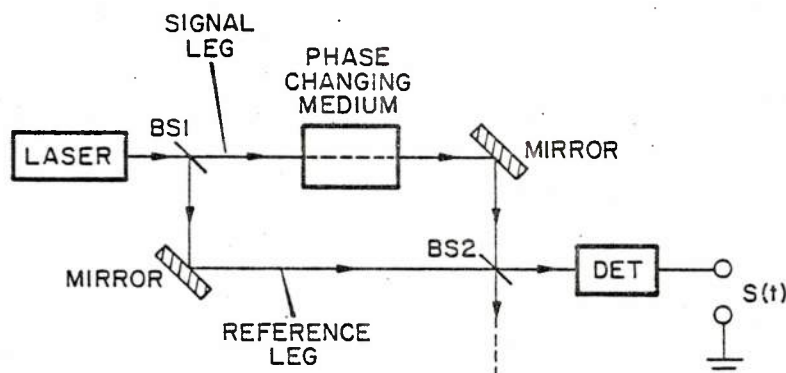


Fig. 1 - Mach-Zehnder interferometric system used to  
measure optical phase modulation

-----  
*Manuscript submitted February 22, 1982*

To quantitatively determine how the detector output signal is proportional to the relative phase difference of the two optical signals, consider the following simple mathematical model for the interferometer shown in Fig. 1.

If the laser produces a plane-wave, single frequency, longitudinal beam, then the electric fields for the signal and reference legs may be expressed respectively:

$$\bar{E}_s = E_s \exp\{i[\omega t - kz + \theta_{s1} + \theta_i(t) + \theta_{n1}(t)]\}$$

and

(1)

$$\bar{E}_r = E_r \exp\{i[\omega t - kz + \theta_{s2} + \theta_{n2}(t)]\},$$

where both beams are assumed to be propagating in the z direction with electric field amplitudes  $E_s$  and  $E_r$  where

$k$  = wave number of the optical frequency

$\theta_{s1}$  = static phase shift produced by the optical path length of the signal leg

$\theta_{s2}$  = static phase shift produced by the optical path length of the reference leg

$\theta_i(t)$  = phase modulation produced by the signal source

$\omega_o$  = optical radian frequency

$\theta_{n1}(t)$  = any noise phase produced by the signal leg

$\theta_{n2}(t)$  = any noise phase produced by the reference leg.

The optical detector is modeled as a "square-law" device that produces signal output  $s(t)$  proportional to the incident power of the electric field. In the case of the interferometer in Fig. 1, the incident field  $\bar{E}_i$  is composed of the vector sum of the fields from the sensor and the reference leg or

$$\bar{E}_i = \bar{E}_s + \bar{E}_r. \quad (2)$$

If  $\bar{E}_s$  and  $\bar{E}_r$  are assumed to be linearly polarized in the same direction, the power of the incident field is linearly proportional to  $|\bar{E}_i|^2$  and the detected output  $s(t)$  is linearly proportional to the field power or

$$s(t) \propto |\bar{E}_i|^2 = \bar{E}_i \bar{E}_i^*, \quad (3)$$



where \* represents the complex conjugate. After some algebraic manipulations and the use of Euler's formula, Eq. (3) results in

$$s(t) = K\{E_r^2 + E_s^2 + 2E_r E_s \cos[\theta_s + \theta_i(t) + \theta_n(t)]\}, \quad (4)$$

where K is a constant of proportionality relating to the efficiency of the detector. The term  $\theta_s$  represents the difference between the static-phase terms ( $\theta_s = \theta_{s1} - \theta_{s2}$ ) while the term  $\theta_n(t)$  represents the difference between the noise-phase terms [ $\theta_n(t) = \theta_{n1}(t) - \theta_{n2}(t)$ ].

Inspection of Eq. (4) shows that the output of the simple passive interferometer in Fig. 1 produces a signal output that is a nonlinear function of  $\theta_i(t)$ ,  $\theta_n(t)$ , and  $\theta_s$ . It is also a function of  $E_r$  and  $E_s$ . The idea behind the interferometer is to measure  $\theta_i$ . The rest of the terms serve to obfuscate this measurement of  $\theta_i$ ; these terms will be discussed individually.

The field amplitude terms  $E_r$  and  $E_s$  are seen to vary as the laser intensity varies. They also may vary as a function of variable interferometer attenuation. The static phase  $\theta_s$  is a constant and generally takes on a value of  $0 - 2\pi$  with a uniform probability. The noise phase  $\theta_n(t)$  will be seen to vary from interferometer to interferometer. For Mach-Zehnder interferometers, the thermal expansion and contraction of materials is usually the term manifest in producing  $\theta_n(t)$ , which can generally be assumed to be a random variable. In summary, the simple passive interferometric phase-measurement process is nonlinear, subject to two random variables in phase and unable to distinguish the difference between wavefront and field-amplitude variations.

## Fiber-Optic Interferometric Sensors

The scope of interferometric systems discussed in this report will be limited to that of fiber-optic sensors. The two most common fiber-optic sensors are the acoustic sensor [2,3] and the rate gyroscope [4,5]. The basic concepts of these two sensors are described in the following passages.

### The Acoustic Sensor

The basic configuration of the fiber-optic acoustic sensor is shown schematically in Fig. 2. This diagram is seen to be very similar to the general Mach-Zehnder interferometer shown in Fig. 1. Light from a laser is split up by beamsplitter BS 1 and is coupled into single-mode fibers via proper focusing optics (generally microscope objectives for a laboratory setup). The upper leg is the signal leg and is comprised of a coil of fiber generally 10- to 100-m long rolled up into a "sensing coil" so as to be compact enough to be much smaller in diameter than the acoustic wavelengths of interest (to be detected). The lower leg is the reference leg and is generally a piece of fiber as long as the sensor leg (unless



the laser has an unusually long coherence length) as to match its optical path length. The beams are coupled out of the fibers and recollimated via the proper optics and recombined with beamsplitter BS 2 to produce an interference pattern on the detector. If it is assumed that the light in the fiber is propagating single mode ( $HE_{11}$ ) and the cladding modes are stripped off along with all the preliminary assumptions leading up to the development of Eq. (4), the phase terms describing the input signals and the noise signals may be defined. The static phase term  $\theta_s$  may be arbitrarily assumed to be 0. The input phase term  $\theta_i(t)$  is described as

$$\theta_i(t) = \left[ \left( \frac{dn}{dP} \right) + \frac{n}{l} \left( \frac{dl}{dP} \right) \right] k l P(t), \quad [6] \quad (5)$$

where  $l$  is the length of the fiber exposed to the sound field,  $n$  is the effective refractive index of the single-mode fiber,  $k$  is the optical wave number,  $P$  represents static pressure, and  $P(t)$  represents the acoustic pressure to which the fiber is subjected. This relationship assumes that the sensing coil's largest dimension (generally the diameter) is much smaller than the acoustic wavelength. The bracketed term represents the effective index change for a 1-meter (or unity length, depending on the convention used) piece of fiber exposed to a static pressure. The first term in the brackets describes the true index change or dispersion resulting from the incident pressure while the second term relates the length change of the fiber (as a function of pressure) to the effective index change.

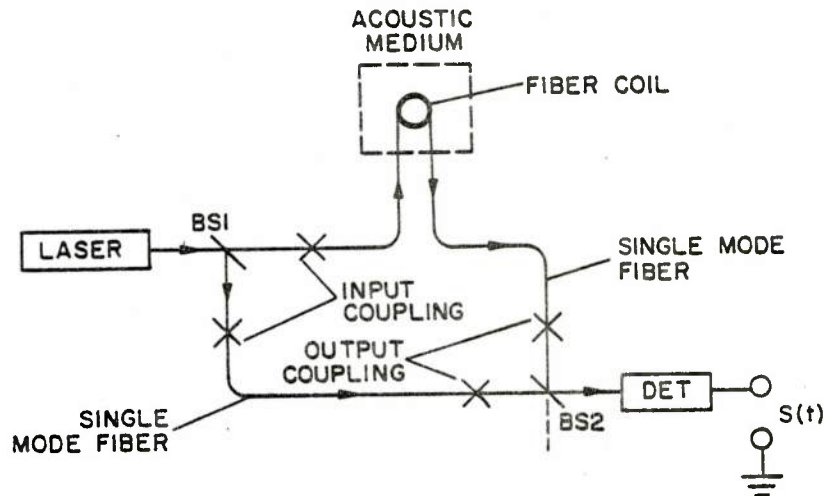


Fig. 2 - Basic configuration for fiber-optic acoustic sensor

The system noise may be represented with both amplitude and phase terms. The amplitude noise is manifested in the  $E_r$  and  $E_s$  terms of Eq. (4) and is either a function of the shot, intermodulation, or spontaneous emission noise from the laser or the shot, thermal (Johnson), or dark current produced by the photodetector. These "noise floor" terms are of little significance when considering the functional operation of the acoustic sensor (albeit it does represent the minimum detectable signal level). The phase noise of the system primarily consists of three components: 1) phase noise produced by acoustic background noise, 2) phase noise produced by a path length mismatch resulting in loss of coherence, and 3) phase noise resulting from temperature fluctuations. The first two terms are basically "noise floor" type phenomenon; and if certain precautions are taken in the laboratory (or setup), these terms do not greatly inhibit system operation. The third term (thermal-induced phase fluctuation), is capable of producing very large phase shifts. In fact, it is not uncommon to see phase shifts of approximately 500 rads/m °C in jacketed fiber [7,8]. This number is deduced by taking Hockers bare fiber number and multiplying by a scaler described by Tateda to generalize the jacketed fiber. This thermal-phase noise, because of its large magnitude, poses a problem in the passive interferometric detection shown in Fig. 2. As was discussed in an earlier section of this chapter, the detected acoustic phase (of a relatively small magnitude) will become a nonlinear function of thermal-induced noise phase [as seen in Eq. (4)].

### The Rate Gyroscope

The basic configuration of the fiber-optic rate gyroscope is shown schematically in Fig. 3. This interferometer will produce a phase shift (via the sagnac effect) that is a function of rotation rate  $\Omega$  of the sensor. Equal, nonreciprocal phases (of equal magnitude and opposite sign) are induced in the two counter-propagating beams in the fiber and are seen to be proportional to the area  $A$  of the coil, the number of fiber loops  $N$  that comprise the coil, and the angular rotation rate  $\Omega$  of the coil expressed in rads/s. The phase shift  $\phi$  measured by the interferometer may be expressed as

$$\phi = \mu NA\Omega. \quad (6)$$

The coefficient  $\mu$  is a constant of proportionality and is equal to  $4/\lambda c$ , where  $\lambda$  is the vacuum wavelength and  $c$  is the vacuum speed of light [9]. Equation (7) is an ideal relationship and assumes a circular loop and col-linear polarization between the two counter-propagating beams (so that the fiber birefringence does not alter the expression).

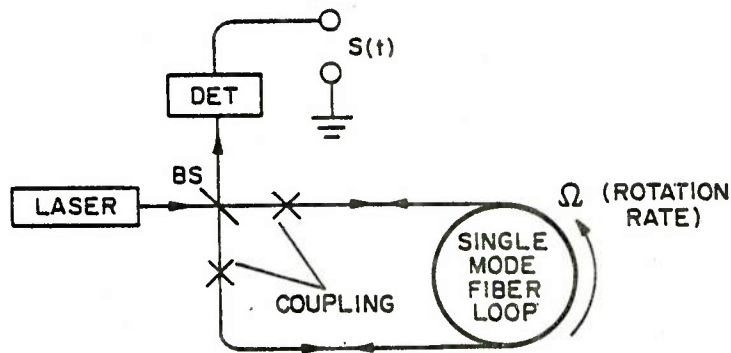


Fig. 3 - Basic configuration for fiber-optic rotational rate sensor

It is possible to model the rotational rate sensor with the general interferometer, Eq. (4). The phase shift  $\phi$  related to the rotation rate represents the input signal  $\theta_i(t)$ . The static phase  $\theta_s$  will be zero as there is no path length mismatch. The field amplitudes  $E_r$  and  $E_s$  will be a function of the laser output power and the input coupling efficiencies. The phase noise sources for the rate gyro will be much different than those experienced in the acoustic sensor while the amplitude noise will be exactly the same. The difference in the phase noise stems from the interferometric paths (medium) for both beams being the same. For the system shown in Fig. 3, thermal and acoustic fluctuations will not produce any phase noise as the phase shift they produce is reciprocal (that is, the phase produced by one propagation direction is canceled out by the same phase produced in the opposite propagation direction). The only appreciable phase noises in this type of system are: 1) distributed Rayleigh backscattering over the entire fiber, creating a superposition of signals out of phase with the transmitted beams [10], and 2) fiber birefringence, which can cause the counter-propagating polarized beams to take different paths therefore altering the value of  $\theta_s$ . If the fiber's birefringence is related to a randomly changing environment, then the random path length difference will create a random drift phase.

Albeit the rotational rate sensor does not have the drift problem that the acoustic sensor has, but it does have problems that are just as complicated. They may be itemized as follows:

- There is no way to tell the direction of rotation.
- The system is nonlinear and demonstrates a poor dynamic range.
- The measurement is a function of laser intensity.

These problems are easily identified when Eq. (4) is used to model the fiber gyro in Fig. 3. Some reasonable assumptions are taken allowing  $\theta_s = 0$ ,  $\theta_i = \phi$ ,  $E_r = E_s = E$ , and  $\theta_n = 0$  to produce signal output

$$s(t) = K\{2E^2[1 + \cos(\phi)]\}. \quad (7)$$

It is indeed evident as the cosine operation produces an even function, that this signal is independent of the sign of  $\phi$ . The sign of  $\phi$  is most important in that the specifications for most rate gyroscopes mandate magnitude and direction. The system produces a nonlinear output as the cosine function is nonlinear and also suffers from a poor dynamic range in phase measurement resulting from the  $2\pi n$  ( $n = 0, \pm 1, \pm 2, \dots$ ) degeneracy. It is also obvious that  $s(t)$  varies as the optical intensity (which is proportional to  $E^2$ ) varies.

## SYSTEM DESCRIPTION AND OPERATION

### System Introduction

It should now be evident, after a most laborious discussion, that passive fiber-optic interferometric sensors (or any interferometer) suffer from a wide variety of problems. In order to overcome these problems, it is obvious that the interferometer must be modified.

This report introduces, describes, and models a synchronous detection system used to detect phase in an optical interferometer. This system operates linearly, has the ability to function independently of large fluctuations in  $E_r$  and  $E_s$ , operates independent of  $\theta_s$ , and exhibits a large dynamic range. The system is called a heterodyne phase feedback interferometer (HPFI). The HPFI is a closed-loop system and operates on the principal of feeding back an error signal to a phase shifter in the reference leg of the interferometer to maintain synchronization or phase lock to the signal leg.

The concept of the HPFI may be applied to any interferometric system. Each interferometric system has its own set of specifications such as dynamic range requirements, noise floor, bandwidth considerations, environmental conditions, packaging requirements, and physical configuration. These specifications serve as an indicator on how the HPFI should be configured for the given system.

The HPFI is a system developed to accurately measure optical phase fluctuations in an active interferometric configuration. It overcomes many problems experienced by passive interferometers, as discussed earlier in this report. It acts as a linear detector, operates independently over a wide range of optical intensity and polarization fluctuations, exhibits a very large dynamic range, and is of a simple design configuration.



The HPFI is a second-order, synchronous detection system that employs a correction signal feedback. The term synchronous pertains to the system being locked in phase to the signal input. The HPFI's operation is similar to that of an electronic phase locked loop (PLL) commonly used for detecting frequency-modulated signals. The PLL accomplishes demodulation and phase lock by feeding back an error signal (resulting from the difference of synchronization between the system and its input signal) to a voltage/current-controlled frequency shifter. Since optical interferometric sensors produce phase modulation, the HPFI accomplishes demodulation and phase lock by feeding an error signal back to a voltage/current-controlled phase shifter.

## System Operation

Figures 4 through 7 show the block diagrams that represent the HPFI in both acoustic and rotational rate-detection configurations. The fundamental difference between Figs. 4 and 5 and Figs. 6 and 7 is the method utilized in producing the carrier signal. Figures 4 and 6 demonstrate creation of a carrier signal using phase-modulation techniques while Figs. 5 and 7 demonstrate creation of a carrier frequency by using a Bragg diffractor (which is somewhat akin to a frequency-modulation technique).

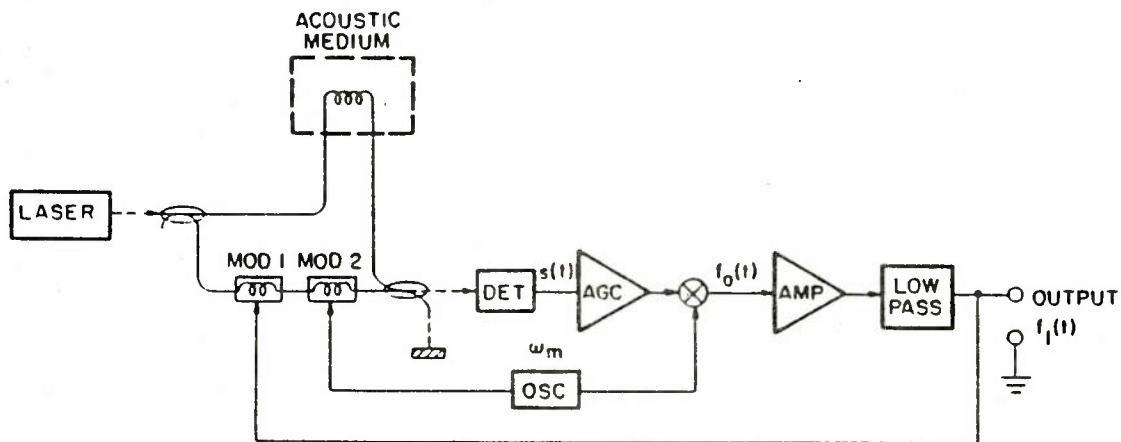


Fig. 4 - The HPFI configured for acoustic sensing employing a phase modulator to produce the carrier signal

Figures 4 and 5 demonstrate the HPFI setup for acoustic detection. In Fig. 4, light from a single-frequency laser is split up to provide inputs to both legs of the interferometer. One leg, the signal leg, is optically phase modulated by the fiber-optic coil exposed to the acoustic pressure field while the reference leg is phase modulated by Mods 1 and 2. (The methods of optical phase modulation will be discussed later in this text.) The beams are recombined, having collinear propagation, to

produce an interference pattern on the detector. Mod 2 is sinusoidally driven at  $\omega_m$  to produce a phase-modulated signal with a sufficient depth of modulation to produce phase excursions that exceed  $\pi$  rads to utilize the full contrast of the interference signal produced by the interferometer. Mod 2 essentially shifts the signal information up in frequency as sidebands to carrier frequencies of  $\omega_m$  and its harmonics. The number and amplitude of the harmonics naturally depend on the phase excursion produced by the sinusoidal drive signal. The output signal from the optical square-law detector is cross correlated (via multiplication with an electronic mixer) to a reference signal at the carrier frequency  $\omega_m$ . The low-frequency portion of the cross-correlated signal is fed back to Mod 1, the feedback phase modulator, and is denoted the error signal. When the loop gain of the feedback system is of a sufficient magnitude, it is seen that the phase produced by Mod 1 effectively duplicates the phase in the signal leg created by the acoustic perturbances. If the phase modulator in the reference leg is linear, then the output voltage  $f(t)$  is described as being a linear function of the phase produced in the signal leg (i.e., the demodulated output). It will be shown in subsequent sections that as the loop gain is increased, the phase in the reference leg becomes a closer estimate of the phase in the signal leg. It is also seen that as the loop gain increases, the system damping (or stability) decreases. This indicates the need to modify the loop (low pass) filter of the HPFI for high-gain operation.

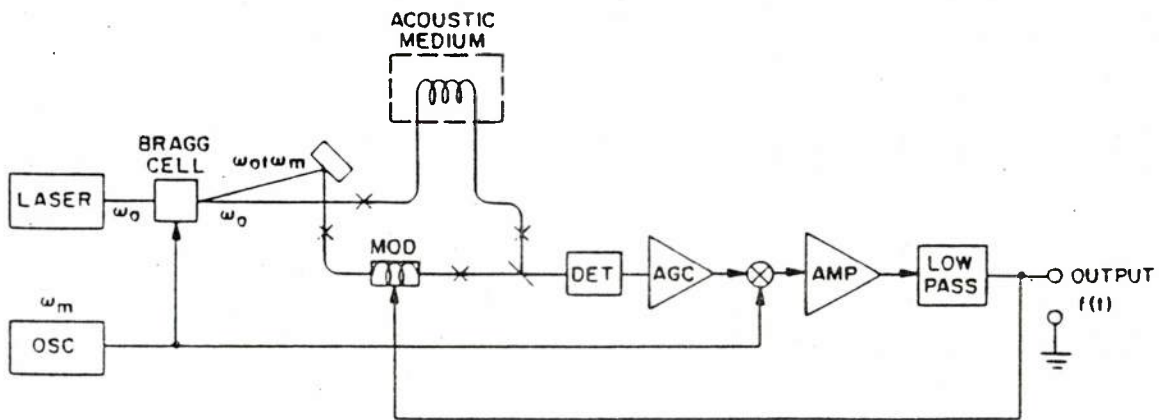


Fig. 5 - The HPFI configured for acoustic sensing employing a Bragg diffractor to produce the carrier signal

It will be shown that this modification for a suitable system is simple to implement.

Inspection of Fig. 5 reveals that the carrier frequency for signal information is produced in a different manner. In this design, an electro-optic modulator (a Bragg diffractor that is discussed in more

detail later in this text) is used to produce two optical beams at different frequencies spatially removed from each other. Despite the difference of the methods of producing the carrier signal, it is seen that the operation of both systems (in Figs. 4 and 5) in terms of system transfer function or output response are synonymous.

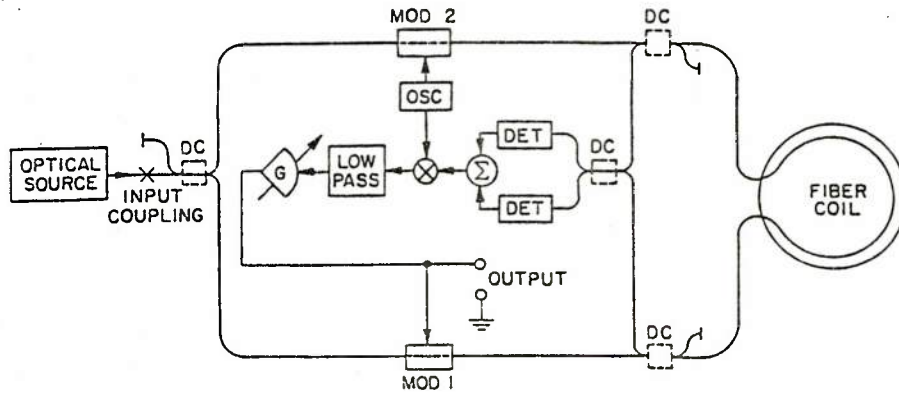


Fig. 6 - The HPFI configured for rotational rate sensing employing a phase modulator to produce the carrier signal

Figures 6 and 7 demonstrate the HPFI setup for rotational rate sensing utilizing the Sagnac effect. These systems are somewhat different than the acoustic sensors, but the measurement system (HPFI) maintains the identical function as before. In the rotational rate-sensor systems, a carrier signal is generated; the beams counter-propagate through the sensor coil to be recombined on the detector or detectors (the choice of one or two detectors is optional). The detected signal is cross correlated with an unmodulated signal at the fundamental of the carrier frequency with the resultant low-frequency component being processed and fed back to a phase modulator in the interferometer. As in the case of the acoustic sensor, the feedback signal also constitutes the output signal of the measurement system.

The particular block diagrams shown in Figs. 6 and 7 utilize evanescent field-type coupling [11,12] to constitute physical beamsplitting. This is a well-known phenomenon in dielectric waveguides where the guided mode has wave energy beyond the propagation boundaries. This energy is directionally transferred to another waveguide by placing it close enough to the primary waveguide, thereby performing the task of a bulk beamsplitter. The evanescent field-type coupling, depicted as dc (directional coupler) is schematically used in Figs. 6 and 7 to give insight to an integrated optical device. These evanescent couplers may also be used in lieu of beamsplitters for the acoustic sensors represented in Figs. 4 and 5.



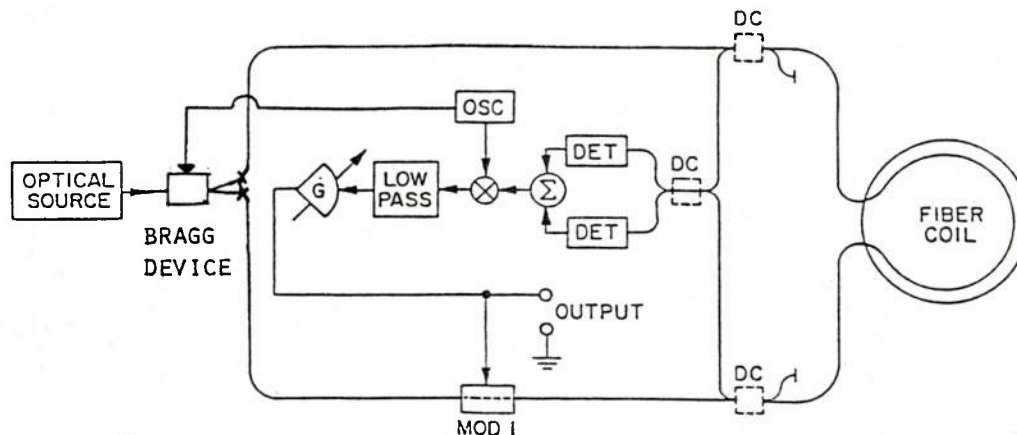


Fig. 7 - The HPFI configured for rotational rate sensing employing a Bragg diffractor to produce the carrier signal

All of the HPFI configurations discussed up to now employ processes that shift the information up in frequency. This feature is of tantamount importance when considering the effectiveness of an interferometric measurement system. This frequency shift of signal information enhances the interferometer's ability in two ways:

1. It allows system operation in a region where detector  $1/f$  noise and laser intermodulation noise are low.
2. It allows amplitude stabilization techniques (a clipper or AGC circuit) to be applied to prevent optical intensity fluctuations or acute polarization from altering the system dynamics.

For semiconductor optical detectors, the main contributions to  $1/f$  noise relate to the properties of the surface of the material and how the generation and recombination of carriers occur [13]. Laser intermodulation results from the multiline operation of most lasers. This multiline phenomenon is well known in lasers resulting from "inhomogeneously broadened" medias [14] where the frequency spacing of the laser lines within the broadened gain curve is approximately equal to  $c/2\ell$  where  $c$  is the speed of light in the laser medium and  $\ell$  is the cavity length. This frequency spacing is constantly shifting as the spacing is a function of both random environmental conditions and the mismatch between the cavity resonance and the inverted medium's natural resonance. This constant shifting of the frequency spacing along with optical square-law detection techniques produces an intermodulation noise that dominates the lower frequencies [15]. Both  $1/f$  noise and intermodulation noise manifest themselves as amplitude fluctuations. The HPFI can be easily configured to operate at frequencies well away from these noise sources.

Since the HPFI operates with a carrier frequency, it is a simple matter to stabilize the carrier level independent of optical intensity fluctuations or acute polarization rotations. The importance of the carrier amplitude stabilization will be elucidated in a subsequent chapter in this report, where it will be demonstrated that the loop gain  $G$  of the system is a function of the input carrier level. The most desirable HPFI configurations rely on  $G$  being a constant.

Carrier-amplitude-stabilization techniques employ either an automatic-gain-control (AGC) device or a hard limiter. Slow random phase fluctuations manifest themselves such that a hard limiter (which is much simpler than an AGC) cannot be used for HPFI's configured with the carrier signal being generated by a phase modulator. This stems chiefly from the insight that the phase-modulated carrier-generation technique generates harmonics (in fact, for maximum signal contrast, the second harmonic is almost the same size as the fundamental). These harmonics are also subject to the hard limiter. This type of process obfuscates the information to a point that proper operation of the system is impossible. Automatic gain control must be used for the case of phase-modulated carrier generation. The only HPFI configuration where hard limiting is viable is where only one carrier exists, which obviously restricts operation to systems employing the Bragg diffractor.

## Optical Modulation

### Bragg Diffraction

Figure 8 schematically represents the operation of a Bragg diffractor. A single-frequency ultrasonic wave is produced by a piezoelectric transducer and coupled into an isotropic homogeneous medium. The effect that this traveling wave has on the interaction medium is that of a sinusoidally varying index distribution and may be conceptualized with the analogy of the device being a dynamic diffraction grating that doppler shifts the diffracted light. A commonly used transducer to produce the ultrasonic signal is lithium niobate ( $\text{LiNbO}_3$ ). A common diffraction interaction medium is lead molybdate ( $\text{PbMoO}_4$ ).

When input light to the Bragg diffractor is at the Bragg angle  $\phi_B$ , where

$$\phi_B = \frac{1}{2}\lambda/\Lambda \quad (8)$$

(where  $\lambda$  is the free-space wavelength of the light and  $\Lambda$  is the acoustic wavelength in the interaction medium, for certain given conditions such as sufficient ultrasonic power and long enough interaction length), all of the diffracted light will constructively interfere in one direction giving rise to a single diffracted beam at a shifted optical frequency [16].

If this diffraction phenomenon is modeled on the particle level, the theory of conservation of momentum predicts that the acoustically produced photon and the input photon are annihilated with the simultaneous creation of a new photon at a new propagation direction. Figure 9 shows the momentum diagram for propagation. Conservation of energy describes the upshift of frequency for the scattered light, which is simply equal to the acoustic frequency. The angle  $\phi$ , the scattered light shifted from the unscattered light, is described by Yariv [17] as

$$\phi = \lambda/\Lambda = 2\phi_\beta. \quad (9)$$

Fig. 8 - Bragg diffractor (right)

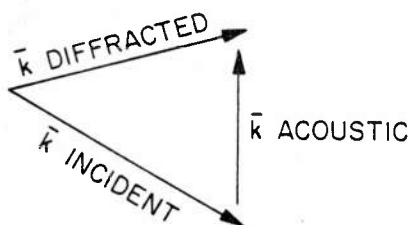
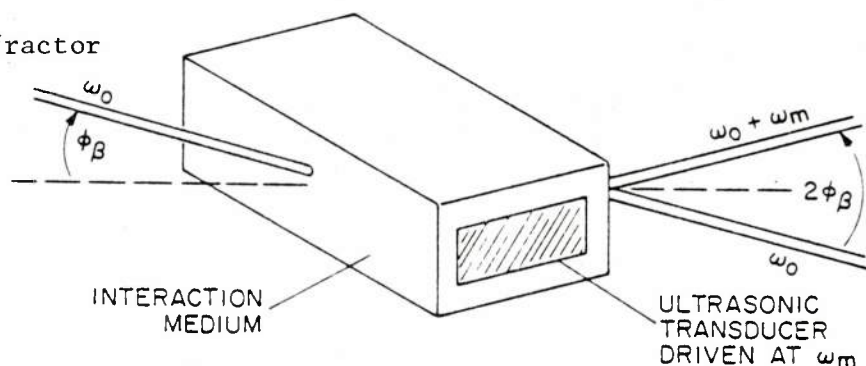


Fig. 9 - Momentum diagram for Bragg diffractor (left)

### Optical Phase Modulation

The optical phase modulators shown in Figs. 4 through 7 will be defined as any transducer that produces a change in optical phase that varies linearly with its input signal. From previous discussion, it was elucidated that different interferometric measurement systems see a large range of phase magnitudes with which to synchronize. The acoustic sensor may have to track thousands of rads while the rotation-rate sensor might require only a trackability of around 10 rads.

For the fiber-optic acoustic sensor, a very effective modulation technique is accomplished by wrapping the fiber tightly around a thin-walled piezoelectric cylinder. This type of modulator induces an optical phase shift by stretching the fiber resulting from an electromechanical radial displacement of the cylinder [18]. If these piezoelectric devices are operating at frequencies well below their resonant frequency, they may be modeled as linear devices exhibiting a linear relationship between the applied voltage and the induced optical phase shift [19]. In the optics laboratory at the Naval Research Laboratory's Underwater Sound Reference Detachment in Orlando, Florida, a 5-cm-diam, PZT-4 (lead zirconate-lead titanate) cylinder, with a wall 0.3-cm-thick and 5-cm-long

with approximately 10 m of fiber wrapped around it, is capable of producing a phase shift (using the 6328-Å line from a helium-neon laser) of approximately 10 rads/V. This cylinder is capable of sustaining voltages of up to  $\pm 500$  V and operates linearly up to approximately 2000 Hz. This predicts a trackability of this phase modulator of  $\pm 5000$  rads.

The rotational rate sensor does not require such a large tracking range, and a suitable phase modulator may be realized by utilizing the Pockels effect [20] seen in certain crystals. The Pockels effect is a linear electro-optical effect that is observed in certain crystals and that produces a birefringence linearly proportional to the applied transverse electric field. To produce just phase modulation and not polarization rotation, the input beam (which is assumed to be linearly polarized) is lined up to have its polarization parallel to one of the crystal's birefringence axes. The crystal most commonly used for this type of optical phase modulation is  $\text{LiNbO}_3$ . This is due in part to its inherent, large electro-optic coefficient and also to the ability to use the crystal in an integrated optic configuration. These lithium niobate modulators have the ability to operate linearly up to tens of megahertz with a range up to about  $\pm 5$  rads using conventional components that generate voltage swings of  $\pm 20$  V. These numbers are based on general handbook values and currently achievable crystal geometries [21,22].

## LINEAR ANALYSIS

Earlier in this report, the HPFI was described as a second-order nonlinear system. The nonlinearity results from the correlation technique (the mixer) used in comparing the interferometer's phase to the reference phase (from the oscillator) that produces the sine of the difference of both of the phases. As can be expected, this nonlinear term manifests itself as a malignant menace in the system modeling such that simple solutions are completely out of the question. Careful inspection of the system equation shows that when one is interested in the steady-state response, the nonlinearity may be replaced with a first-order, linear approximation providing certain provisions on system parameters are met. This linearization creates an amenable environment for the linear-minded engineering community, and standard control-theory techniques may be utilized in analyzing the system. This chapter develops the model for the HPFI and uses the linear approximation to analyze and discuss the system performance and operation.

### The Model

#### General Development

A statement was made in the previous chapter to the effect that the modeling for the HPFI is consistent regardless of the interferometer or method of producing the carrier signal (this will become evident as the discussion continues). With this in mind, the system in Fig. 4 (the



acoustic sensor with a phase-modulated carrier signal) will arbitrarily be chosen to be modeled.

The interference pattern produced by the interferometer in Fig. 4 may be generalized by Eq. (4) with the introduction of two more phase terms ( $\phi_m$  and  $\theta_m$ ) produced by the respective phase modulators Mod 1 and Mod 2. The output of the optical square-law detector will yield

$$s(t) = [KE_r^2 + E_s^2 + 2E_r E_s \{\cos[\theta_s + \theta_i(t) + \theta_n(t) - \phi_m(t) - \theta_m(t)]\}]. \quad (10)$$

From a previous discussion,  $\phi_m$  is the feedback phase to keep the interferometer synchronized to the input while  $\theta_m$  is phase produced to generate the carrier and may be represented by the expression

$$\theta_m = \beta \sin \omega_m t, \quad (11)$$

where  $\omega_m$  is the rad frequency of the oscillator. For the case of the acoustic sensor,  $\theta_n$  will take on the value of  $\theta_{nT}$  (the temperature-induced phase shift). If the phase terms are lumped together such that

$$\theta_i + \theta_{nT} + \theta_s - \phi_m = \phi_i - \phi_m = \phi_e; \quad (12)$$

and only being interested in the ac component of the interference pattern,

$$s(t)_{ac} = 2E_r E_s K[\cos(\beta \sin \omega_m t - \phi_e)]. \quad (13)$$

This expression may be rewritten with the aid of some trigonometric identities to reveal

$$s(t)_{ac} = 4KE_r E_s \left[ \sum_{n=1}^{\infty} J_{2n}(\beta) \cos(2n\omega_m t) \cos\phi_e + \sum_{n=0}^{\infty} J_{2n+1}(\beta) \sin \left\{ (2n+1)\omega_m t \right\} \sin\phi_e \right] \quad (14)$$

or by rearranging the terms

$$s(t)_{ac} = 4KE_r E_s \left\{ [J_1(\beta) \sin \phi_e] \sin \omega_m t + [J_2(\beta) \cos \phi_e] \cos 2\omega_m t + [J_3(\beta) \sin \phi_e] \sin 3\omega_m t + [J_4(\beta) \cos \phi_e] \cos 4\omega_m t + \dots \right\}, \quad (15)$$

where  $J_K(X)$  represents a Bessel function of the first kind of order  $K$  and argument  $X$ .

If it is known that  $\omega_m \gg \omega_c$ , where  $\omega_c$  is the cutoff frequency (-3 dB point) for the low-pass filter, it is most obvious that the only significant term in  $s(t)_{ac}$  [Eq. (15)] is the first one  $[J_1(\beta) \sin \phi_e \sin \omega_m t]$ . The rest of the terms will be greatly attenuated. It can therefore be stated that for the case of  $\omega_m \gg \omega_c$ ,

$$s(t)_{eff} = 4KE_r E_s J_1(\beta) \sin(\phi_e) \sin(\omega_m t). \quad (16)$$

The mixer is modeled as a multiplier whose inputs are  $s(t)$  and  $\sin \omega_m t$ . It is a well known fact that multiplication of sinusoids produces sinusoids at the sum and difference frequencies of the input frequencies (or product terms). If the same logic as before ( $\omega_m \gg \omega_c$ ) is employed, it is seen that the only term that is passed by the low-pass filter is the difference frequency. The effective input signal to the low-pass filter is

$$f_o(t)_{eff} = 2E_r E_s K J_1(\beta) K_1 \sin(\phi_e) = G_1 \sin(\phi_e), \quad (17)$$

where  $K_1$  is the gain of the AGC and amplifier and  $G_1 = 2E_r E_s K J_1(\beta) K_1$ . This term can also be expressed in the frequency domain via the Laplace transform

$$F_o(s)_{eff} = G_1 \mathcal{L}\{\sin \phi_e(t)\}, \quad (18)$$

which makes it rather easy to obtain the expression for the system output

$$F(s) = L(s) G_1 \mathcal{L}\{\sin \phi_e(t)\}, \quad (19)$$

where  $L(s)$  is the transfer function that models the low-pass filter. The expression for the feedback phase  $\phi_m(t)$  may be simply modeled by the equation

$$\phi_m(t) = Cf(t) \quad (20)$$

or

$$\phi_m(s) = CF(s),$$

where C may be described as the modulator constant expressed in rads/V. Note that the modulator is assumed to be constant over all frequencies. This is generally not true, but will be assumed to hold for the frequencies of interest. Combining Eqs. (19) and (20) completes the feedback loop and produces the system equation

$$\phi_m(s) = CG_1 L(s) \mathcal{L}\{\sin\phi_e(t)\} . \quad (21)$$

The low-pass filter used in this analysis is shown in Fig. 10, where its transfer function is described as

$$\frac{Y(s)}{X(s)} = L(s) = \frac{\lambda^2}{s^2 + 2s\lambda + \lambda^2} \quad (22)$$

where  $\lambda$  is defined to be  $1/RC$  or the inverse time constant of one of the filters. It is assumed that the second filter poses no loading problems on the first. This is guaranteed by placing a high-input impedance unity gain buffer amplifier between the two filter sections. The combination of Eqs. (12), (21), and (22) results in the expression

$$(s^2 + 2s\lambda + \lambda^2)\phi_m(s) = G\lambda^2 \mathcal{L}\{\sin[\phi_i(t) - \phi_m(t)]\} , \quad (23)$$

where  $G = CG_1$ . If both sides of this equation are inverse Laplace transformed, one obtains

$$\begin{aligned} \mathcal{L}^{-1} \left\{ s^2 \phi_m(s) \right\} + 2\lambda \mathcal{L}^{-1} \left\{ s \phi_m(s) \right\} + \lambda^2 \mathcal{L}^{-1} \left\{ \phi_m(s) \right\} \\ = G\lambda^2 \sin[\phi_i(t) - \phi_m(t)] ; \end{aligned}$$

or



$$\begin{aligned}
& \ddot{\phi}_m(t) + \mathcal{L}^{-1} \left\{ s\phi_m(0) \right\} + \mathcal{L}^{-1} \left\{ \dot{\phi}_m(0) \right\} \\
& + 2\lambda \left[ \dot{\phi}_m(t) + \mathcal{L}^{-1} \left\{ \phi_m(0) \right\} \right] + \lambda^2 \phi_m(t) \\
& = G\lambda^2 \sin[\phi_i(t) - \phi_m(t)].
\end{aligned} \tag{24}$$

If it is assumed that the feedback phase  $\phi_m(t)$  and its time derivative are zero, the resulting terms of Eq. (24) are

$$\ddot{\phi}_m + 2\lambda \dot{\phi}_m + \lambda^2 \phi_m = G\lambda^2 \sin(\phi_i - \phi_m), \tag{25}$$

where the time variation for variables  $\phi_i$  and  $\phi_m$  is assumed.

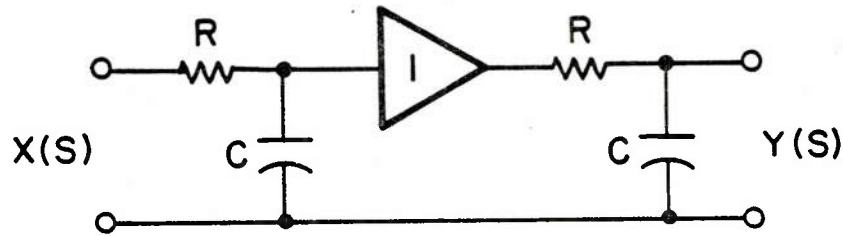


Fig. 10 - Second-order, low-pass filter

Equation (25) will also result when modeling the system in Fig. 5 (which uses a Bragg diffractor to produce the carrier signal). To demonstrate how the Bragg diffractor works, the interferometer equations will be rederived.

Making the same assumptions as before as to the monochromatic planar nature of both optical fields permits  $E_{r1}$  and  $E_{s1}$  in Fig. 5 to be expressed as

$$\overline{E_{s1}}(t) = E_{s1} \exp\{i[(\omega_o + \omega_m)t + \theta_{s11} + \theta_{i1}(t) + \theta_{n1}(t)]\}$$

and

$$\overline{E_{r1}}(t) = E_{r1} \exp[i(\omega_o t + \theta_{s12} + \theta_{n2})]. \quad (26)$$

If the same optical detector is used and is ac coupled, the output voltage  $s(t)$  of the square-law detector yields

$$s_1(t) = 4KE_{r1}E_{s1} \cos(\omega_m t + \phi_{e1}), \quad (27)$$

where  $\phi_{e1} = \phi_{i1} = \phi_{m1}$ .

If the gain of the amplifier is negative and the input to the mixer (multiplier) is  $\sin \omega_m t$ ,

$$\begin{aligned} f_{o1}(t) &= -4KE_{r1}E_{s1}K_1 \cos(\omega_m t + \phi_e) \sin \omega_m t \\ &= -2KE_{r1}E_{s1}K_1 [\sin(2\omega_m t + \phi_e) - \sin \phi_e]. \end{aligned} \quad (28)$$

For  $\omega_m \gg \omega_c$ , the equation reduces to

$$f_{o1}(t) = 2K_1E_{r1}E_{s1} \sin(\phi_e) = G_{11} \sin \phi_e, \quad (29)$$

where  $G_{11} = 2K_1E_{r1}E_{s1}$ .

It is clearly obvious that Eq. (17) is very much like Eq. (29). The only difference between the two is how the individual amplitude terms make up the respective gain terms  $G$  or  $G_{11}$ . This is irrelevant to the model in that the terms are treated as a constant and may be set by changing the gain of an amplifier in either of the feedback loops. The feedback modulators to both systems are functionally identical; hence, the models representing both systems are functionally identical. If one were to model the rate sensors in Figs. 6 and 7, the end result (as should be expected) will be an expression just like the one of Eq. (25).

## Linearization of the Model

Inspection of the system Eq. (25) shows a second-order nonlinear system. The nonlinearity arises from the dependent variable being a part of the argument of the sine function (a nonlinear operator).

If one, for the time being, assumes a slowly varying input phase ( $\phi_i$ ), such as a thermal drift phase, the only term on the left-hand side of Eq. (25) (assuming steady-state conditions) of any significant value will be the  $\lambda^2 \phi_m$  term. Remember, the main objective for this system is for  $\phi_m$  to duplicate  $\phi_i$ , so  $\phi_m$  will be slowly varying also. An approximation to this occurrence may be written as

$$\phi_m \approx G \sin(\phi_i - \phi_m) \quad \left| \begin{array}{l} 1. \lambda \phi_m \gg 2 \dot{\phi}_m \\ 2. \lambda^2 \phi_m \gg \ddot{\phi}_m \end{array} \right. \quad (30)$$

where the  $\lambda^2$  term has been cancelled out of both sides. It is fairly obvious to see that the maximum value of the right side of this equation is limited to  $G$ , the loop gain (expressed in rads). This allows a maximum value for  $\phi_m$  to be established.

$$\left| \phi_m \right|_{(\max)} = G \quad (31)$$

This is a most interesting consequence (although not so surprising) in that this equation is very similar to the lock range equation [23] for a PLL, which is

$$\Delta\omega_L = K_V \quad (32)$$

where  $\Delta\omega_L$  represents the frequency tracking ability of the PLL and  $K_V$  represents its loop gain expressed in rads/s.

Equation (30) provides some very interesting insight to the nonlinearity of the HPFI. It provides especially interesting results for sufficiently large  $G$ . For example, if  $G$  is arbitrarily chosen to be 100, Eq. (31) produces  $\left| \phi_m \right|_{(\max)} = 100$ . From Eq. (30) for  $\phi_m = 100$ , it isn't difficult to determine that  $\phi_i - \phi_m = \pi/2$ ; hence,  $\phi_i = 101.57$ . This suggests a fairly linear relationship between  $\phi_i$  and  $\phi_m$  (recall that the sine function is linear for small angles and does not bring in the higher ordered terms of its power series until the angle gets larger). To test this idea, the nonlinear part of Eq. (30) is replaced with a linear substitute, or specifically,

$$G(\phi_i - \phi_m) \leftarrow G\sin(\phi_i - \phi_m). \quad (33)$$

For the case of  $G = 100$ , this substitution, when placed into Eq. (30), yields  $\phi_i = 101.0$ . The worst-case error (as the nonlinearity of the sine function becomes worst case) between the linear approximation and the nonlinear equation is 0.57%. It can be easily demonstrated that as  $G$  increases, this worst-case error will decrease.

This past example makes a pretty powerful statement about the steady-state operation of the HPFI operating with a  $G$  of about 100 or more and adhering to the conditionalities of Eq. (30). It says that the nonlinearity (for large enough  $G$ ) may be for the most part ignored when studying the steady-state behavior of the HPFI when it experiences a slowly varying input phase.

Up to this point, the linearization of the system equation for the HPFI has been considered only for the case of slowly varying input phase  $\phi_i$ . This analysis obviously does not cover the general case for all frequencies as it would violate the constraints of Eq. (30). It would be most desirable to generate the criteria for linearization of the system equations for all frequencies. This turns out to be possible and will be seen to work quite well. Before plunging into this analysis, it would be beneficial to describe some parameters esoteric to the fiber-optic sensors being discussed.

- Analysis shows that the input rad frequency never needs to be more than  $4\lambda$ .
- These higher frequency signals will be of a much smaller magnitude (in phase excursion) than the earlier described low-frequency phase. These signals for both the acoustic and rotational rate sensors rarely need to exceed levels larger than a rad.

A worst-case analysis will be performed for a system operating at a frequency of  $4\lambda$ . Suppose an input signal is generated to produce some output signal

$$\phi_m(t) = A\sin\omega t,$$

then

$$\dot{\phi}_m(t) = A\omega\cos\omega t,$$

and

$$\ddot{\phi}_m(t) = -A\omega^2\sin\omega t. \quad (34)$$

If these values are plugged into Eq. (25) and allowing  $\omega = 4\lambda$ , one sees

$$-A\omega^2 \sin \omega t + \frac{A}{2} \omega^2 \cos \omega t + \frac{A\omega^2}{16} \sin \omega t = G \frac{\omega^2}{16} \sin(\phi_i - A \sin \omega t)$$

or

$$-15A \sin \omega t + 8A \cos \omega t = G[\sin(\phi_i - A \sin \omega t)],$$

simplifying to get

$$17A \left( \frac{-15}{17} \sin \omega t + \frac{8}{17} \cos \omega t \right) = G \sin(\phi_i - A \sin \omega t); \quad (35)$$

letting

$$\cos \alpha = \frac{15}{17}; \quad \sin \alpha = \frac{8}{17}. \quad (36)$$

Equation (35) is reduced to

$$17A(\cos \omega t \sin \alpha - \sin \omega t \cos \alpha) = G \sin(\phi_i - A \sin \omega t)$$

or

$$-17A \sin(\omega t - \alpha) = G \sin(\phi_i - A \sin \omega t). \quad (37)$$

Solving for  $\phi_i$ , one finds

$$\phi_i = \sin^{-1} \left[ \frac{-17A}{G} \sin(\omega t - \alpha) \right] + A \sin \omega t. \quad (38)$$

Notice here that if the largest value of A is assumed (1 rad) and also the largest value of  $\sin(\omega t - \alpha)$  is assumed (unity), the worst-case condition for describing the nonlinearity of the system is met, leaving

$$\phi_{i(wc)} = \sin^{-1} \left[ \frac{17}{G} \right] + \sin(\alpha - \pi/2) \quad (39)$$

from the CRC math tables [24], the power series expansion for the inverse sine function is described for an argument x as

$$\sin^{-1}(x) = x + \frac{x^3}{2 \cdot 3} + \frac{1 \cdot 3}{2 \cdot 4 \cdot 5} x^5 + \frac{1 \cdot 3 \cdot 5}{2 \cdot 4 \cdot 6 \cdot 7} x^7 + \dots \quad (40)$$

where  $x^2 < 1$  and  $-\pi/2 < \sin^{-1}(x) < \pi/2$ .

If  $G$  is assumed to be 100 or greater, as in the low-frequency analysis, one finds that all of the higher order terms of the power series may be neglected as they are less than 1% of the magnitude of the first-order term. This indeed implies an accurate approximation for a linear function, which implies a linear system. It is therefore permissible to rewrite the linear version of Eq. (25) as an accurate approximation of the HPFI:

$$\ddot{\phi}_m + 2\lambda\dot{\phi}_m + \lambda^2\phi_m = G\lambda^2(\phi_i - \phi_m). \quad (41)$$

## Application and Verification of the Linear Model

### System Analysis

Frequency-domain techniques utilized to analyze linear closed-loop systems seem to require fewer calculations than time-domain techniques.

If "0" initial conditions are assumed for  $\phi_m$  and  $\dot{\phi}_m$ , Eq. (41) may be Laplace transformed to reveal

$$(s^2 + 2s\lambda + \lambda^2)\Phi_m(s) = G\lambda^2[\Phi_i(s) - \Phi_m(s)], \quad (42)$$

which may be arranged to produce the transfer function  $H(s)$  describing the ratio of the system output  $\Phi_m(s)$  to the system input  $\Phi_i(s)$ , obtaining

$$\overline{H(s)} = \frac{\Phi_m(s)}{\Phi_i(s)} = \frac{G\lambda^2}{s^2 + 2s\lambda + \lambda^2(1 + G)}. \quad (43)$$

From the theory of Laplace transforms, one may recall that the system transfer function represents the Laplace transform of the impulse response of the system. Since the impulse has a flat spectrum,  $H(s)$  represents the normalized steady-state frequency response of the system. The amplitude response is determined by solving for the magnitude of  $H(s)$ ; the phase is determined by standard techniques from complex variable algebra. For  $s = i\omega$ ,

$$\text{Mag } \overline{H(s)} = H(s) = \frac{G\lambda^2}{\{4\omega^2\lambda^2 + [\lambda^2(1 + G) - \omega^2]^2\}^{1/2}} \quad (44)$$

and

$$\text{Phase } \overline{H(s)} = H(s) \angle \theta = \tan^{-1} \left[ \frac{2\omega\lambda}{\lambda^2(1 + G) - \omega^2} \right]. \quad (45)$$

It is quite obvious that the system's magnitude and phase vary with the loop gain  $G$ , the inverse time constant  $\lambda$ , and the rad frequency  $\omega$ .

The natural frequency  $f_n$  for the HPFI will be defined as the frequency at which  $H(s)$  is a maximum. To determine the natural frequency, one simply differentiates  $H(s)$  with respect to  $\omega$  and sets it equal to zero. The resulting equation is

$$\omega_n = \lambda\sqrt{G - 1} \quad \text{or} \quad f_n = \lambda \frac{\sqrt{G - 1}}{2\pi}. \quad (46)$$

The natural frequency will be an aid in determining the system bandwidth and estimating the system performance.

The system bandwidth may be described by the cutoff frequency  $f_c$ , which is defined to be the frequency where the output signal is attenuated by 3 dB from the input signal. To determine  $f_c$ ,  $H(s)$  is equated to 0.707 (-3 dB) to explicitly solve for  $\omega_c$  ( $=2\pi f_c$ ), which reveals

$$f_c = \lambda/2\pi \left[ G - 1 + (2G^2 - 4G)^{1/2} \right]^{1/2}. \quad (47)$$

A close inspection shows that for  $G \geq 10$ , the cutoff frequency may be accurately approximated as

$$f_c = 1.55f_n (G \geq 10). \quad (48)$$

It turns out (and is lucidly demonstrated) that the HPFI requires  $G$  to be much larger than 10 to produce accurate detection. A useful parameter to describe the stability of a system is the damping ratio  $\delta$ . It is determined by the placement of the complex poles of the system transfer function. It is defined as the sine of the angle made from the imaginary axis to the pole in the second quadrant with the origin at the vertex [25]. For the transfer function in Eq. (43),  $\delta$  may be expressed as



$$\delta = \frac{1}{\sqrt{1 + G}} . \quad (49)$$

The important feature to note here is that the damping is only a function of  $G$ .

A typical system in the laboratory operates with a  $\lambda$  of any value and  $G$  between 50 and 2000. Figures 11, 12, and 13 show plots of  $H(s)$  and  $H(s)\angle\theta$  for  $\lambda = 2100$ ,  $G = 1000$ , 500, 200, and 50. Figure 11 demonstrates increased bandwidth with increased  $G$ . Figure 12 is the same as Fig. 11 but is normalized to  $f_n$ . One may take interest in noting that when  $G$  is increased, the system amplitude at  $f_n$  is increased. This is inversely related to the damping of the system. Inspection of Eq. (44) produces

$$H(f_n) = \sqrt{G/2} . \quad (50)$$

The plot in Fig. 13 is an expanded version of Fig. 11, which exemplifies the system's output for a flat input spectrum in amplitude and phase. The dashed line for the plot of  $H(s)$  represents the system input. One may take note that the system with a  $G$  of 1000 produces the most desirable output (in that  $\phi_m$  more accurately duplicates  $\phi_i$ ) response for a 2-kHz input-signal bandwidth. The system with  $G = 1000$  also has the highest bandwidth and the smallest damping ratio. From Eq. (49) the damping ratio for  $G = 1000$  is calculated to be 0.0316. This is a rather small  $\delta$  and may create some system disadvantages such as overshoot causing system instability or loss of lock. One might be inclined to use the results in Fig. 13 as a design aid (as the author did some time ago). This practice will not yield much information as each curve on the plot contains a different natural frequency. If one looks at Fig. 12, where the curves are normalized to their respective natural frequencies, it would become lucidly evident that the curves for  $H(s)$  are almost identical when the frequency is not near the natural frequency. This would tend to indicate that the natural frequency governs the system response (at lower frequencies than  $f_n$ ) while the loop gain governs the damping. With all this information at hand, the design engineer can meet various specifications by choosing the proper  $f_n$  for system response and  $G$  for dynamic range and damping ratio, while  $\lambda$  will "pop out" of the design equations.

Figures 14 and 15 demonstrate how  $f_n$  can be used to pick the system response. In Fig. 14,  $f_n$  is seen to be the same for all curves. This is accomplished by picking various pairs of  $G$  and  $\lambda$  that satisfy Eq. (36) for a constant  $f_n$ . In this figure,  $f_n$  is approximately 10 kHz ( $f_c = 15.5$  kHz). Note that  $H(f_n)$  varies for various  $G$  but that  $H(f \ll f_n)$  is relatively independent of  $G$ . The design engineer is interested in the system response where the output duplicates the input. This is seen to occur for  $f \leq 0.1f_c$ . Figure 15 demonstrates this phenomenon; it shows the first 2 kHz of the curves in Fig. 14. In this expanded view, it is very obvious that the curves are almost identical.

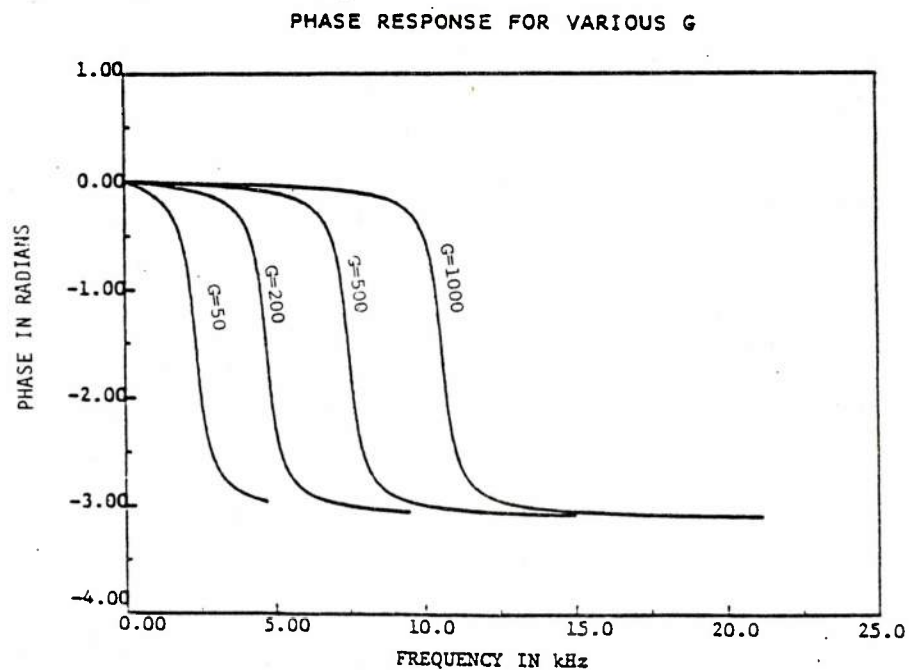
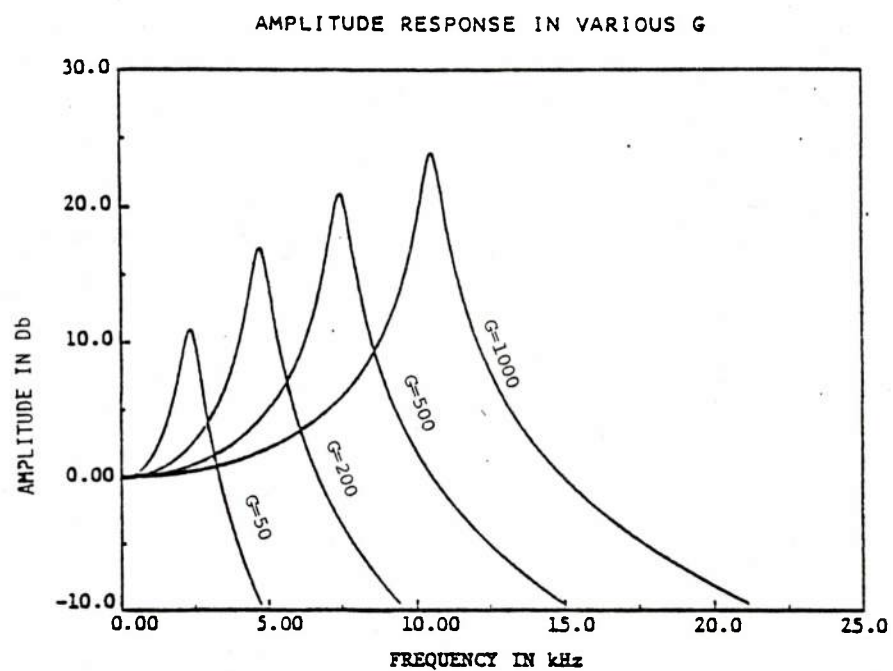


Fig. 11 - Theoretical response.  $\lambda = 2100$ , G is variable

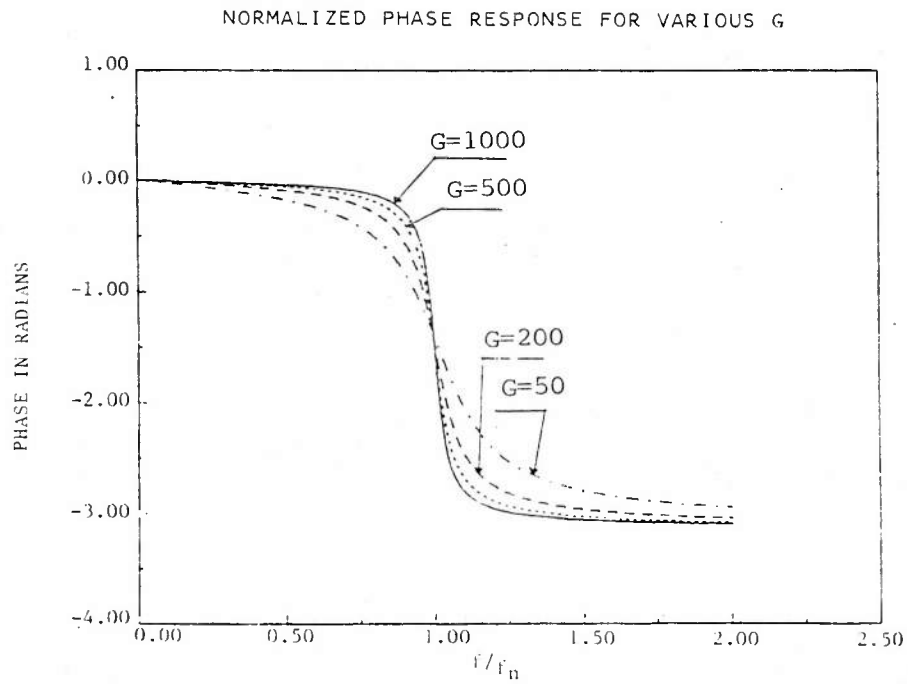
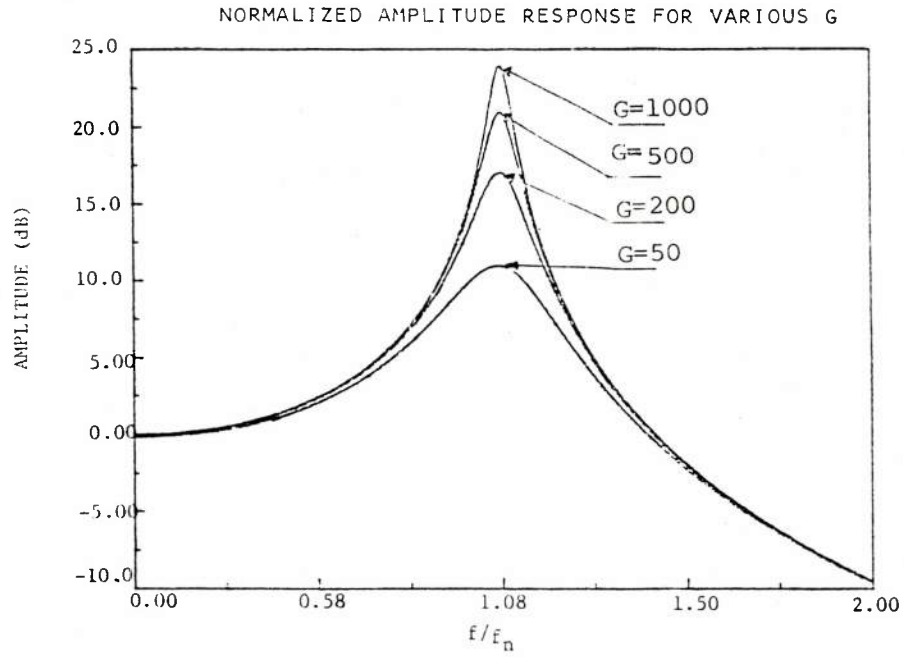


Fig. 12 - Theoretical response.  $\lambda = 2100$ ,  $G$  is variable

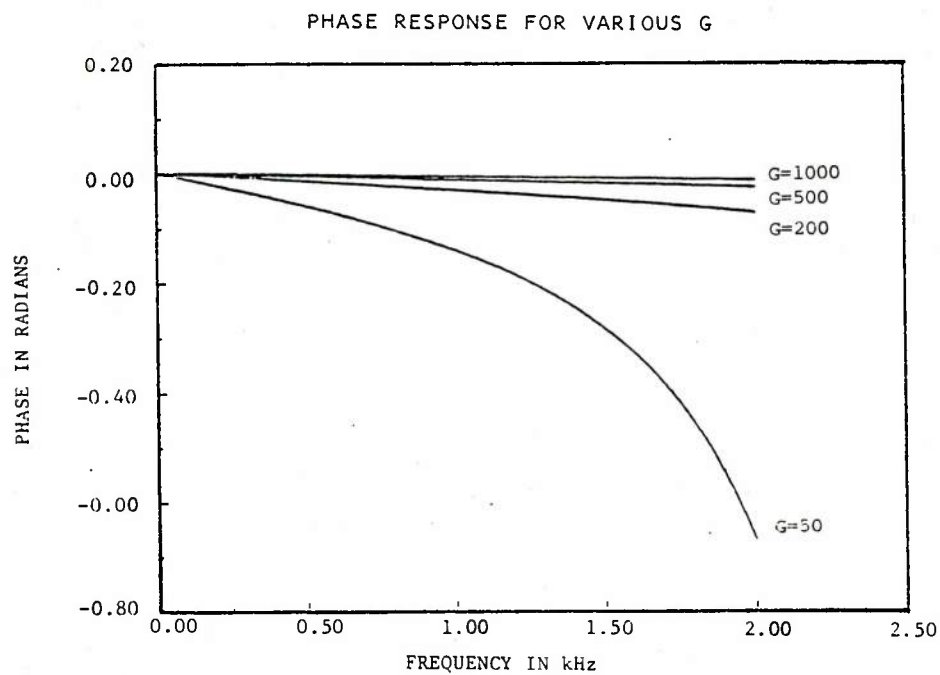
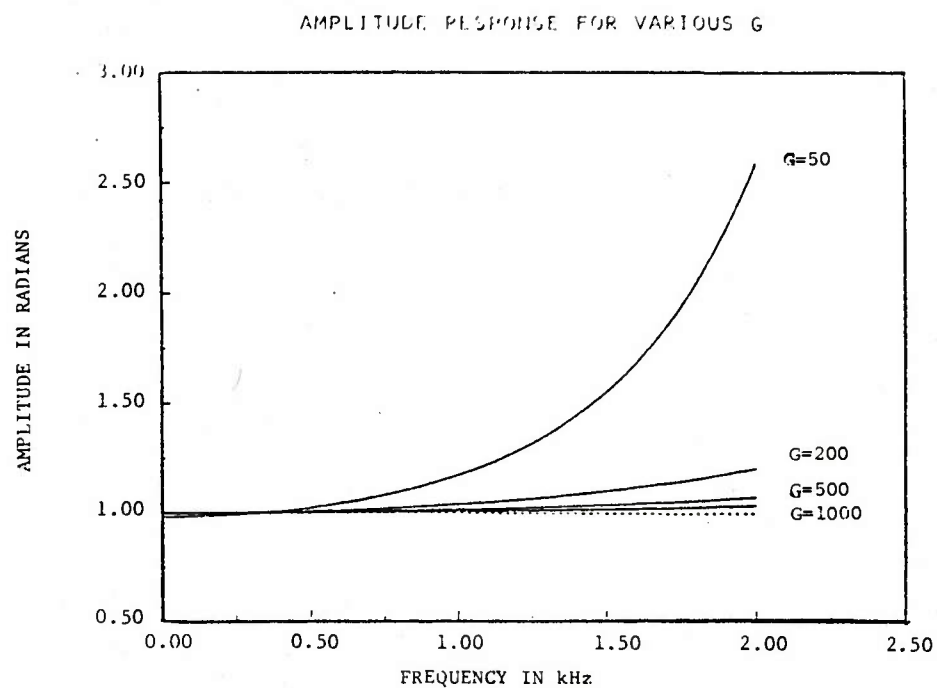


Fig. 13 - Theoretical response.  $\lambda = 2100$ , G is variable

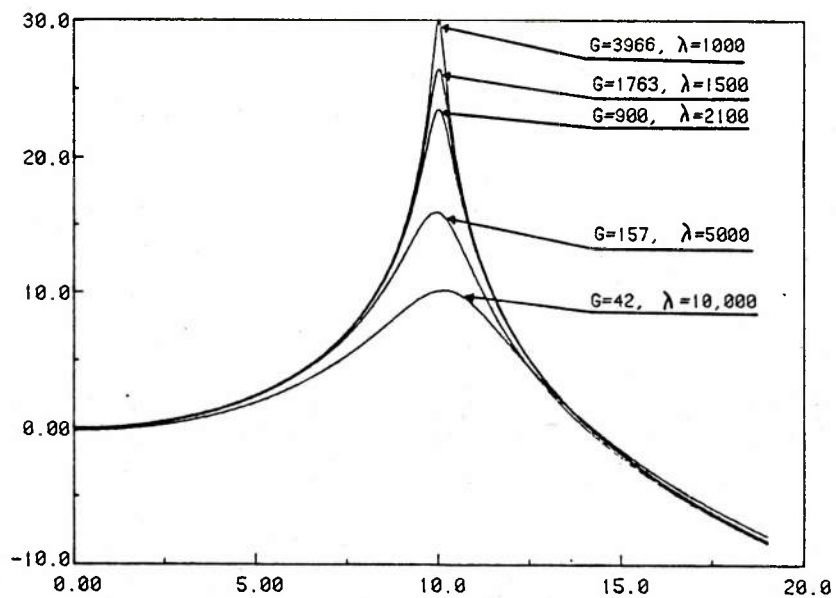


Fig. 14 - Amplitude response for  $f_n = 10$  kHz

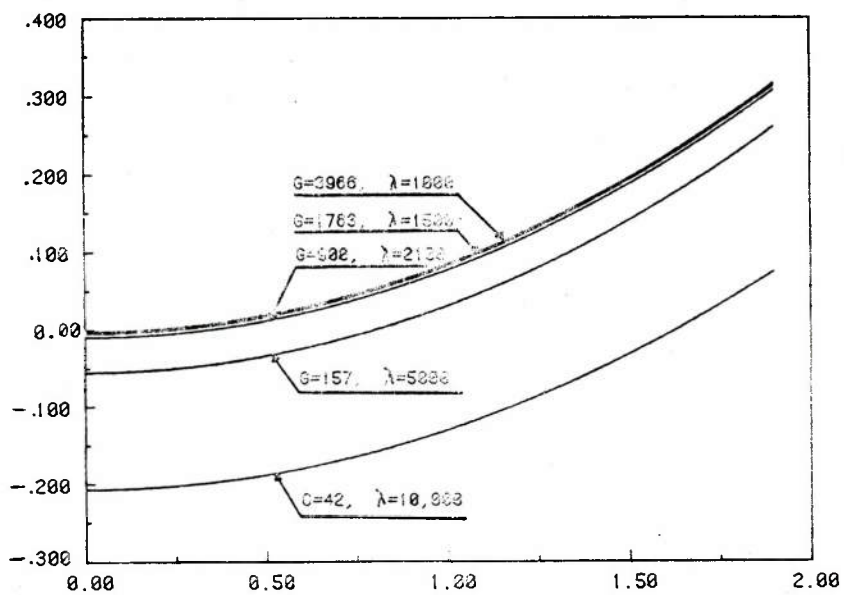


Fig. 15 - Expanded view of Fig. 14

## Verification of the Linear Model

Up to this point the development of this report has been completely theoretical. The author now wishes to present some laboratory results to provide a little corroboration to this most enlightening theory.

A system was configured to demonstrate the HPFI with a Bragg diffractor (Fig. 5) at the Naval Research Laboratory's Underwater Sound Reference Detachment. The laser used was a Tropel-100, single-frequency (which provides a coherence length well over 100 m), helium neon, 1-mW source of wavelength 0.6328 microns. The Bragg diffractor used was manufactured by Isomet and consists of a series 230 driver operating at 80 MHz and a model #232-1 lead molybdate modulator. The fiber used was ITT-T16-01 step index fiber, which has the property of propagating single-mode ( $HE_{11}$ ) optical radiation of wavelengths greater than 0.6 microns. An RCA 4840 photomultiplier tube with a pinhole input was used to detect the recombined beams. The output current from the photomultiplier is ac coupled, converted to a voltage, multiplied by the carrier signal, filtered, and fed back to Mod 1. Mod 1 consists of a length of fiber wrapped around a piezoelectric cylinder. Its modulator constant was measured to be 4.08 rads/V.

To test the theory generated for the HPFI, one must have a controlled (or known) input signal. This is most easily implemented by replacing the acoustic environment with another phase modulator. This modulator was measured to produce a phase of 7.87 rads per applied V. This acoustic simulator modulator was driven with a known voltage producing a known phase shift and swept from 100 to 2000 Hz in 100-Hz increments. This was done for two different system configurations wherein the first configuration  $f_n$  is set to 6000 Hz and the second configuration is operated at  $f_n = 4000$  Hz. The natural frequencies of the individual system configurations were determined by observing the system output  $f(t)$  on a spectrum analyzer. The hump produced in the noise floor at the natural frequency was easily discernable in both cases and probably accurate to  $\pm 3\%$ . Once  $f_n$  is known,  $G$  may be determined from Eq. (46) providing  $\lambda$  is known ( $\lambda$  was measured and is 2200 in both cases). Once  $G$  is determined, then Eq. (44) may be utilized to theoretically predict the system's amplitude response.

Figures 16 and 17 compare the theoretical and actual responses of both systems. The theoretical response is represented by the dashed line while the laboratory data are shown with the solid line. It is no surprise that the theoretical and the empirical data are highly correlated. This evidence should provide corroboration to the carefully drawn assumptions implemented to generate the linear estimation of the non-linear model.

Still, the most cynical of researchers may raise an eyebrow at the fact that the entire transfer function was not tested. This was done mainly in part relating to the lower (frequency) end of the transfer function being the important (or of most interest) area, for it contains the useful demodulation band (where  $\phi_i = \phi_m$ ). The rest of the transfer function isn't that particularly important, except for locating the

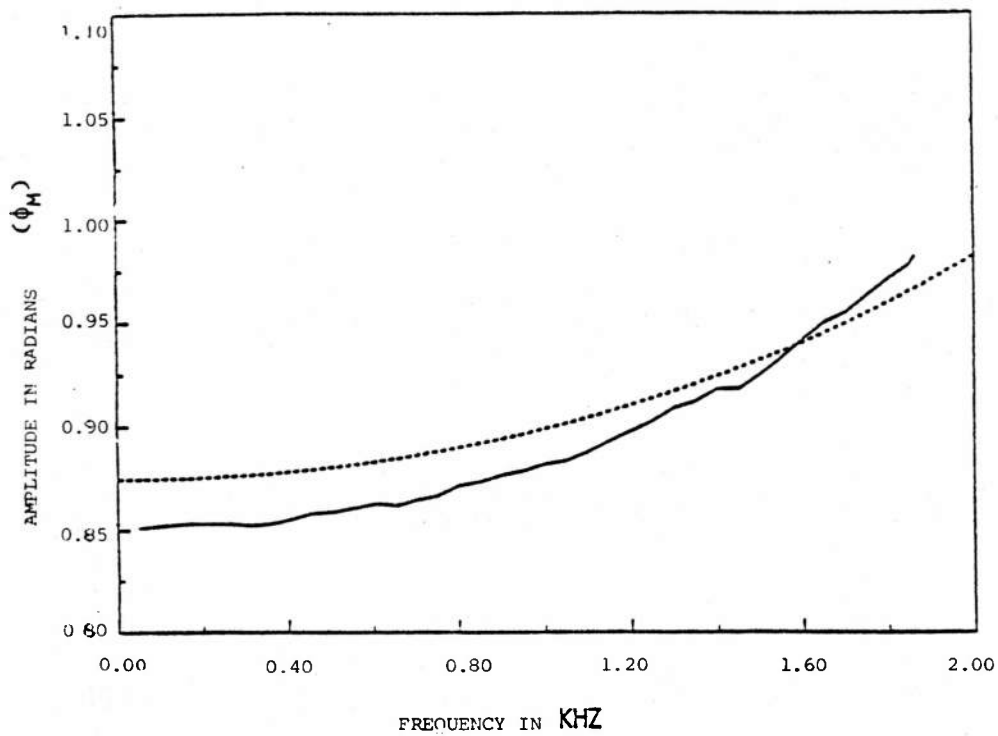


Fig. 16 - Amplitude response for  $G = 295$ ,  $\lambda = 2200$

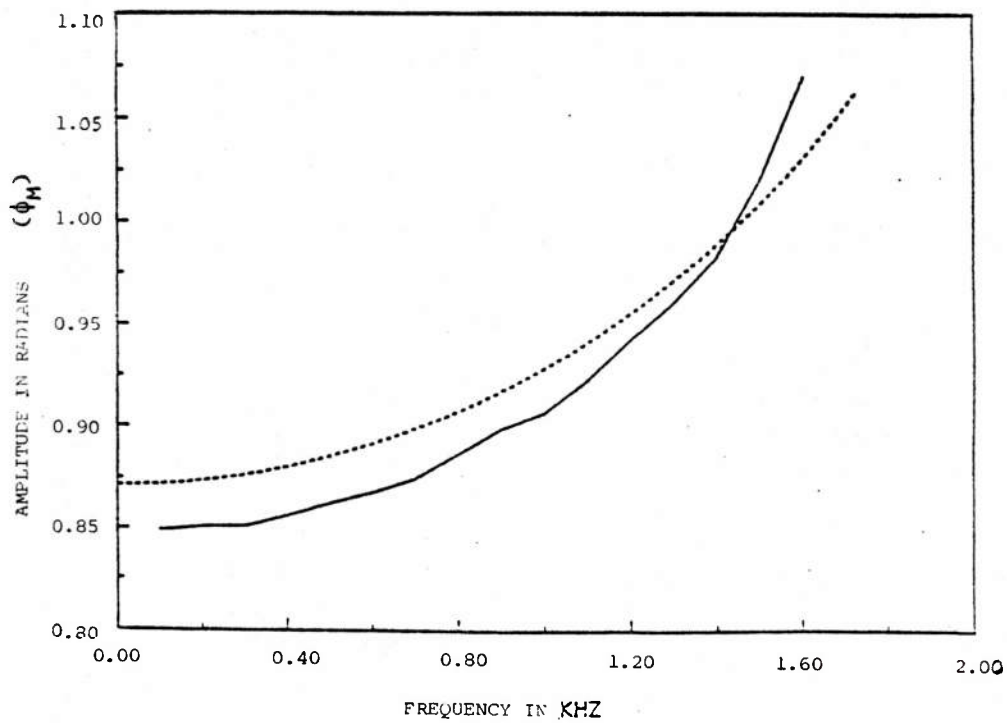


Fig. 17 - Amplitude response for  $G = 131$ ,  $\lambda = 2200$



natural frequency. To be completely thorough, a test of the entire transfer function was performed (at a much later date). In this experiment,  $\lambda = 3225$ ,  $f_n = 4800$  Hz, and  $G = 38.4$ . This experimental setup was identical to the other two, except that the feedback modulator was changed to one with a constant of 2.4 rads/V. Figure 18 compares the theoretical and actual response of the system; again both are highly correlated.

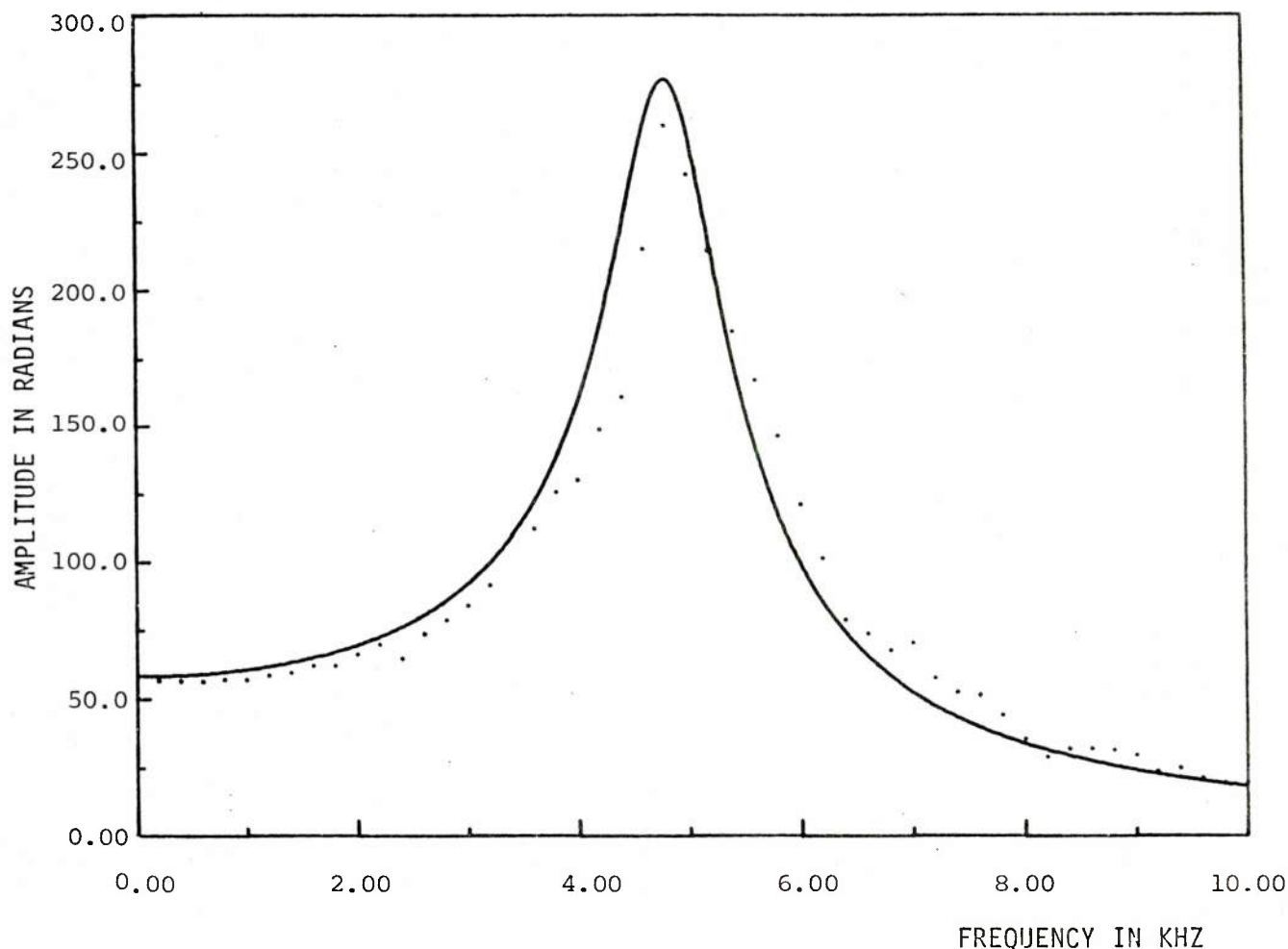


Fig. 18 - Theoretical and actual response of HPFI.  
 $\lambda = 3230$ ,  $G = 38.4$

### The Solution to the Step Response and Its Effect on System Damping

It is a well known fact that any linear second-order feedback system will "ring" at its fundamental frequency upon the receipt of a discontinuous input signal. The two most common input signals are the step and impulse. Since the step function is more physically realizable, it is chosen to be used to investigate the HPFI's behavior when responding to a discontinuity.

The step response to the HPFI may be easily obtained by starting with Eq. (43). Dividing Eq. (42) by  $s$  and taking the inverse Laplace transform of  $H(s)/s$  with the assumption of "zero" initial conditions, yields the step response  $r(t)$  to a unit step of phase starting at  $t = 0$ . Described in equation form

$$r(t) = \mathcal{L}^{-1} \left\{ \frac{H(s)}{s} \right\} = \mathcal{L}^{-1} \left\{ \frac{G\lambda^2}{s[s^2 + 2s\lambda + \lambda^2(1 + G)]} \right\}. \quad (51)$$

Simplifying the expression

$$r(t) = \mathcal{L}^{-1} \left\{ \frac{G^2}{s[s + \lambda(1 + i\sqrt{G})][s + \lambda(1 - i\sqrt{G})]} \right\}. \quad (52)$$

The technique of partial fraction expansion will be used to recognize known transform pairs:

$$\begin{aligned} & \frac{G^2}{s[s + \lambda(1 + i\sqrt{G})][s + \lambda(1 - i\sqrt{G})]} = \\ & \frac{A}{s} + \frac{B}{s + \lambda(1 + i\sqrt{G})} + \frac{C}{s + \lambda(1 - i\sqrt{G})}, \end{aligned} \quad (53)$$

where  $A = \frac{G}{1 + G}$

$$B = \frac{-(G + i\sqrt{G})}{2(1 + G)}$$

$$C = \frac{-(G - i\sqrt{G})}{2(1 + G)}.$$

The three inverse transforms are taken and combined via laws of superposition for linear systems to obtain

$$\begin{aligned} r(t) = \frac{1}{1 + G} & \left[ G - \left( \frac{G + i\sqrt{G}}{2} \right) e^{-\lambda(1 + i\sqrt{G})t} \right. \\ & \left. - \left( \frac{G - i\sqrt{G}}{2} \right) e^{-\lambda(1 - i\sqrt{G})t} \right], \end{aligned} \quad (54)$$

which may be simplified using some trigonometric relations to produce

$$r(t) = \frac{1}{1+G} \left[ G - \sqrt{G^2 + G} e^{-\lambda t} \cos(\lambda \sqrt{G} t - \theta) \right] , \quad (55)$$

where  $\theta = \tan^{-1}(G^{-1/2})$ . This equation represents the step response of the linearized model of the HPFI. Inspection of the equation shows no great surprise. At  $t = 0$ , the system output  $r(t)$  is zero (as is expected relating to the boundary conditions); and as time increases to infinity, the resulting steady-state solution reduces to

$$r(t)_{ss} = \frac{G}{1+G} . \quad (56)$$

If one goes back to Eq. (55) and defines the fundamental rad frequency of the step response to be  $\omega_f (= \lambda \sqrt{G})$ ,  $\lambda$  may be expressed in terms of the damping ratio  $\delta$  as

$$\lambda = \frac{\omega_f \delta \sqrt{G+1}}{\sqrt{G}} . \quad (57)$$

If  $G > 50$ , an accurate approximation to this equation is seen as

$$\lambda = \omega_f \delta \left| \begin{array}{l} \\ G > 50 \end{array} \right. . \quad (58)$$

Rewriting Eq. (55) one obtains

$$r(t) = \frac{1}{1+G} \left[ G - \sqrt{G^2 + G} e^{-\omega_f \delta t} \cos(\omega_f t - \theta) \right] . \quad (59)$$

It is quite obvious that the decay time of the oscillation at the system's fundamental frequency is a function of  $\omega_f$  and  $\delta$  [one might also note that for large  $G$  ( $G > 50$ )  $\omega_f = \omega_n$ ].

Figures 19 and 20 show the theoretical step responses for various combinations of  $\lambda$  and  $G$  ( $f_n = 10,000$ ) chosen for Fig. 14. They simply demonstrate a quicker decay time for a larger  $\delta$ . This indicates that if one desires a system that stabilizes quickly,  $\delta$  should be large (or  $G$  is small), which sacrifices system dynamic range [recall Eq. (31)]. This obviously indicates that a compromise be made between  $\delta$  and the dynamic range when designing for the optimum system. Figure 21 shows some photographs of the HPFI setup in the laboratory under various conditions of  $f_n$

with  $\lambda$  constant. Note that the decay time for all three configurations is the same (as theory predicts).

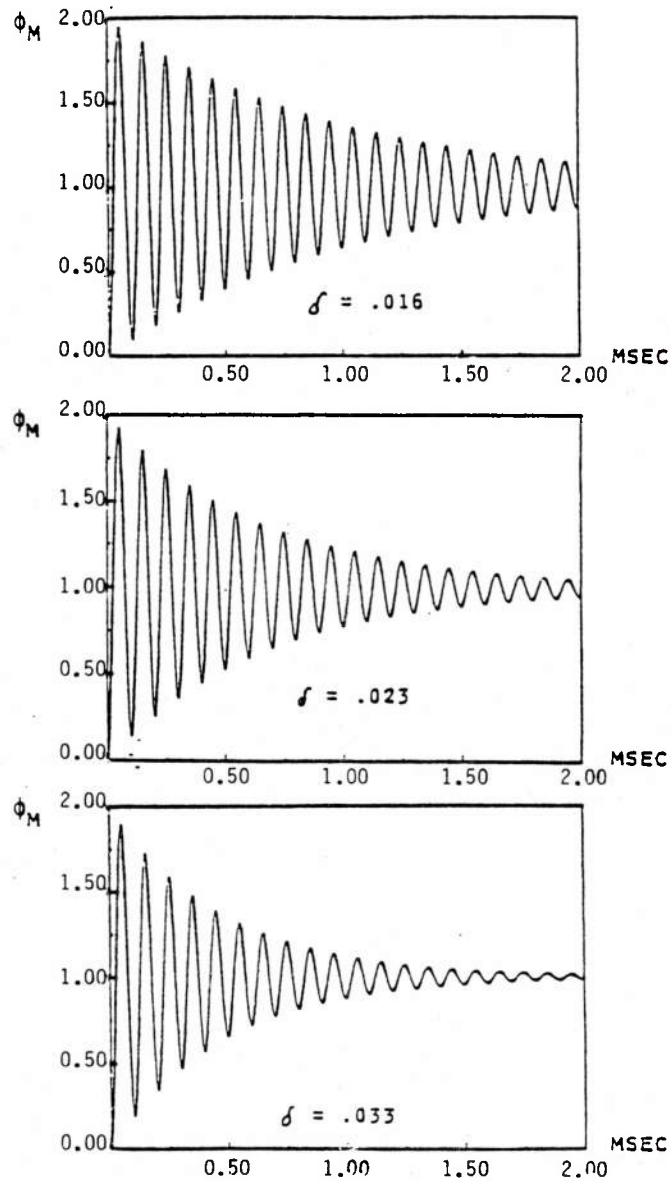


Fig. 19 - Theoretical step response for  $f_n = 10$  kHz and various  $\delta$

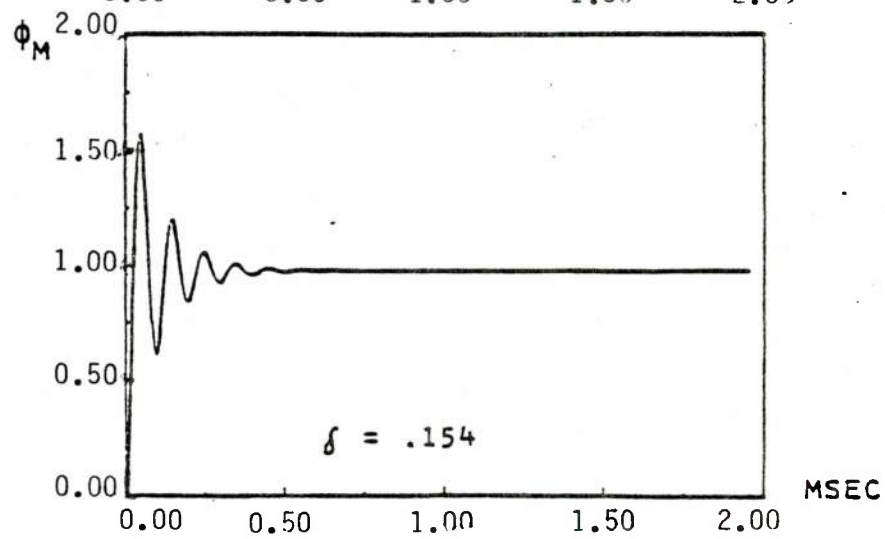
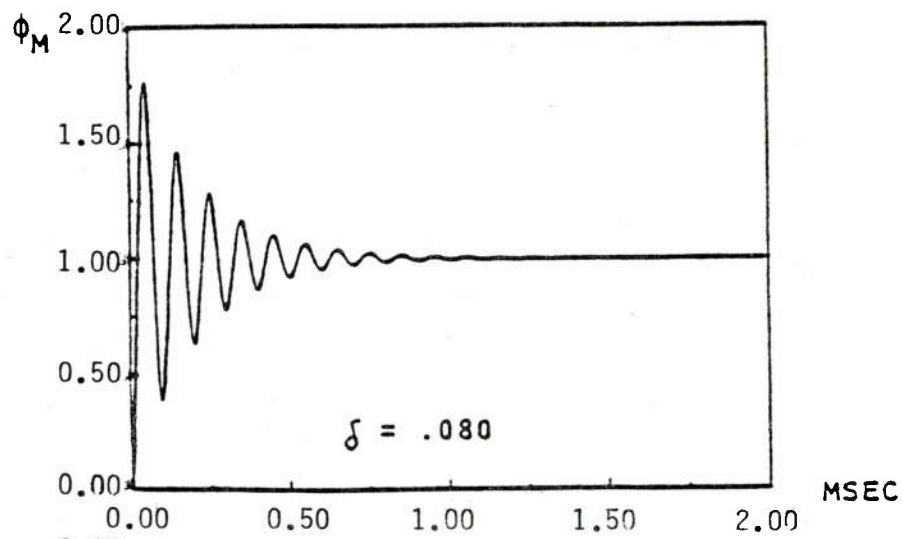
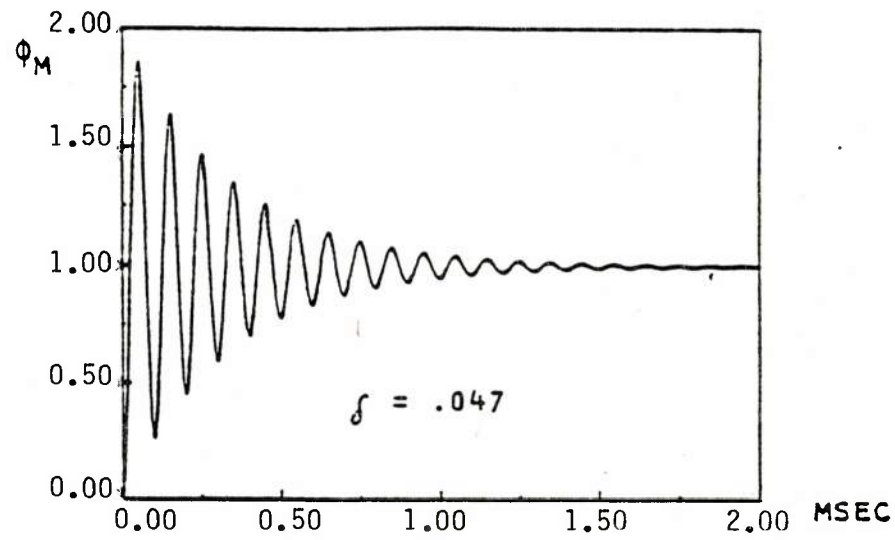


Fig. 20 - Theoretical step response for  $f_n = 10$  kHz and various  $\delta$

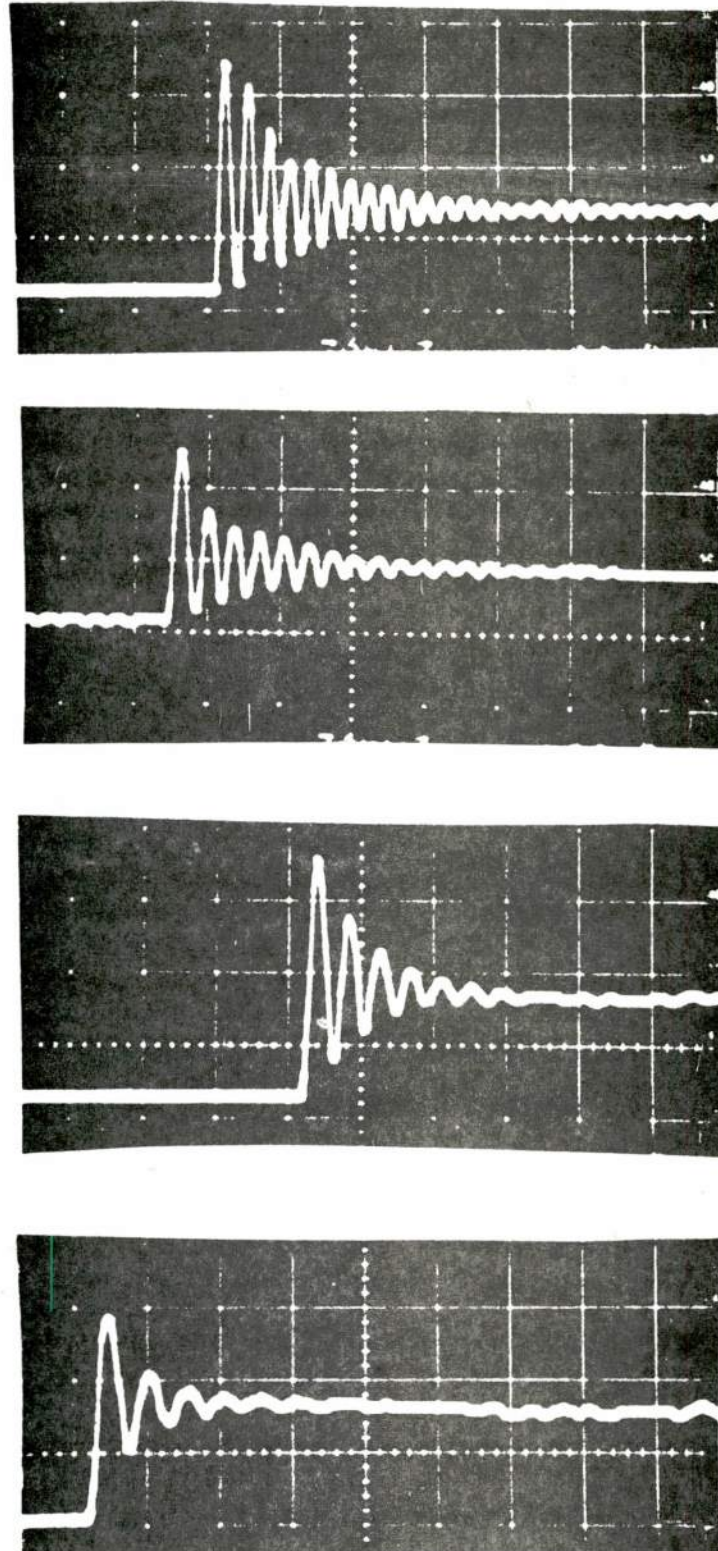


Fig. 21 - System step response for  $\lambda = 2200$  and various  $f_n$



## A Compensation Technique for Increasing System Damping when Large Loop Gains are Involved

A most obvious feature of the HPFI as modeled up to now is that when the system requires any substantial loop gain, the damping becomes quite low. This response is primarily due to the choice of low-pass filter in the feedback loop, which is the simplest 2-pole, low-pass combination possible. This simple filter is used as a vehicle to analyze the operation and performance characteristics of the HPFI by using relatively simple and uncluttered mathematics. A more sophisticated low-pass filter design in the feedback loop of the HPFI will allow much more flexibility in controlling the loop gain and damping ratio. One such filter commonly utilized by designers of phase-locked loops is the lag-lead filter [26]. This filter when implemented in the HPFI provides some shunt resistance in one of the single-pole filters and is shown in Fig. 22.

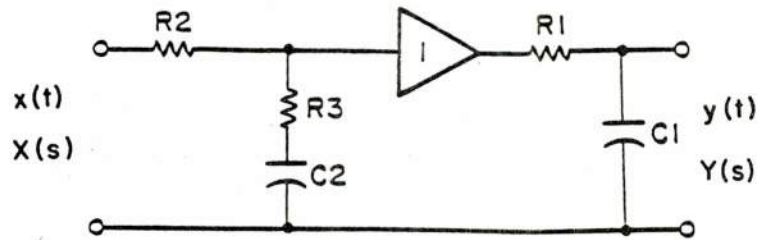


Fig. 22 - Lag-lead filter

The transfer function for this filter is

$$\frac{Y(s)}{X(s)} = \frac{K\lambda_1(s + \lambda_3)}{(s + \lambda_1)(s + \lambda_2)}, \quad (60)$$

where  $\lambda_1 = 1/R_1C_1$

$$\lambda_2 = 1/(R_2 + R_3)C_2$$

$$\lambda_3 = 1/R_3C_2$$

$$K = \lambda_2/\lambda_3.$$

If Eq. (22) is replaced with Eq. (60), the closed-loop transfer function for the HPFI may be solved (assuming all of the linearizing assumptions hold true) to be

$$H(s)_c = \frac{G\lambda_1 K(s + \lambda_3)}{s^2 + s(\lambda_1 + \lambda_2 + \lambda_1 GK) + \lambda_1(\lambda_2 + GK\lambda_3)} \quad (61)$$

This equation is seen to duplicate Eq. (43) (as it should) in the limit as  $R_3$  is taken to zero.

As before, it is most desirable to break up the transfer function into its magnitude and phase terms. With a substantial amount of algebra, one will find

$$\text{Mag } \overline{H(s)}_c = H(s)_c = \frac{G\lambda_1 K \sqrt{\ell^2 + m^2}}{c^2 + d^2} \quad (62)$$

where  $c = 2\omega^2\lambda_1(2 + GK)$

$$d = 2\omega(\omega^2 - \lambda_1^2 - GK\lambda_3)$$

$$\ell = 2c\lambda_3 - 2d\omega,$$

$$m = 2d\lambda_3 - 2c\omega,$$

$$\lambda_1 = \lambda_2,$$

and

$$H(s)_c \angle \theta = \tan^{-1}(\ell/m). \quad (63)$$

It is most difficult to look at Eq. (62) and interpret the HPFI's behavior for various values of compensation as this expression is somewhat complicated. Figures 23 and 24 show computer-generated plots for the theoretical amplitude response Eq. (62) of the HPFI for various compensations at two respective loop gains of 500 and 1500. One may take note that when  $K$  approaches 0 (or is very small), Eq. (62) will predict responses very similar to that of Eq. (44) (if  $K$  takes on the value of 0, the two equations are equal). It should become clearly obvious in Figs. 23 and 24 that when  $K$  is increased, the magnitude of the natural frequency becomes lower. This indicates that there is an increase in system damping (indicating better stability). Just how much the damping is increased by

adding the compensation may be realized by observing the closed-loop poles of the transfer function in Eq. (61). Some algebraic manipulations reveal that the damping ratio for the lag lead system is

$$\delta_c = \frac{\lambda_1(1 + GK) + \lambda_2}{2\sqrt{\lambda_1(\lambda_2 + GK\lambda_3)}}; \quad (64)$$

or, when  $\lambda_1 = \lambda_2$ , a simpler equation results:

$$\delta_c = \frac{2 + GK}{2\sqrt{1 + G}} \quad \left| \quad \lambda_1 \approx \lambda_2 \right. \quad (65)$$

These values are shown in Figs. 23 and 24 with their respective amplitude

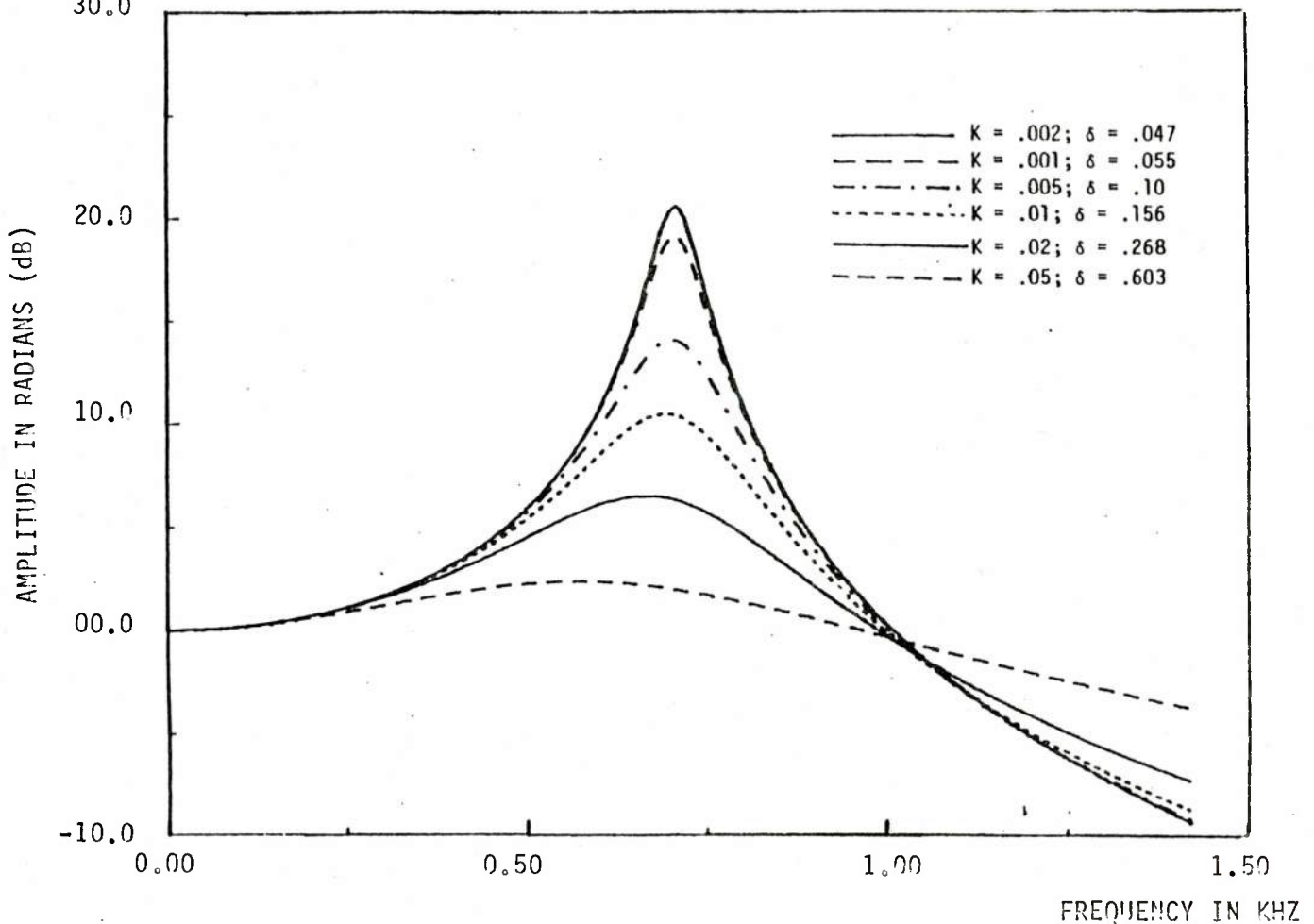


Fig. 23 - Amplitude response for various values of K;  $G = 500$ ,  $\lambda = 200$

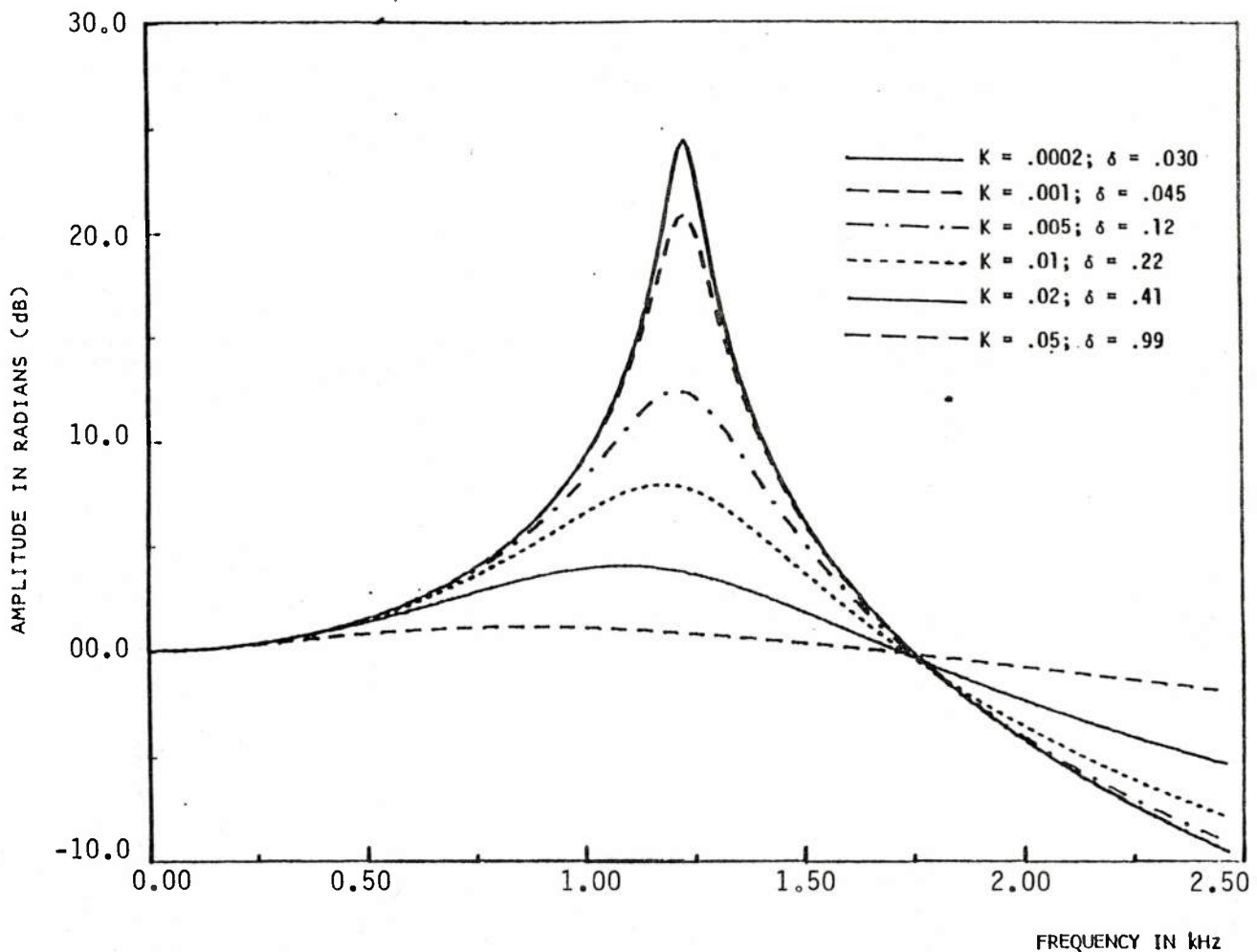


Fig. 24 - Amplitude response for various values of  $K$ ;  $G = 1500$ ,  $\lambda = 200$

The two plots in Figs. 23 and 24 serve just to exemplify the improvements incurred by adding compensation, but do not serve to present total insight to the situation. The root-locus [27] technique depicts the effect of the loop-filter compensation more clearly (not to mention that it serves as an excellent design tool). The root-locus is simply a plot of the migration of the closed-loop poles in the system as the loop gain is varied. This graphical technique can predict the damping and estimate the natural frequency for any system. Figure 25 shows the migration of the closed-loop poles in the second and third quadrants of the complex plane for  $K = 0.01$ ,  $\lambda = 2$ , and variable  $G$ . Since the system is second order, there are two branches (one in the second quadrant and one in the third quadrant); they start (for  $G = 0$ ) at the open-loop poles (for this case, both are at  $s = -\lambda_1$ ) and form semicircles in the second and third quadrants with increasing  $G$ . As the gain is increased even further, the branches meet at the negative real axis at approximately  $-2\lambda_3$  and split off in opposite directions staying on the real axis. Each point on the plot represents a gain spacing of 790; no values for gain are shown on the real axis.

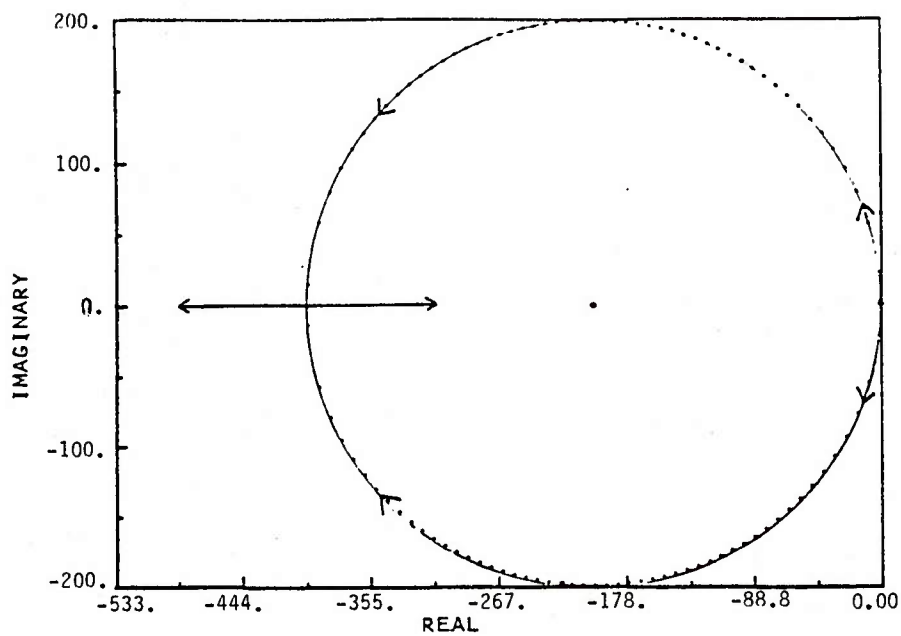


Fig. 25 - Root locus plot for  $K = 0.01$  and  $\lambda = 2$

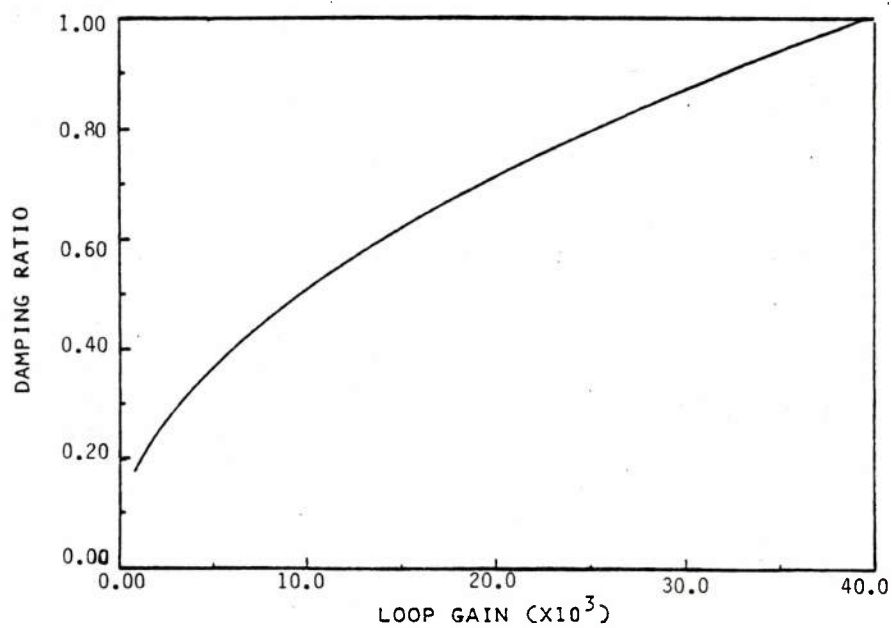


Fig. 26 - Damping ratio plotted versus loop gain;  $K = 0.01$ ,  $\lambda = 2$

This type of plot allows one to look at the pole migrations and have a good feel for what system damping is. Figure 26 shows the damping ratio plotted as a function of gain for the system ( $\lambda = 2$ ,  $K = 0.01$ ,  $G$  variable). It does not require much effort to infer that any root-locus plot for the particular lag-lead configuration chosen ( $\lambda_1 = \lambda_2$ ) leads to a circle of center  $-(\lambda_1 + \lambda_3)$  with radius  $\lambda_3 - \lambda_1$  that starts at  $-\lambda_1$  with branches forming mirror-image semicircles about the negative real axis to meet at  $-(2\lambda_3 + \lambda_1)$  and branch off in opposite directions along the real axis, one to terminate at  $-\infty$  while the other terminates at  $-\lambda_1$  (for infinite  $G$ ). The tremendous advantage of the lag-lead filter is seen when it is compared to a system without compensation. The root-locus and resulting damping ratio for a system with no compensation (over the same range of gain depicted in Fig. 25) is shown in Figs. 27 and 28, respectively. The extremely low damping, which implies poor stability, should be noticed. One might also take interest in noting that this situation (Fig. 27) may also be created with a lag-lead configuration where  $\lambda_3$  is placed at  $-\infty$ .

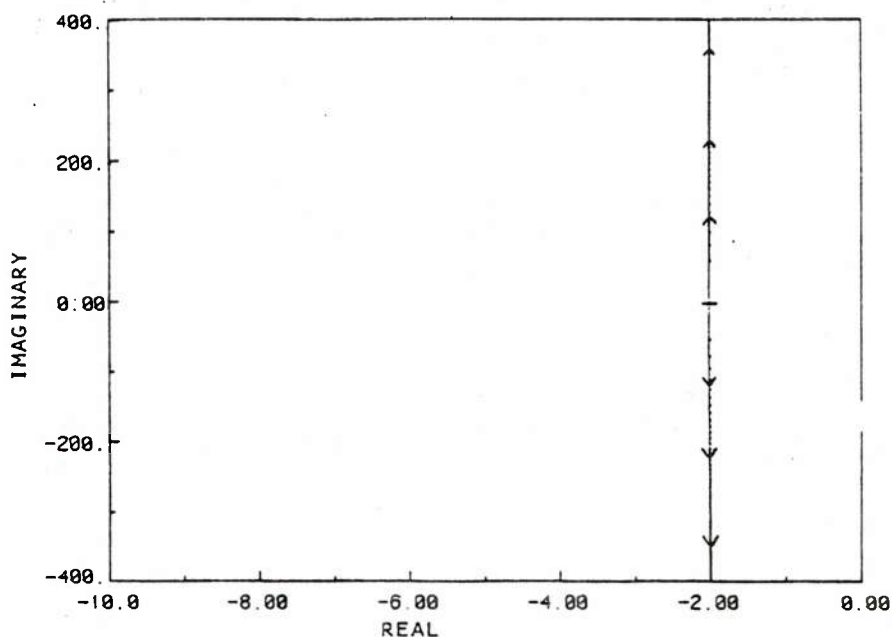


Fig. 27 - Root locus for uncompensated HPFI with  $\lambda = 2$

An interferometric system was set up to verify this theory. For this particular experiment, a setup similar to that shown in Fig. 5 was used. The acoustic input was replaced by a linear phase modulator (fiber wrapped around a PZT-4, 5-cm-diam, thin-walled cylinder) driven with band-limited (to 5 kHz), white (zero-meant), gaussian noise. The system gain  $G$  was determined by setting  $R_3$  to 0, observing  $f_n$ , and using Eq. (46). For this case,  $G$  was found to be approximately 1200. The inverse time constant  $\lambda_1$  was also set to be a constant at 500. Figure 29 illustrates



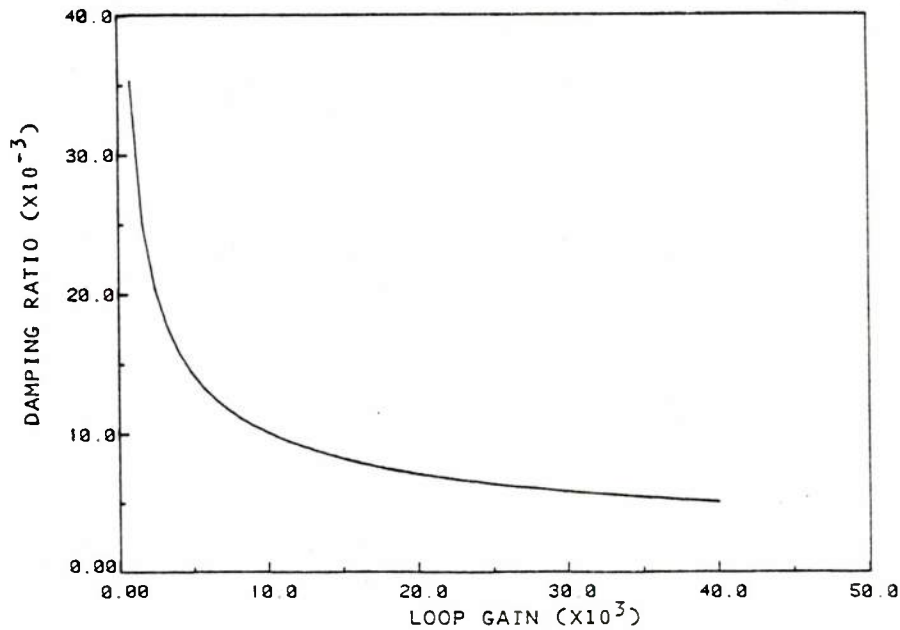


Fig. 28 - Damping ratio plotted versus loop gain  
for uncompensated HPFI with  $\lambda = 2$

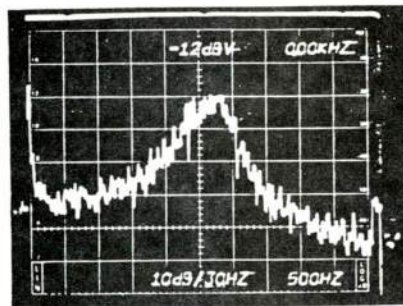
the experimental results when  $K$  takes on values of 0, 0.0031, 0.0077, and 0.015, which predict corresponding damping factors of 0.029, 0.082, 0.162, and 0.295 [from Eq. (65)]. Since white noise produces a flat spectrum, these plots represent the system transfer function  $H(s)_c$ .

It would not be out of reason for one to question the need for spending so much time (in analysis) on the noncompensated HPFI. The author's response to this question is that it is much easier to thoroughly analyze the noncompensated system and draw parallels to the compensated system. A detailed logical insight to this response follows.

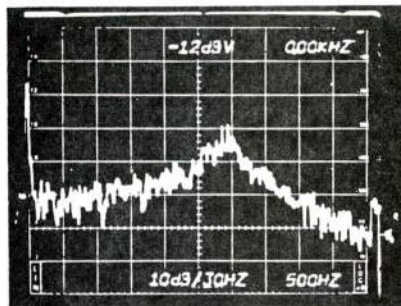
If the compensated HPFI is modeled (assuming "0" initial conditions), the resulting nonlinear equation is

$$\ddot{\phi}_m + 2\lambda_1 \dot{\phi}_m + \lambda_1^2 \phi_m = G\lambda_1^2 \sin(\phi_i - \phi_m) + G\lambda_1 K \frac{d}{dk} [\sin(\phi_i - \phi_m)]. \quad (66)$$

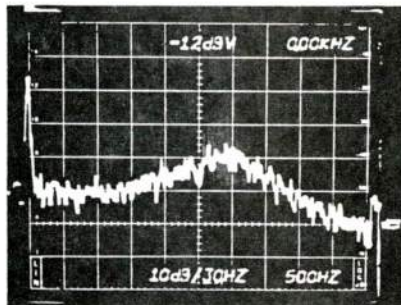
Notice that this equation is exactly the same as Eq. (25) except for the additive term on the right-hand side. It is relatively easy to observe (as before) that for slowly varying  $\phi_m$



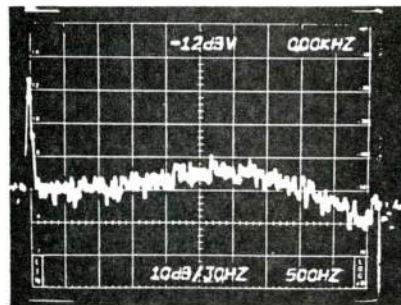
$K = 0$   
 $\delta = .029$



$K = .0031$   
 $\delta = .082$



$K = .0077$   
 $\delta = .162$



$K = .015$   
 $\delta = .295$

Fig. 29 - System response for various compensations;  
 $\lambda_1 \approx \lambda_2 = 500$ ,  $G = 1200$ ; vertical axis at  
 10 dB per division, horizontal axis at  
 500 Hz per division

$$\phi_m = G \sin(\phi_i - \phi_m), \quad (67)$$

leading to  $\phi_m^{\max} = G$ , which is exactly the same as the noncompensated system, which implies that for a large enough  $G$ , the system behaves linearly.

If one were to try to demonstrate linearity for the higher frequencies of  $\phi_m$ , they would be presented with great difficulties when trying to use Eq. (66) to explicitly solve for  $\phi_i(\omega_c)$  [as in Eq. (39)]. It is much easier to assume values for  $K$  to make the right-hand term of Eq. (66) negligible. This leaves one with Eq. (25), which has been shown to behave linearly for  $\phi_i \leq 4\lambda_1$  and  $\lambda \leq 1$ .

The natural frequency for the compensated HPFI can also be estimated with solutions from the uncompensated HPFI. The author has yet to differentiate Eq. (62) with respect to  $\omega$  and set the result to zero to obtain an expression for  $\omega_n$ . From Figs. 23 and 24, one is able to see that when  $K$  is very small, the system becomes uncompensated, which is a reasonable assumption for  $K = 0.0002$ . Notice that for all values of  $K$  in Figs. 23 and 24 that  $f_n$  remains relatively unchanged. Close inspection reveals that

$$f_n \approx \frac{\lambda_1 \sqrt{G-1}}{2\pi} \quad \left| \begin{array}{l} G > 100 \\ \delta < 0.3, \end{array} \right. \quad (68)$$

which is seen to be the same as Eq. (66).

## NONLINEAR ANALYSIS

The theoretical development in the previous chapter was developed from the point of view that the HPFI was never operated in a region of instability or loss of synchronization. The most obvious example of the HPFI losing synchronization occurs when the input phase  $\phi_i$  exceeds  $G$ , the loop gain. This is most easily observed in the low-frequency case where Eq. (30) demonstrates that  $\phi_m$  cannot possibly take on a value greater than  $G$  and, hence, the system loses synchronization. The linear model of the HPFI does not address this loss of synchronization as it is a nonlinear process. This example suggests the HPFI's complete response to any input can be observed only via the nonlinear model. If the nonlinear model for the HPFI could be solved, one might be able to produce answers to the following questions:

- When is the linear model a good approximation to the nonlinear system?

•What conditions cause the system to lose synchronization?

•How does the system respond to a loss of synchronization?

As there is no closed-form technique to solve for the nonlinear expression in Eqs. (25) and (66), it is nearly impossible to provide generalized solutions. It is, however, possible to simulate this nonlinear system to provide specialized solutions for given inputs. This is accomplished by constructing a difference equation from the nonlinear differential equation and iteratively implementing it in a computer. This chapter develops the difference equation and utilizes it to demonstrate the system response for various inputs.

## The Nonlinear Model Approximated with Discrete Modeling

### Development of the Nonlinear Discrete Model

The most generalized expression that models the HPFI (with or without compensation) is described in Eq. (66). This equation is nonlinear as the dependent variable  $\phi_m$  is contained within the argument of the sine function (which creates orders of  $\phi_m$  higher than 1). The equation can be approximated in the discrete sense by constructing a difference equation.

If  $\phi_m(t + k\Delta t)$  is represented by a new variable  $\phi_{n+k}$  ( $k = 0, \pm 1, 2, 3, \dots$ ), one sees that if  $\Delta t$  is kept constant that the subscript ( $n+k$ ) for the new variable denotes the value of  $\phi_m$  at the discrete time  $t + k\Delta t$ . It is possible to define the discrete derivative to simulate a continuous derivative evaluated at a point in the following fashion:

$$\dot{\phi}_m(t) \approx \frac{\phi_{n+1} - \phi_{n-1}}{2\Delta t}, \quad (69)$$

which is, of course, exactly true in the limit as  $\Delta t$  approaches "0". In a similar manner,  $\ddot{\phi}_m(t)$  may be approximated as follows

$$\begin{aligned} \ddot{\phi}_m(t) &\approx \frac{\frac{\phi_{n+1} - \phi_n}{\Delta t} - \frac{\phi_n - \phi_{n-1}}{\Delta t}}{\Delta t} \\ &= \frac{\phi_{n+1} - 2\phi_n + \phi_{n-1}}{(\Delta t)^2}. \end{aligned} \quad (70)$$

Equations (69) and (70) may be substituted in Eq. (66) to construct a difference equation. Starting with Eq. (66)

$$\ddot{\phi}_m + 2\lambda_1 \dot{\phi}_m + \lambda_1^2 \phi_m = G\lambda_1^2 \sin(\phi_i - \phi_m) + G\lambda_1 K \frac{d}{dt} [\sin(\phi_i - \phi_m)]. \quad (71)$$

Substituting the continuous variables with the discrete variables, one sees

$$\begin{aligned} & \frac{\phi_{n+1} - 2\phi_n + \phi_{n-1}}{(\Delta t)^2} + \frac{\lambda(\phi_{n+1} - \phi_{n-1})}{\Delta t} + G\lambda^2 \sin(\phi_i - \phi_n) \\ & + G\lambda K \left\{ \frac{d}{dt} [\phi_i(t)] - \frac{\phi_{n+1} - \phi_{n-1}}{2\Delta t} \right\} \cos(\phi_i - \phi_n). \end{aligned} \quad (72)$$

This equation may be arranged to solve explicitly for  $\phi_{n+1}$  to yield

$$\begin{aligned} & \frac{\Delta t^2 \lambda^2 G \sin(\phi_i - \phi_n) + \frac{GK}{\lambda} \frac{d}{dt} \phi_i(t) + \frac{\phi_{n-1}}{2\Delta t} \cos(\phi_i - \phi_n) - \phi_n}{1 + \lambda \Delta t + G\lambda \Delta t K \cos(\phi_i - \phi_n)/2} \\ & + \frac{\phi_{n-1}(\Delta t \lambda - 1) + 2\phi_n}{1 + \lambda \Delta t + G\lambda \Delta t K \cos(\phi_i - \phi_n)/2} = \phi_{n+1}. \end{aligned} \quad (73)$$

In this expression,  $\lambda_1 = \lambda_2 = \lambda$  and  $K = \lambda_2/\lambda_3$ . This relationship describes the "next state" of the system providing the two previous states ( $\phi_n$  and  $\phi_{n-1}$ ) and the input value  $\phi_i$  are given. It should be somewhat obvious that the equation be used in an iterative method to solve (or approximate) successive next states by simply letting the subscript  $n$  take on the value  $n+1$  or  $n+2$  or  $n+3$ , and so on. A digital computer is a most useful tool for this type of implementation. One must be cautious, however, when selecting values for  $\Delta t$  as the computer may introduce error as it rounds off numbers. This occurs for values of  $\Delta t$  that are too small. Errors may also be introduced when the choice of  $\Delta t$  is too large. These occur primarily relating to the lack of resolution the system model provides when simulating some continuous operation. Before the discrete model is to be used to approximate system outputs relating to given inputs, one must insure that the parameters chosen for the model do not introduce extraneous effects.

## Verification of the Nonlinear Discrete Model

To insure that the difference equation in Eq. (69) is accurately predicting the system response, one must devise a method to test it.



This test should address such questions as:

- Does the model work?
- Are the chosen parameters for the model adequate?

One method called the phase-plane plot [28] used for demonstrating system stability or instability proves to be a good test for the difference equation. The phase-plane technique plots the trajectory of the HPFI's output (phase) versus its time derivative. For  $\phi_i(t)$  being a step perturbation at  $t = 0$ , the phase-plane represents a plot of the system's step response versus its time derivative. The trajectory for a stable system would result in  $\dot{\phi}_m = 0$  while  $t$  approaches infinity. If the linear model and the approximation to the nonlinear model are to show likenesses, then as  $t$  approaches infinity, the value for  $\phi_m$  will approach  $S[G/(1+G)]$  as predicted by Eq. (56) as  $\dot{\phi}_m$  approaches zero. For this case,  $S$  represents the amplitude of the input step.

Figure 30 shows a phase-plane plot for a compensated system via iterative use of Eq. (73). For this case,  $\lambda = 100$ ,  $K = 0.0001$ ,  $G = 200$ ,  $S = 1$ , and  $\Delta t = 0.0001$ . The result here depicts what the linear model would predict. It shows a damped oscillation of  $\phi_m(t)$  responding to a unity step input that decays to a steady-state value of  $\phi_m(t) = 0$  and  $\dot{\phi}_m(t) = 0.995$ , which coincides exactly with what Eq. (56) would predict.

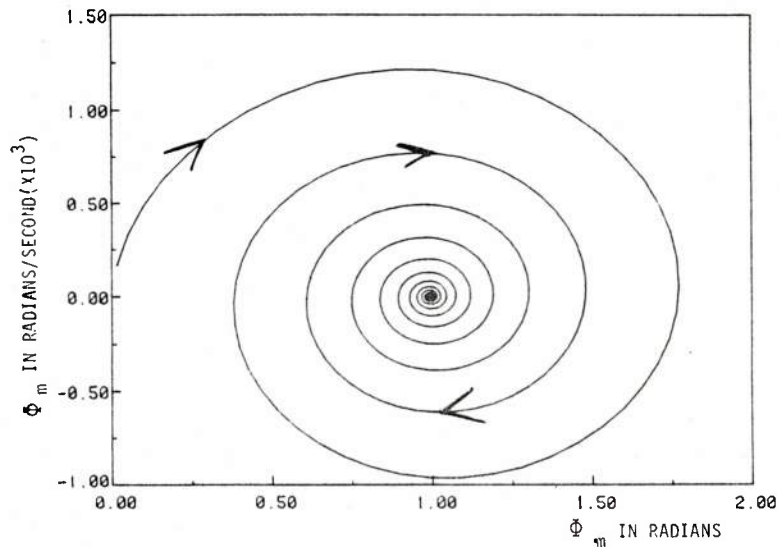


Fig. 30 - Phase-plane plot for a unity step input;  
 $G = 200$ ,  $\lambda = 100$ , and  $\Delta t = 0.0001$

Figures 31, 32, and 33 demonstrate a system simulation with parameters exactly the same as in Fig. 30, but taken with larger time increments ( $\Delta t = 0.004$ ,  $0.0012$ , and  $0.002$  s, respectively). The discrete



nature of this iterative approximation is much more evident in these plots. One would think that such a large time increment would produce disastrous results; but from the point of view of the step response, Figs. 31 and 32 show stable configurations that attain the same steady-state value predicted by the linearized model. In Fig. 33, the time increment finally becomes too large and the model generates an unstable system.

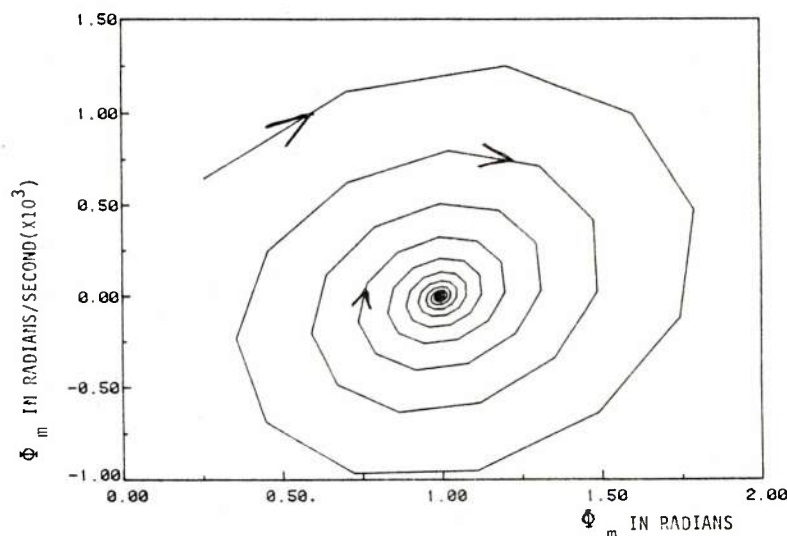


Fig. 31 - Phase-plane plot for a unit step input;  
 $G = 200$ ,  $\lambda = 100$ , and  $\Delta t = 0.0004$

With the previous results at hand, a question is raised concerning a proper choice of  $\Delta t$ . It has been observed that three different choices of  $\Delta t$  generate stable predictable steady-state responses (albeit they appear to be very different). The most reasonable choice would be to go with the smallest time increment as it better approximates a continuous system (as the system actually operates).

The next question for one to address is how small an increment should one take for an adequate representation. It is most obvious that one would not like to take an infinitesimally small increment as computer time is expensive and it is also possible to generate computer round-off errors. The computer used to iteratively implement Eq. (73) is a DEC Model PDP 11-45, and it was found that computer time was much more of a problem than were round-off errors.

The optimized time increment to choose would be one that is as large as possible without distorting the system (as does the time increment chosen in Figs. 31 and 32). The natural frequency  $f_n$ , as described by

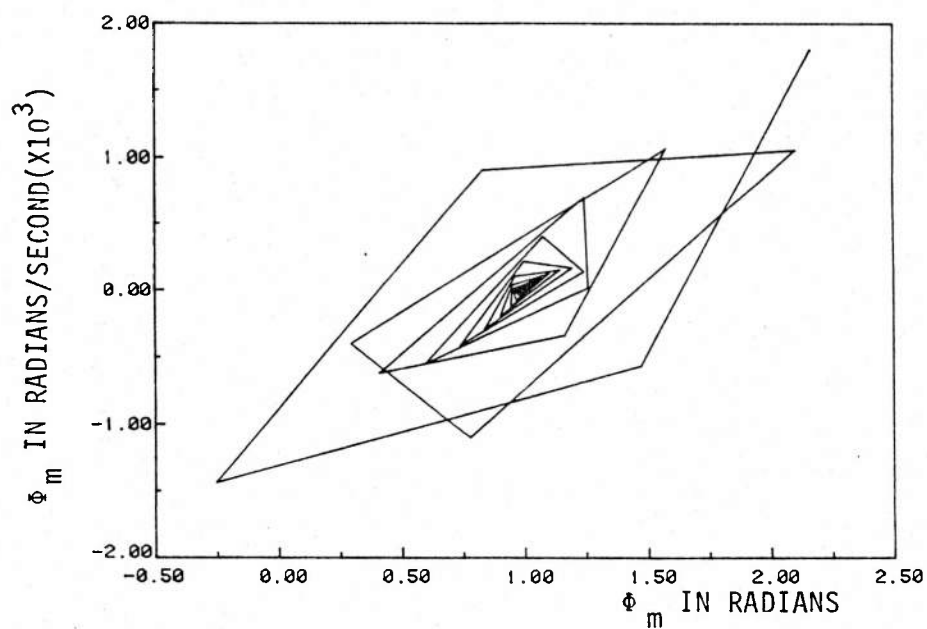


Fig. 32 - Phase-plane plot for a unity step input;  
 $G = 200$ ,  $\lambda = 100$ , and  $\Delta t = 0.0012$

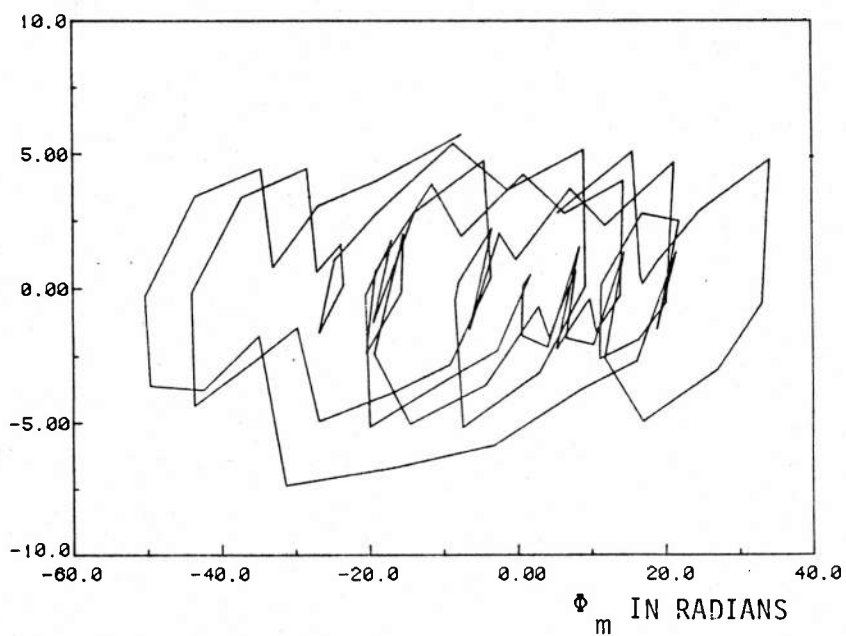


Fig. 33 - Phase-plane plot for a unity step input;  
 $G = 200$ ,  $\lambda = 100$ , and  $\Delta t = 0.002$

Eqs. (46) and (68), has been seen (in previous analysis) to be the highest unattenuated frequency found in the HPFI. It is also a good approximation to the resonant frequency of the HPFI. Since the HPFI responds to all discontinuities by exciting its resonant frequency, one need only to pick a time increment for the discrete model that accurately represents the resonant frequency approximated by the natural frequency [Eq. (68)]. A reasonable time increment (deduced by inspection of the phase-plane plots) would be one that produces 50 data points per one cycle at the system's natural frequency (for  $G > 50$ ). Choosing fewer data points would produce the results shown in Figs. 31, 32, and 33. Although the systems in Figs. 31 and 32 are stable, the paucity of points per cycle at the higher frequencies will generate a signal distortion that results in harmonic distortion. From this point on, any implementation of the discrete model will use a time increment less than  $(50 f_n)^{-1}$  or

$$\Delta t \leq \frac{1}{50 f_n} = \frac{2\pi}{50\lambda\sqrt{G-1}}, \quad (74)$$

which insures a stable system devoid of harmonic distortion.

Before leaving the subject of the phase-plane, it is interesting to observe the effects of system damping. Figure 34 demonstrates the HPFI setup with  $G = 500$ ,  $\lambda = 200$ ,  $\Delta t = 2.5 \times 10^{-5}$ ,  $S = 1$ , and  $K = 0.002, 0.007$ , and  $0.02$ , respectively, producing damping ratios of  $0.047, 0.12$ , and  $0.27$ . Each system was simulated for a 5-ms duration starting at the time of the step input. Notice how the systems with higher damping ratios stabilize faster.

Now that the nonlinear model for the HPFI has been constructed, one may judge its effectiveness by comparing it to the linearized model. Proper modeling will be evident if there is a high degree of similarity between the results of both models. To compare these models, their step and sinusoidal responses were investigated.

To obtain the step response of the linearized model, one starts with Eq. (66), substitutes  $\phi_i - \phi_m$  for  $\sin(\phi_i - \phi_m)$ , and solves the second-order equation for  $\phi_m$  assuming  $\phi_i = 1$  starting at  $t = 0$ . If  $\lambda_1$  is assumed to be equal to  $\lambda_2$ , the resulting solution is

$$r(t)_c = \frac{KG\lambda_1\lambda_3}{B} + e^{-At} \frac{z}{g} \cos(mt) - \frac{f}{g} \sin(mt), \quad (75)$$

where  $A = \lambda_1(2 + GK)/2$

$$B = \lambda_1^2(1 + G)$$

$$m = \sqrt{B - A^2}$$

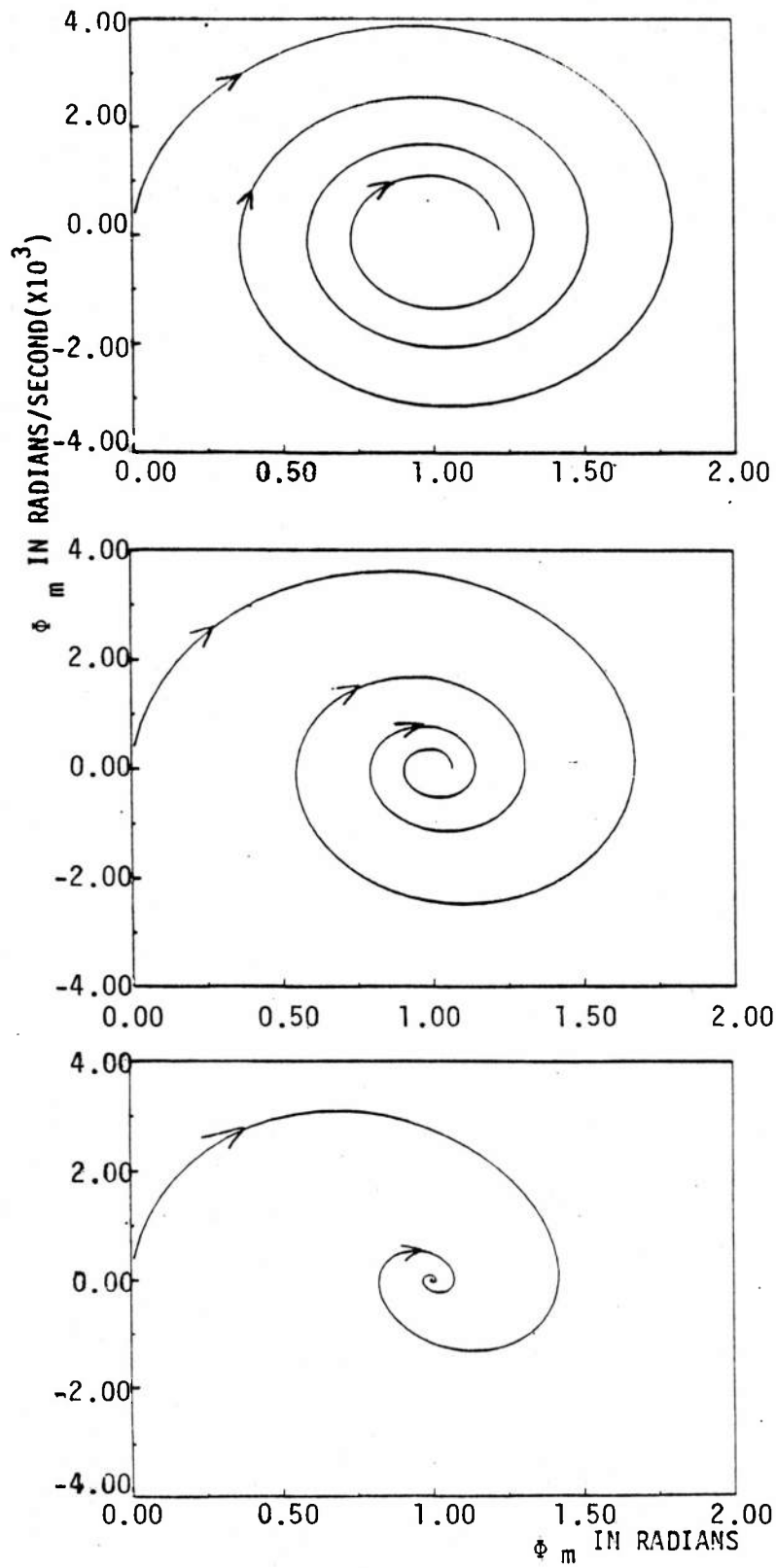


Fig. 34 - Phase-plane plot for unity step input to systems with varying damping factors;  $G = 500$ ,  $\lambda = 200$ ,  $\Delta t = 2.5 \times 10^{-5}$

$$a = KG\lambda_1(\lambda_3 - A)$$

$$b = KG\lambda_1 m$$

$$c = -m^2$$

$$d = -Am$$

$$z = ac + bd$$

$$e = ac - bd$$

$$f = bc - ad$$

$$g = c^2 + d^2.$$

This solution is compared to the prediction of the nonlinear model for various damping ratios and loop parameters. Figure 35 displays the comparison for  $G = 1500$  and  $\lambda = 1000$  with  $\delta = 0.05, 0.10$ , and  $0.32$ . Figure 36 displays the comparison for  $G = 2500$  and  $\lambda = 1000$  with  $\delta = 0.025, 0.07$ , and  $0.27$ . Both figures show a very close comparison for the amplitude response but are off somewhat for the phase. This ambiguity in phase is understandable in that the HPFI is operating under non-steady-state conditions. When steady-state conditions prevail, both models predict the same value. To further corroborate this statement, the linearized sinusoidal response [Eq. (63)] will be compared to the nonlinear model's sinusoidal response.

Figure 37 shows the responses of both models to an HPFI configured with  $G = 5000$ ,  $\lambda = 1000$ , and  $\delta = 0.05$  for a 50-Hz input signal. In this case, the results from both models are indistinguishable. Figure 38 shows the sinusoidal response at 1000 Hz for  $G = 1000$ ,  $\lambda = 1000$ , and  $\delta = 0.11$ . One can see here the transient behavior manifested in the nonlinear model. This behavior should similarly be evident in the linear model, but it has been omitted as Eq. (63) only predicts the steady-state approximation of the linearized system. Notice as the nonlinear model approaches steady state, the two plots converge to almost identical values.

This simple comparative analysis should indeed provide evidence that the linear and nonlinear models represent the same system.

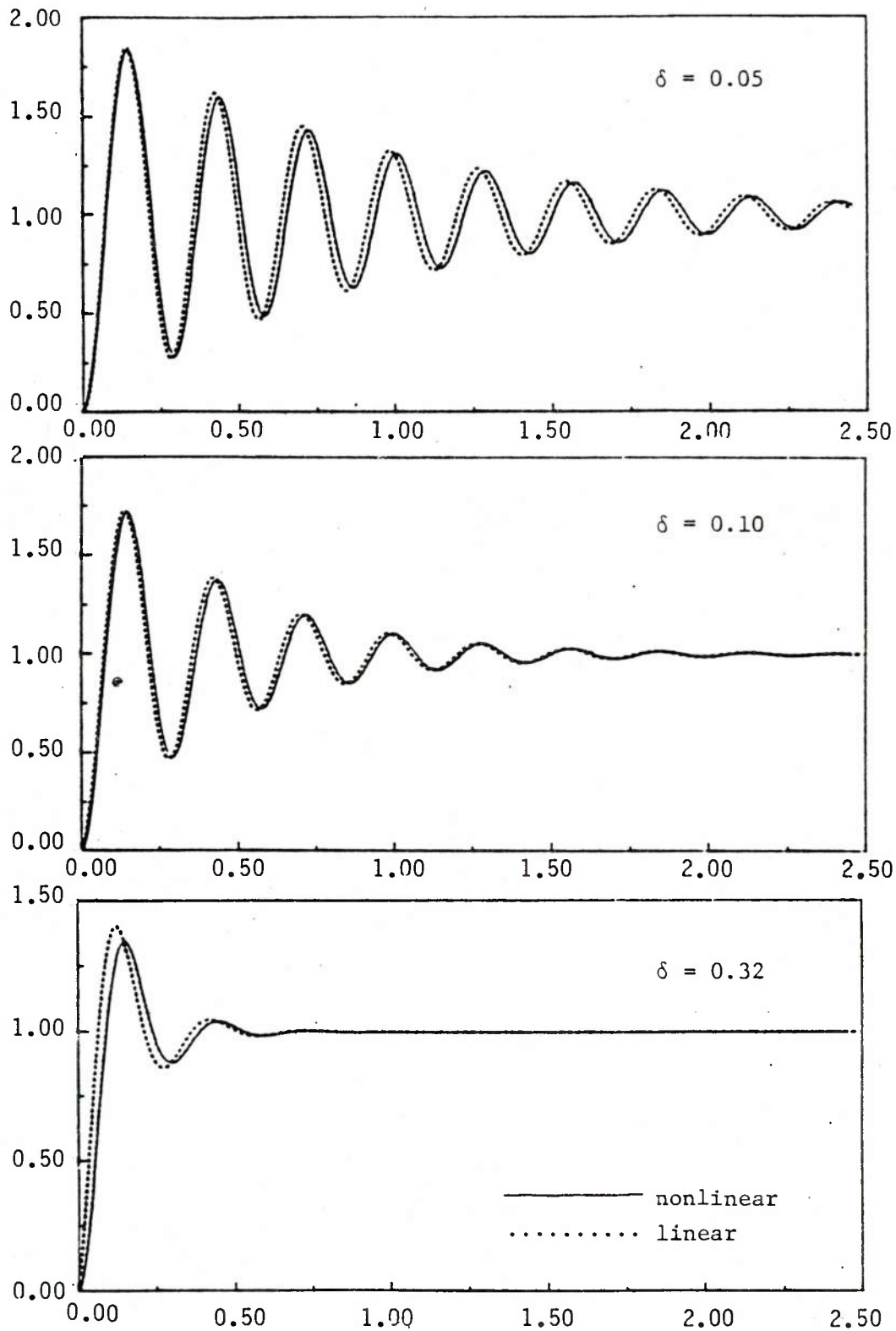


Fig. 35 - Comparison of the step response of the linear and nonlinear models for the compensated HPFI;  $G = 500$ ,  $\lambda = 1000$ , and  $\delta$  is varied



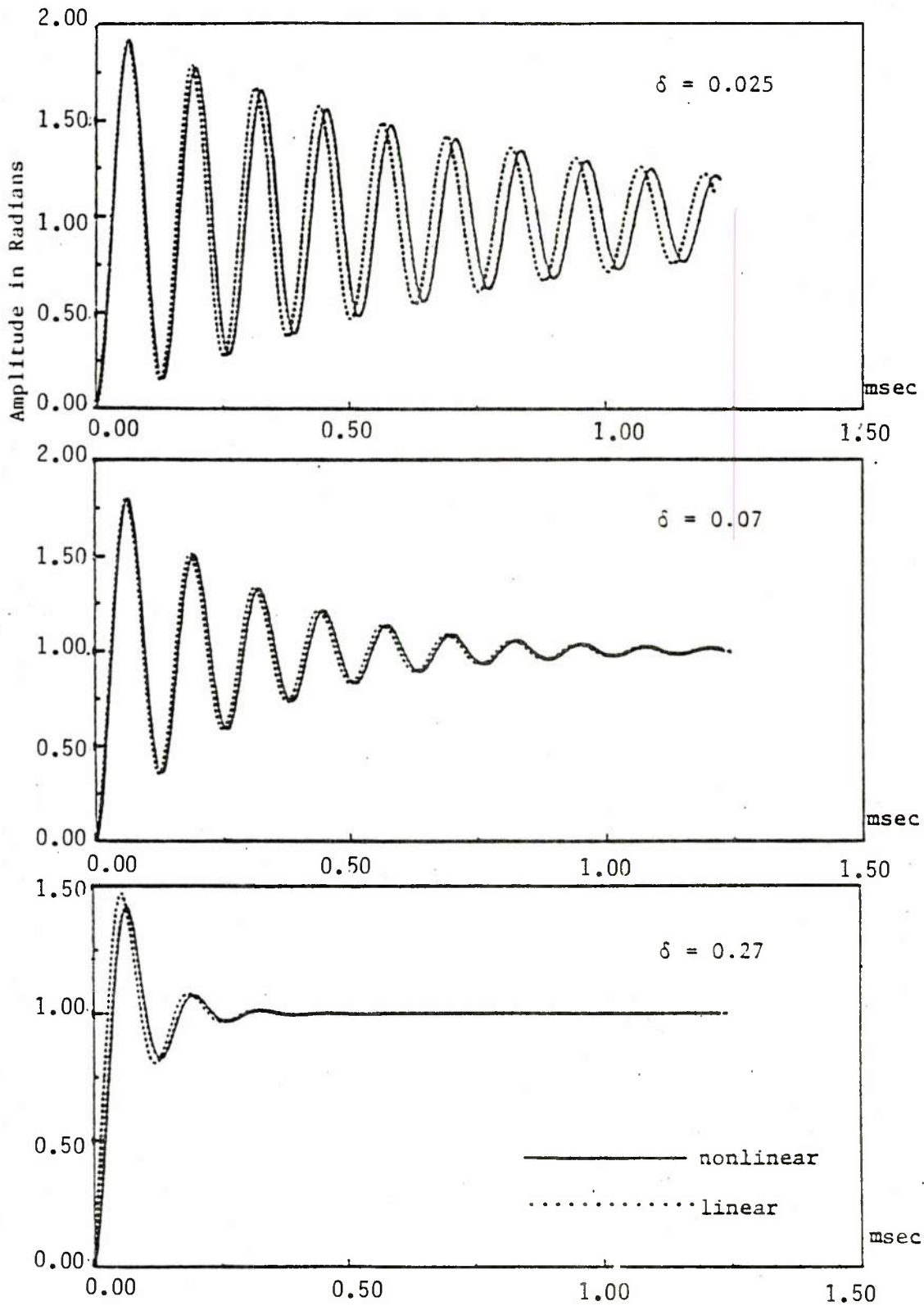


Fig. 36 - Comparison of the step response of the linear and nonlinear models for the compensated HPFI;  $G = 2500$ ,  $\lambda = 1000$ , and  $\delta$  is varied

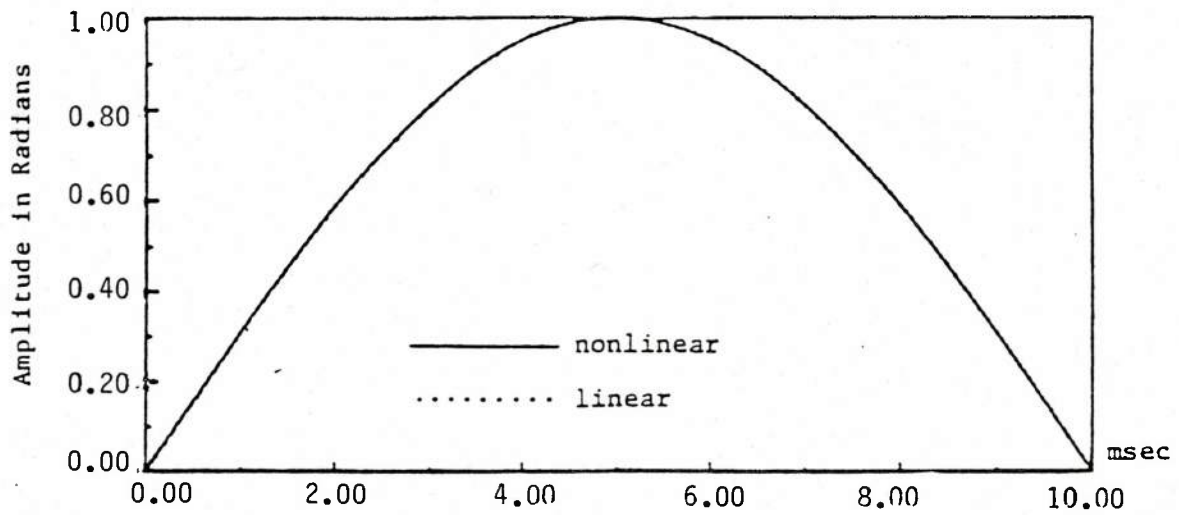


Fig. 37 - Comparison of the sinusoidal response of the linear and nonlinear models for the compensated HPFI;  $G = 5000$ ,  $\lambda = 1000$ ,  $\delta = 0.05$ , and  $f = 50$  Hz

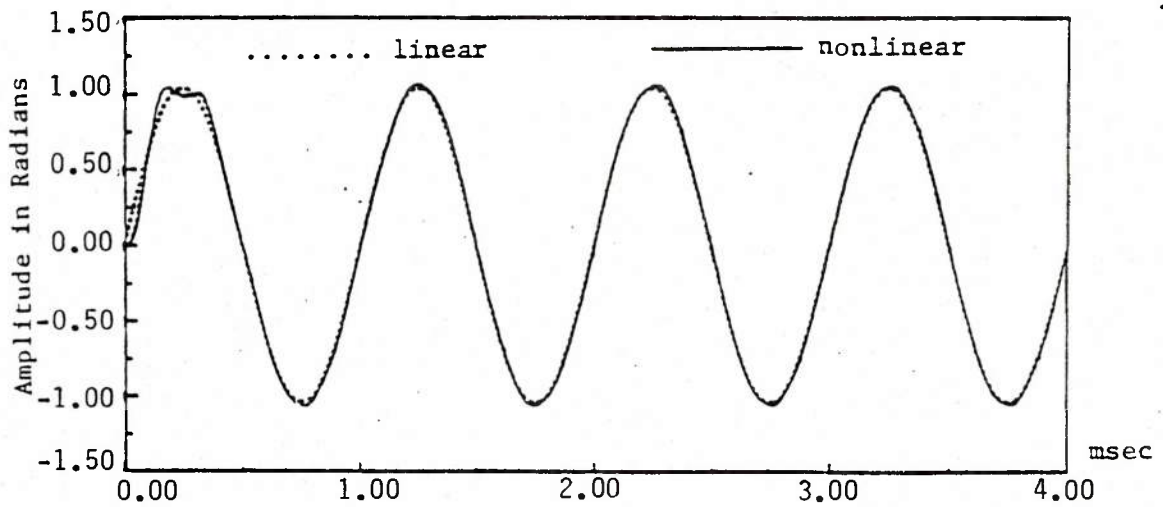


Fig. 38 - Comparison of the sinusoidal response of the linear and nonlinear models for the compensated HPFI;  $G = 1000$ ,  $\lambda = 1000$ ,  $\delta = 0.11$ , and  $f = 1000$  Hz

## Application of the Nonlinear Discrete Model

### The Step Response

The step response of the HPFI was completely covered in the last section. One aspect that might not have been covered is the time-domain response for the step function. Figure 39 demonstrates the time-domain response of the HPFI configurations seen in Fig. 34. The time for this duration is also 5 ms.

### The Ramp Response

The ramp response of the HPFI provides some very interesting information particular to the system's loss of synchronization and its reacquisition. A straightforward method to induce the system to lose synchronization would be to allow  $\phi_i(t)$  to be a ramp of a moderately slow slope (with respect to system parameters) and observe the model's behavior as  $\phi_i$  exceeds  $G + \pi/2$ . An example of this is shown in Fig. 40. Here  $G = 200$ ,  $\lambda = 400$ ,  $K = 0.0001$  ( $S = 0.071$ ),  $\Delta t = 2 \times 10^{-5}$ , and  $r(t) = 250$  rad/s. In this figure,  $\phi_m$  is plotted versus  $\phi_i$ . When  $\phi_m$  attains its maximum value ( $G$ ), the HPFI loses synchronization and  $\phi_m$  responds by plummeting to a lower value where the system parameters allow reacquisition to continue tracking the ramp.

This loss of lock and reacquisition is a very complicated process (being nonlinear in nature). The curious researcher will naturally be interested in the mechanisms of this process. The results in Fig. 40 are not very amenable in providing much information to describe these mechanisms; perhaps the phase-plane plot is more revealing. Figure 41 displays the phase-plane plot of an HPFI having the same parameters as the system modeled in Fig. 40. This plot starts at the onset of the loss of synchronization ( $\phi_m = 200$ ) and follows the system through to reacquisition and then steady-state tracking of the ramp input signal.

In this case, it is clearly seen that as soon as the system loses synchronization,  $\phi_m$  becomes accelerated with a negative magnitude. This initial acceleration is so great that even when  $\phi_m$  has regressed  $\pi$  rads, into a region where the system's acceleration ( $\ddot{\phi}_m$ ) turns positive (in an attempt to stabilize), the system's negative momentum (described by  $\dot{\phi}_m$ ) is too great to be reversed. It is clearly demonstrated that the acceleration that resists the declining motion of  $\phi_m$  does not overcome it until  $\phi_m$  drops to a value of approximately 20 rads. This phenomenon can readily be verified by observing the explicit relation for  $\ddot{\phi}_m$  using the continuous uncompensated model (a simplification of the compensated HPFI) in Eq. (25).

$$\ddot{\phi}_m = G\lambda^2 \sin(\phi_i - \phi_m) - 2\lambda\dot{\phi}_m - \lambda^2\phi_m \quad (76)$$

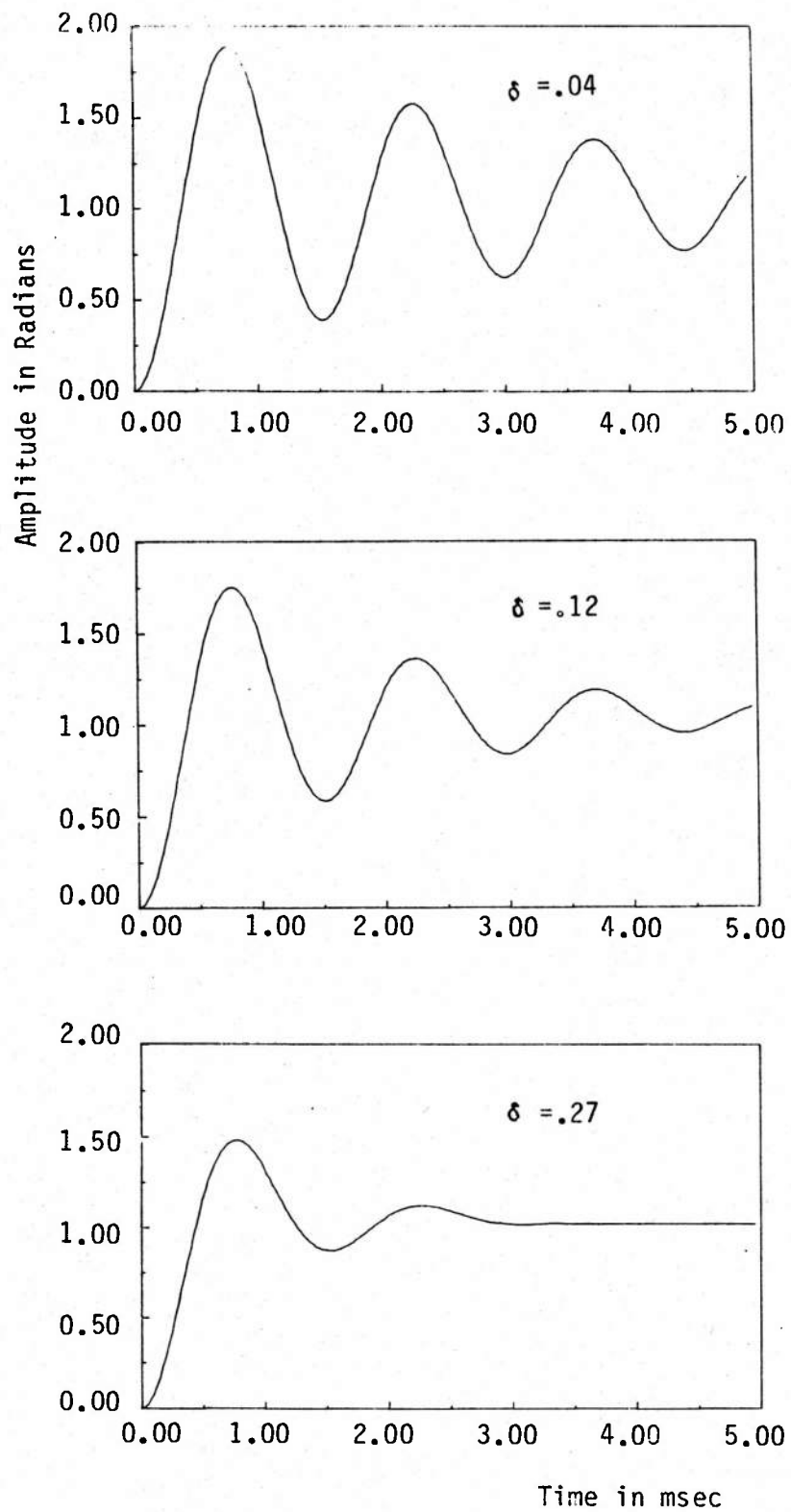


Fig. 39 - Step response for  $G = 500$  and  $\lambda = 200$   
for various damping ratios

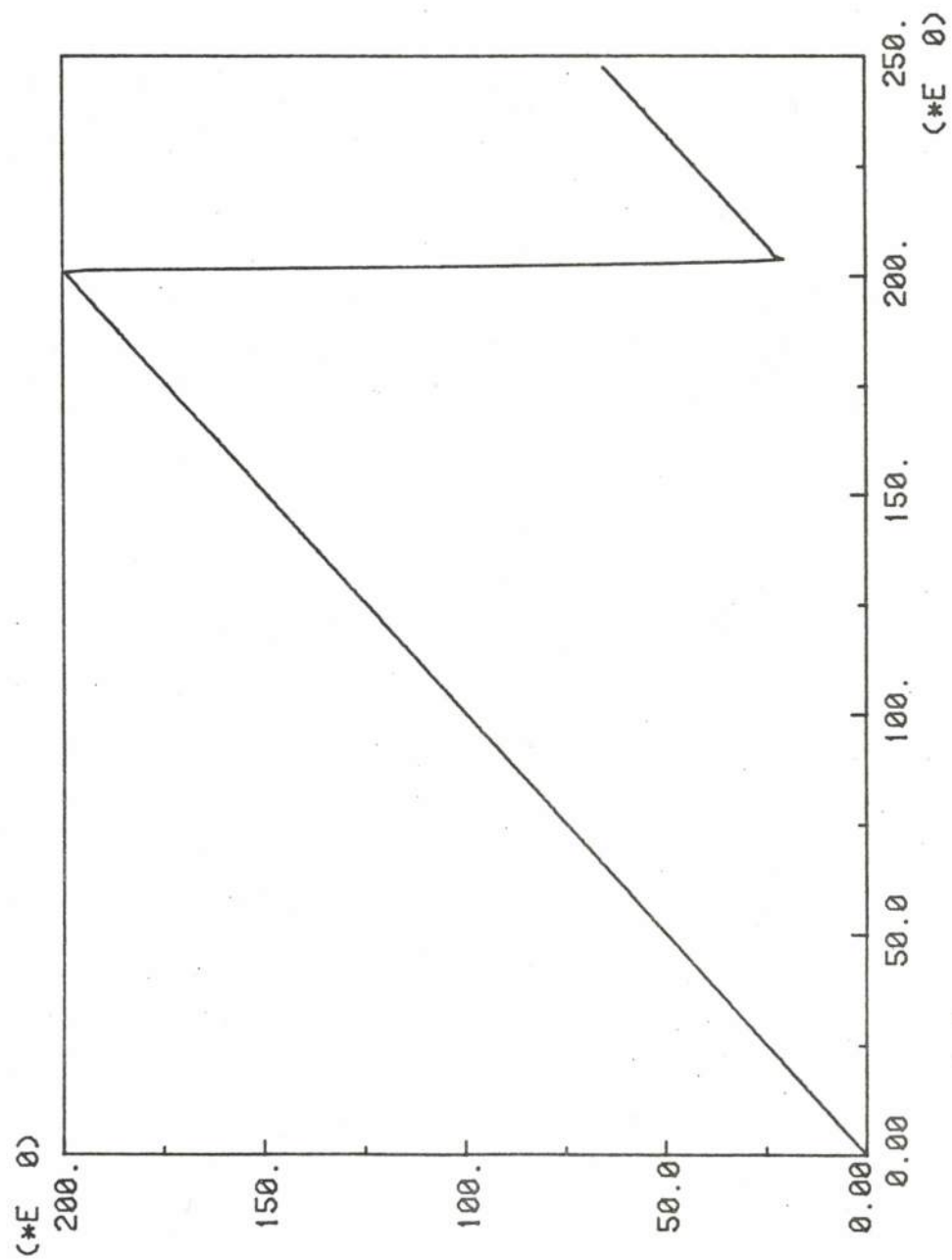


Fig. 40 - Ramp response for  $G = 200$ ,  $\lambda = 400$ , and  $K = 0.0001$

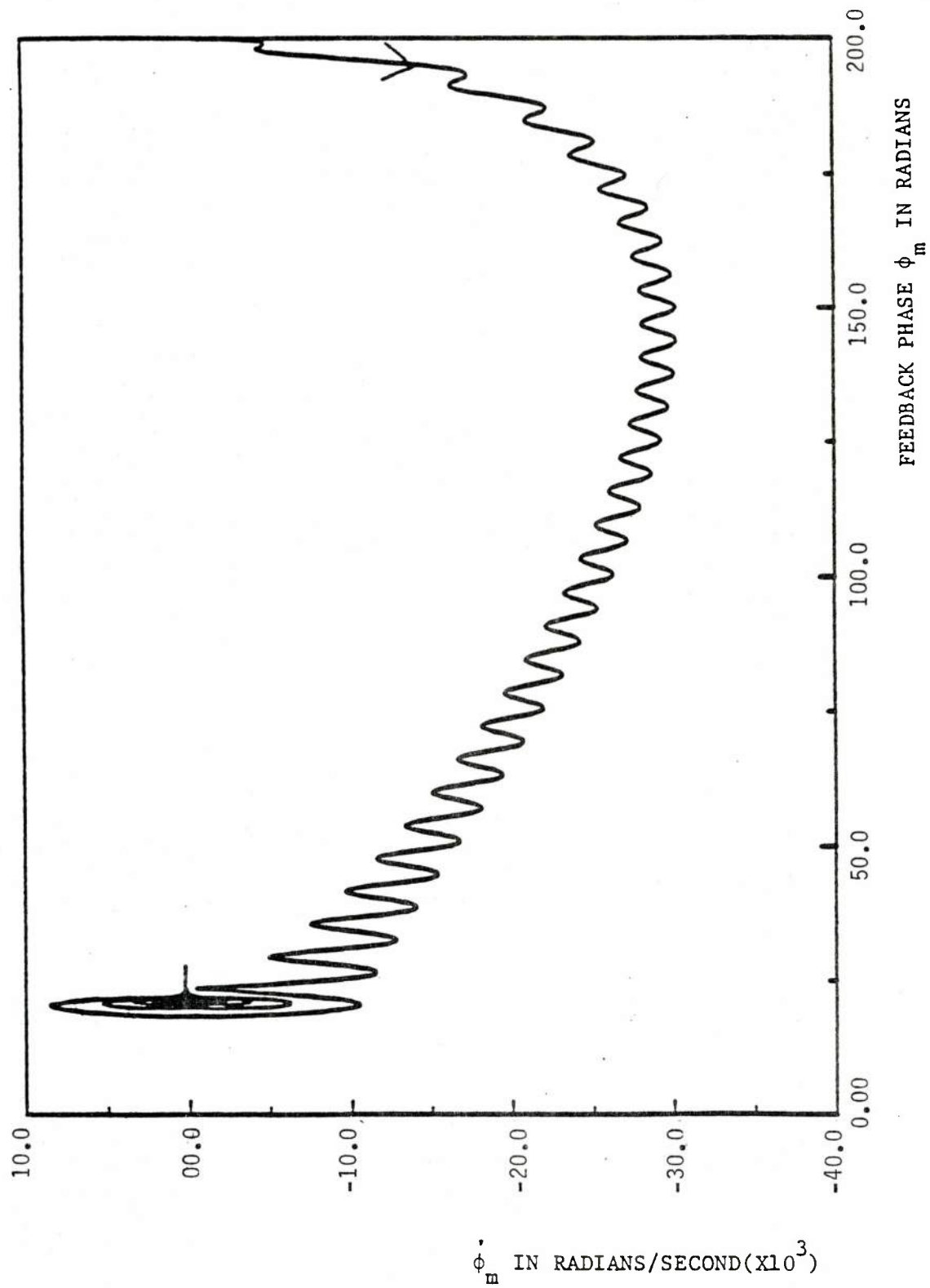


Fig. 41 - Phase-plane plot showing the loss and reacquisition of synchronization;  $g(t) = 250$  rads/s,  $G = 200$ ,  $\lambda = 400$ , and  $K = 0.0001$



One will notice that when  $\dot{\phi}_m$  becomes smaller, the acceleration term ( $\ddot{\phi}_m$ ) becomes more and more positive, which opposes the negative motion of  $\dot{\phi}_m$  and in turn slows down  $\dot{\phi}_m$  to the point where the system regains synchronization. Figure 42 demonstrates a "close-up" view of the phase-plane plot shown in Fig. 41. It shows the system regain synchronization, then exhibit a response that looks like the step response demonstrated in the previous section; but it differs somewhat as the system is tracking the input signal, which is a ramp. The system finally assumes steady state at  $\dot{\phi}_m = 250$  rads/s. Figures 43 and 44 show the phase-plane plot for two other configurations of the HPFI with the same  $f_n$  as in Fig. 41 (900 Hz). In Fig. 43,  $G = 500$ ,  $\lambda = 250$ ,  $K = 0.0001$ , and  $r(t) = 250$  rads/s. In Fig. 44,  $G = 100$ ,  $\lambda = 565$ ,  $K = 0.0001$ , and  $g(t) = 250$  rads/s. Notice that all three systems regain lock at different values of  $\dot{\phi}_m$ ; but in each case, the range of  $\dot{\phi}_m$  is the same, being approximately  $\pm 10,000$  rads/s. This type of phenomenon is very similar to what is described as the "capture range" of a phase-locked loop. This analogy may be corroborated when choosing a different  $f_n$  and observing the range of  $\dot{\phi}_m$  required for re-acquisition. Figure 45 shows the results of performing just such an experiment. In this case,  $f_n$  was chosen to be four times that seen in Figs. 41, 43, and 44. The results show that the capture range for  $\dot{\phi}_m$  is now approximately  $\pm 40,000$  rads/s (four times the previous sample), which agrees with the prediction as the bandwidth of the loop filter incurred a fourfold increase.

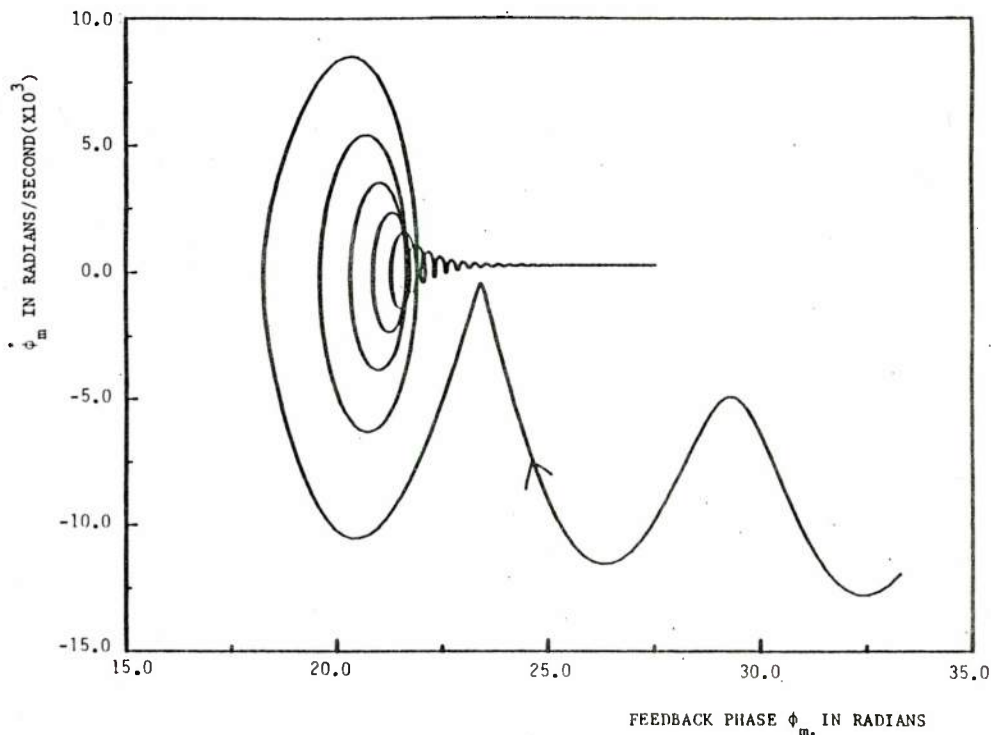


Fig. 42 - Phase-plane plot,  $g(t) = 250$  rads/s,  
 $G = 200$ ,  $\lambda = 400$ , and  $K = 0.0001$

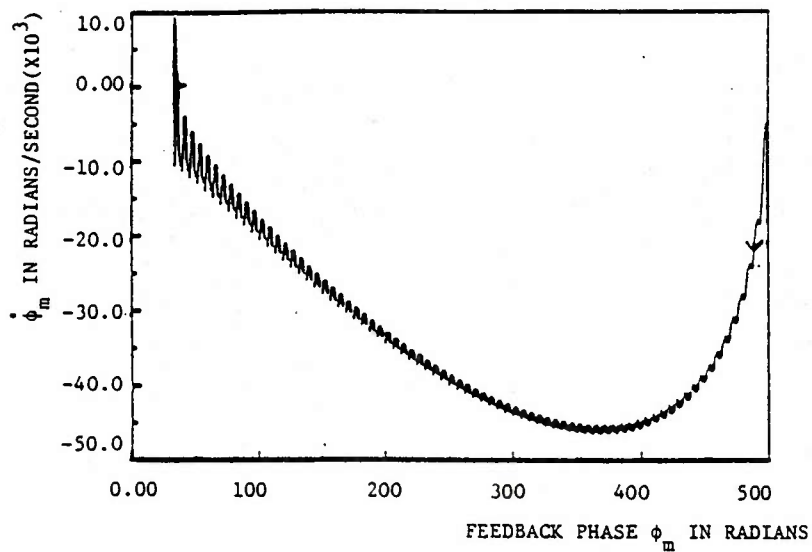


Fig. 43 - Phase-plane plot for  $g(t) = 250$  rads/s,  
 $G = 100$ ,  $\lambda = 565$ , and  $K = 0.0001$

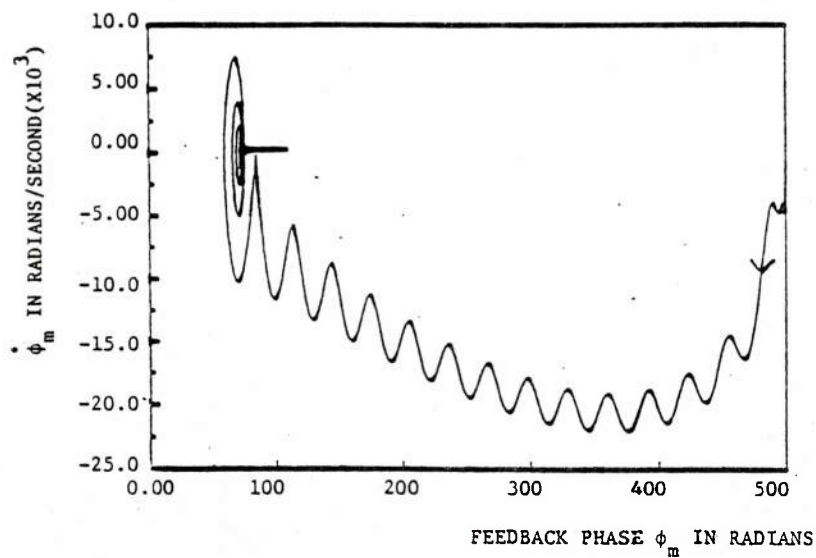


Fig. 44 - Phase-plane plot for  $g(t) = 250$  rads/s,  
 $G = 100$ ,  $\lambda = 565$ , and  $K = 0.0001$

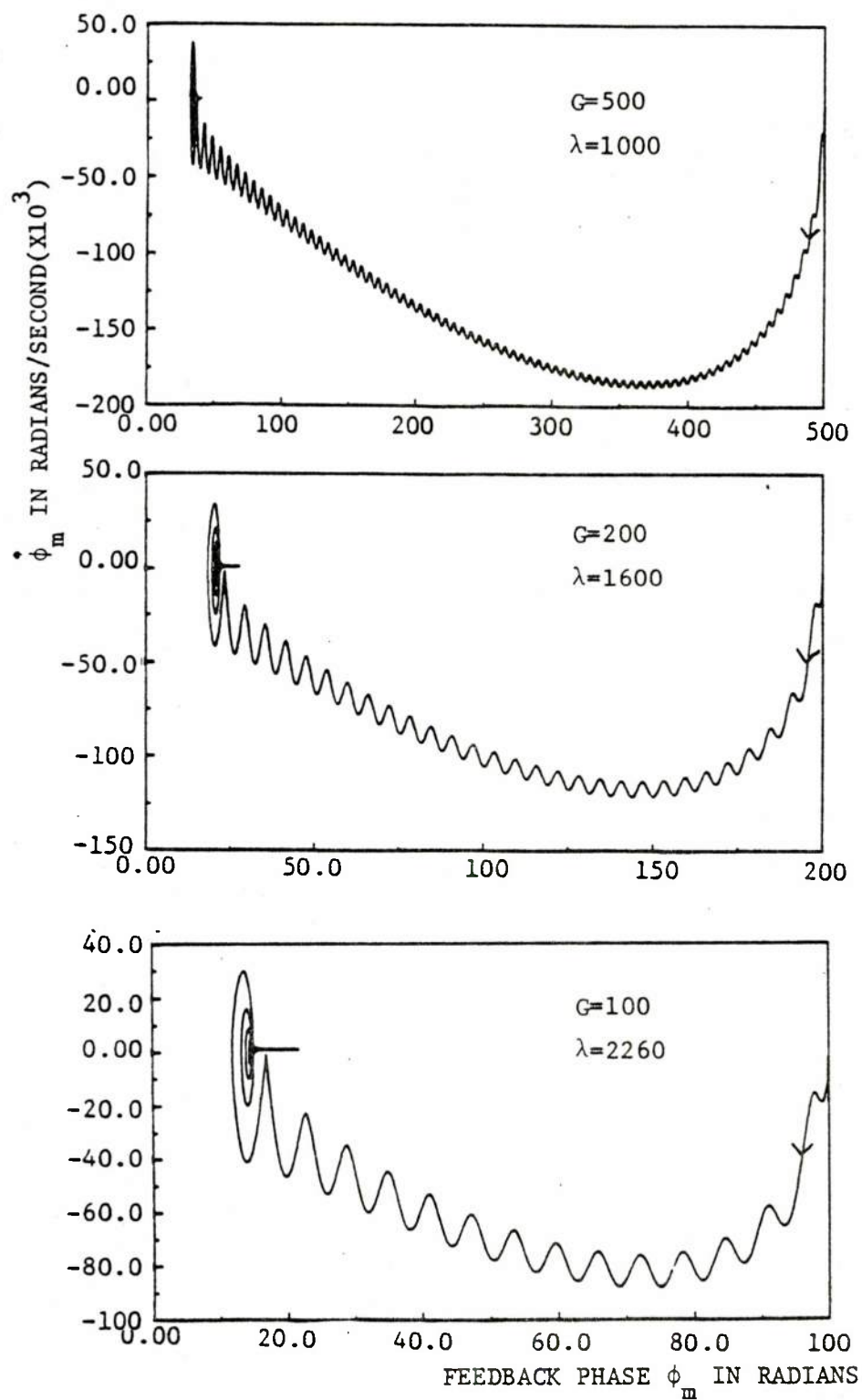


Fig. 45 - Phase-plane plot for  $g(t) = 1000$  rads/s

It can be stated that the capture range  $\dot{\phi}_c$  for the HPFI is approximately 1.75 times that of the natural rad frequency, or

$$\dot{\phi}_c \approx 1.75\omega_n \quad \delta < 0.1 \quad (77)$$

This relation has been observed only for systems with low damping (relatively uncompensated). When the systems are compensated, producing damping factors greater than 0.1, one would expect some change in Eq. (77). A heuristic analysis of this situation will ensue. Figure 46 demonstrates an HPFI with  $G = 200$ ,  $\lambda = 400$ ,  $g(t) = 250$  rads/s, and  $\Delta t = 20$   $\mu$ s. In this case,  $\phi_m$  is plotted versus  $\phi_i$  for the ramp input. The solid line represents a system for which  $\delta = 0.071$ , the long dashed line represents  $\delta = 0.105$ , and the short dashed line represents  $\delta = 0.371$ . It is plainly evident that the larger the system damping the faster the HPFI regains synchronization. This phenomenon can be accomplished only by the HPFI having a larger capture range. This insight is proved true by observing the transfer functions seen in Figs. 23 and 24. It is demonstrated that when the damping ratio is increased, the Q of the system is reduced or the bandwidth is broadened. It is this broadening of the bandwidth that may be attributed to the increase in capture range for the compensated HPFI.

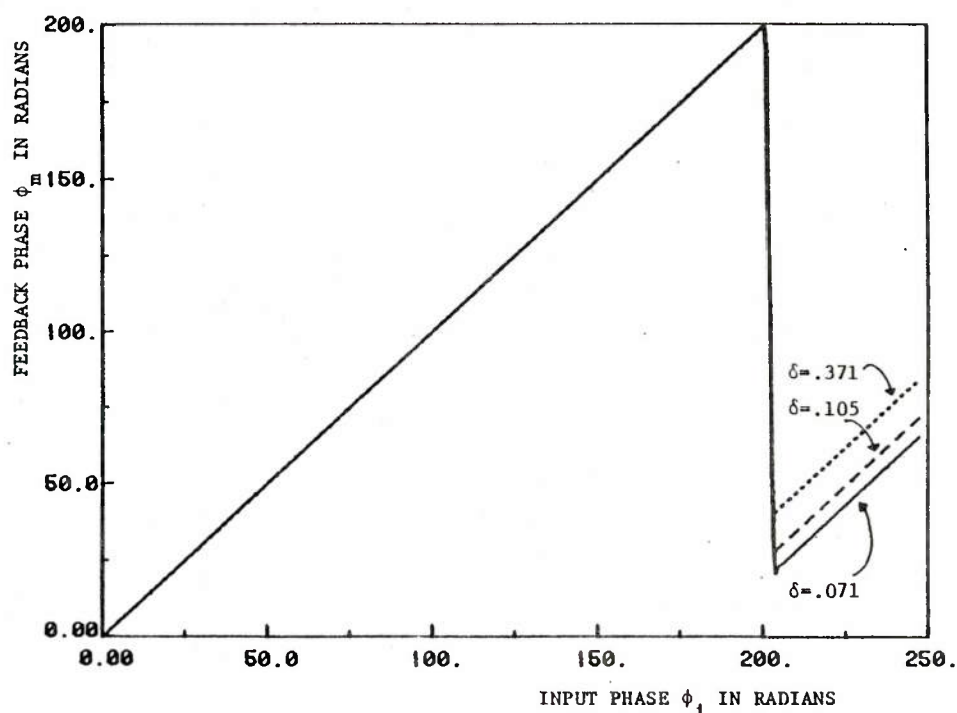


Fig. 46 - Ramp response of the HPFI for damping ratios of 0.071, 0.105, and 0.371;  $G = 200$  and  $\lambda = 400$

It is very possible to construct an HPFI in the laboratory where the amplifier providing the feedback has a maximum output level that is less than what the system parameters allow. For example, suppose the system is constructed so that  $G = 200$  but the feedback amplifier's maximum output allows the HPFI an excursion of only  $\pm 60$  rads. The discrete model incorporating the ramp response provides some very useful information concerning just such a system. If the discrete model is modified to accommodate the restricting limits of  $\phi_m$ , the feedback amplifier limited system may be simulated. Figure 47 depicts just such a process. Here  $G = 200$ ,  $\lambda = 400$ ,  $g(t) = 250$  rads/s,  $|\phi_m| \leq 60$  (due to amplifier restrictions), and  $\delta = 0.071$ . It is surprising to note that the system does not lose lock immediately when  $\phi_m$  becomes 60 rads. This result is quite obvious, however, when one observes Eq. (25) assuming  $\ddot{\phi}_m = \dot{\phi}_m = 0$  and setting the limit of  $\phi_m$  to 60. It is seen that any value of  $\phi_i$  between 60.3 and 62.4 will satisfy the relation.

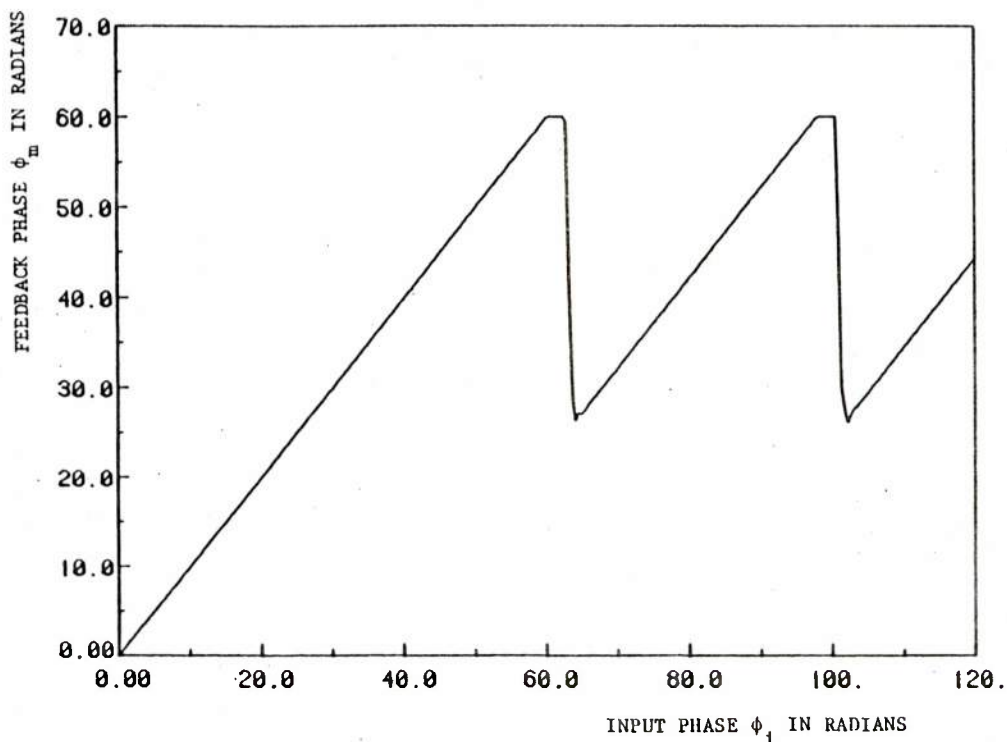


Fig. 47 - Ramp response of the HPFI limited by the range of the feedback amplifier;  $G = 200$ ,  $\lambda = 400$ , and  $g(t) = 250$  rads/s

Before leaving the ramp response, one more interesting point concerning the HPFI's performance may be investigated. When the system loses synchronization and resets itself,  $\phi_m(t)$  may be approximated as a "step" change in value of some very large magnitude. It is interesting to note that the system does not recover by responding to such a large step but responds to a step no greater than  $\pi/2$ . This is realized as the HPFI operates over a  $\pm\pi/2$  degeneracy. Any signal on which it synchronizes is discernable only by the value of the phase error  $\phi_e$ . Since the phase error can take on values of only  $-\pi/2 \leq \phi_e \leq \pi/2$ , the HPFI can respond only to steps having a magnitude less than  $\pi/2$ . Figure 48 demonstrates a system regaining synchronization with parameter values of  $G = 500$ ,  $\lambda = 250$ ,  $g(t) = 250$  rads/s, and  $\delta = 0.047$ .

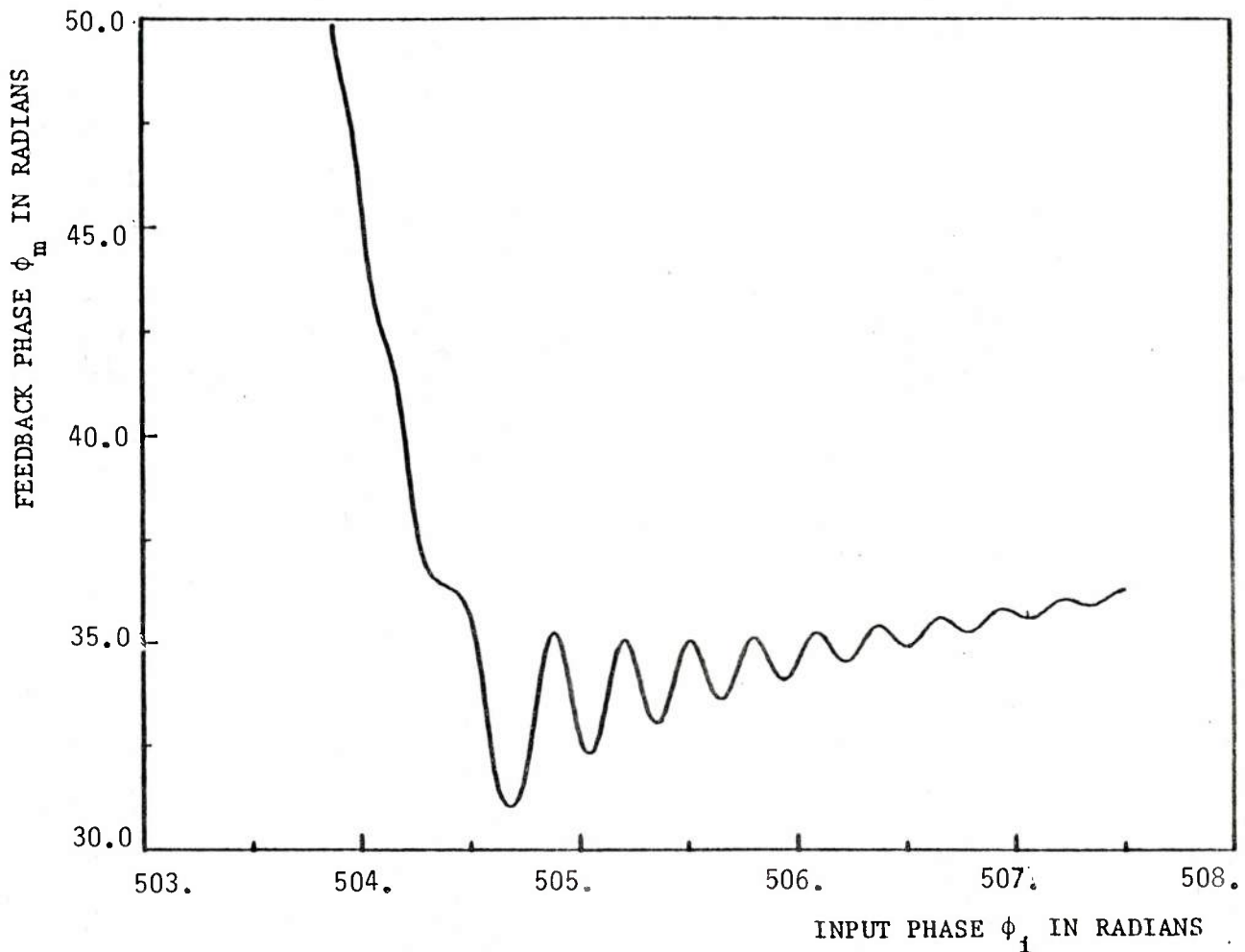


Fig. 48 - Ramp response of the HPFI as it regains synchronization;  
 $G = 500$ ,  $\lambda = 250$ ,  $g(t) = 250$  rads/s, and  $\delta = 0.047$



## The Sinusoidal Response

The sinusoidal response of the HPFI modeled discretely will serve to shed some light on determining a value for the maximum allowable sinusoidal signal that the HPFI is capable of tracking. It was brought out in the last section that the HPFI was slew-rate limited as a result of the loop filter. This phenomenon is also evident as the HPFI operates in tracking a sinusoidal input phase of a certain amplitude and frequency. A straightforward way of finding the HPFI's maximum trackable sinusoidal amplitude at any given frequency is to input that frequency to the HPFI while slowly increasing the amplitude and watching for the system to lose synchronization. Figure 49 demonstrates this procedure implemented theoretically using the discrete model. For this simulation,  $f = 400$  Hz,  $\lambda = 2100$ ,  $G = 900$ , and  $\delta = 0.033$ . It is a simple matter of pinpointing the region where the system loses synchronization. If this process is repeated for different frequencies, one will be able to come up with a plot of maximum allowable amplitude as a function of frequency. This theoretical information is presented in Fig. 50 along with experimental results for an HPFI configured for  $G = 435$ ,  $\lambda = 1800$ , and  $\delta = 0.048$ . The experimental results follow the theory for the lower and higher frequencies but are a little off from about 100 to 500 Hz. This probably is attributed to the fact that it was impossible to center the sinusoid about 0 rads in the experiment as very large, random thermal-induced phases (up to 50 rads/s) controlled the operating point. If one inspects Fig. 50, one finds that  $\phi_m$  at the point where the system is losing synchronization (at any frequency) is about ten times larger than  $\omega_n$ . For a different system configuration, this number may be smaller or larger. This type of sinusoidal analysis leads to the theoretical prediction of the dynamic lock range (author defined) of the system.

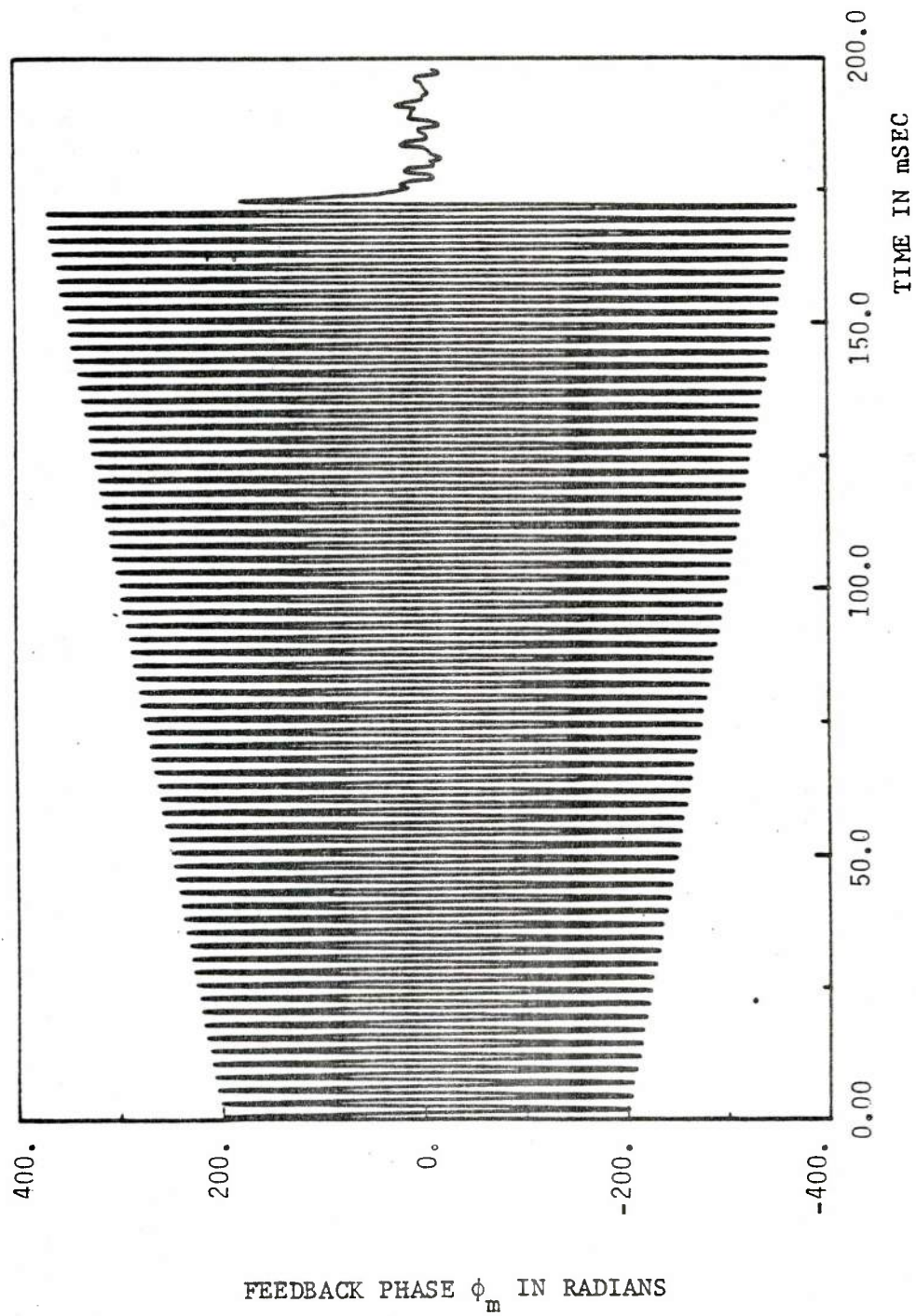


Fig. 49 - Sinusoidal response of the HPFI as the input amplitude is linearly increases;  $f = 400$  Hz,  $\lambda = 2100$ ,  $G = 900$ , and  $\delta = 0.033$

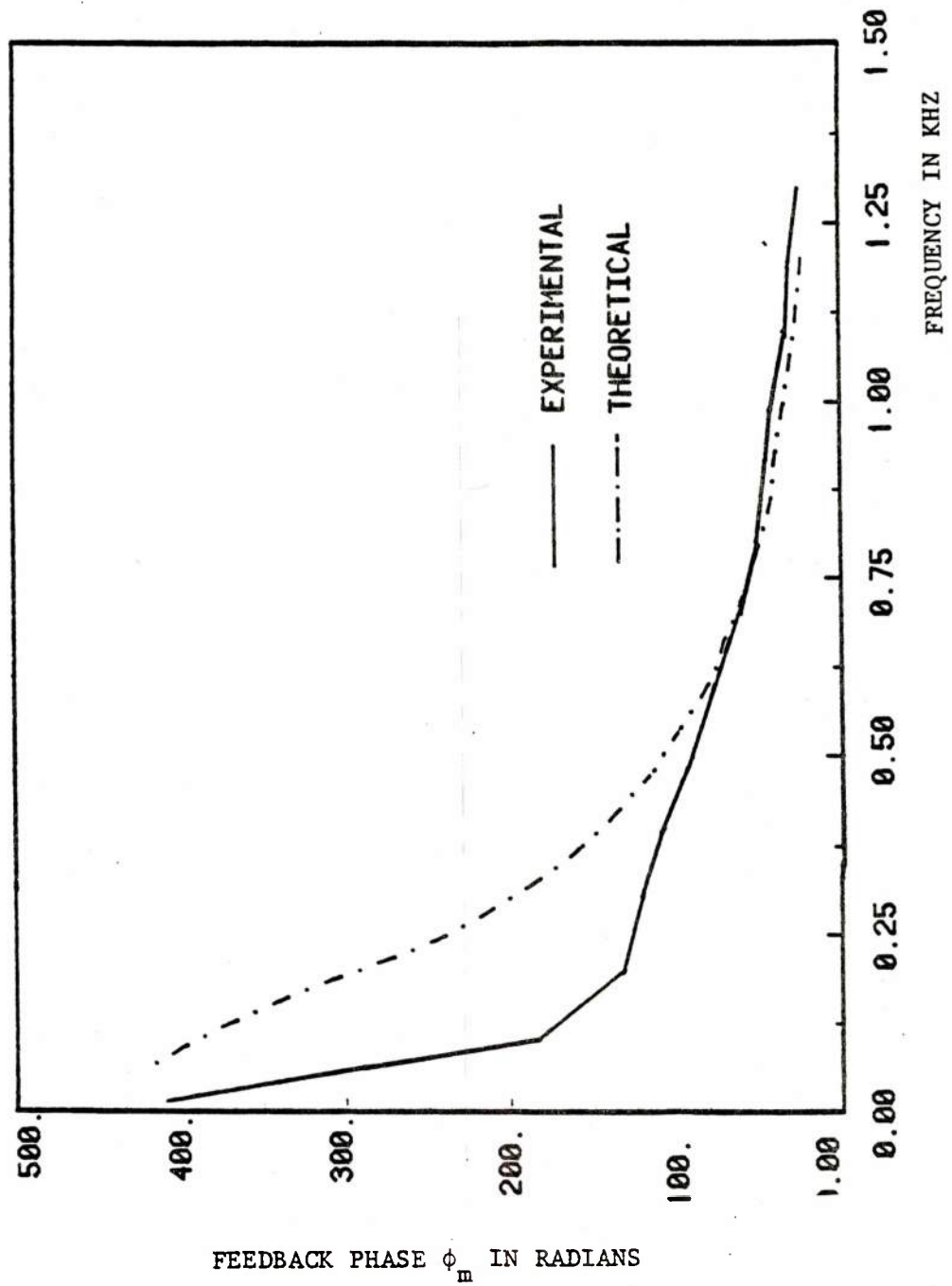


Fig. 50 - Maximum sinusoidal amplitude response for  $G = 435$  and  $\lambda = 1800$

## CONCLUDING REMARKS

This report has been devoted primarily to the theoretical investigation of a unique interferometric stabilization technique, that by no means is complete. Its purpose is merely to lay the groundwork and theoretically generalize the noiseless operation of the HPFI. It was found that the analysis of the HPFI drew many parallels to the analysis of the phase-locked loop. This was no surprise as both systems use nonlinear phase comparison and feedback to synchronize to the input phase.

All of the analysis in this report concerns second-order systems. This choice was intentional as HPFI's with first- or third-order loops place some severe limitations on system performance. The first-order system has practical value only at very low frequencies while the third-order system has operating regions where the system can become unstable. The detailed theoretical analysis to support these statements is omitted as the issue of choice in the order of the HPFI is somewhat peripheral to the scope of this report.

The noise performance of the HPFI is not included in this report. However, it is an important topic not to be overlooked and will be investigated in the very near future.

## REFERENCES

1. E. Hecht and A. Zajac, *Optics*, Addison Wesley Publishing Co., Reading, Mass., 1979, p. 290.
2. J.A. Bucaro, H.D. Dardy, and E.F. Carome, "Optical Fiber Acoustic Sensor," *Appl. Opt.* 16, 1761-1765 (September 1977).
3. J.H. Cole, R.L. Johnson, and P.G. Bhuta, "Fiber Optic Detection of Sound," *J. Acoust. Soc. Am.* 62, 1136-38 (November 1977).
4. S. Ezekiel and S.R. Balsamo, "Passive Ring Resonator Laser Gyroscope," *Appl. Phys. Lett.* 30, 478-82 (March 1977).
5. W.C. Goss, "Fiber-Optic Rotation Sensor Technology," *Appl. Opt.* 19, 852-58 (June 1980).
6. M.R. Layton and J.A. Bucaro, "Optical Fiber Acoustic Sensor Utilizing Mode-Mode Interference," *Appl. Opt.* 18, 666 (March 1980).
7. G.B. Hocker, "Fiber-Optic Sensing of Pressure and Temperature," *Appl. Opt.* 18, 1445-48 (May 1979).
8. M. Tateda, S. Tanaka, and Y. Sugawara, "Thermal Characteristics of Phase Shift in Jacketed Optical Fibers," *Appl. Opt.* 19, 770-73 (March 1980).
9. G.R. Fowles, *Introduction to Modern Optics*, Holt, Rinehart and Winston, N.Y., 1975, p. 315.
10. C.C. Cutler, S.A. Newton, and H.J. Shaw, "Limitation of Rotation Sensing by Scattering," *Opt. Lett.* 5, 488-90 (November 1980).
11. S.K. Sheem and T.G. Giallorenzi, "Single-Mode Fiber-Optical Power Divider: Encapsulated Etching Technique," *Opt. Lett.* 4, 29-31 (January 1979).
12. R.A. Bergh, G. Kotler, and H.J. Shaw, "Single Mode Fiber Optic Directional Couplers," *Electron. Lett.* 12, 18 (February 1980).
13. C.C. Matchenbacher and F.C. Fitchen, *Low-Noise Electronic Design*, John Wiley and Sons, N.Y., 1973, p. 19.
14. A. Yariv, *Introduction to Optical Electronics*, 2nd ed., Holt Rinehart and Winston, N.Y., 1976, p. 90.
15. Spectra Physics, *Model 124A Helium-Neon Gas Laser Instruction Manual*, Spectra Physics, Inc., Mountain View, Calif., 1969, p. 8.
16. R. Adler, "Interaction Between Light and Sound," *IEEE Spectrum* 42, 42-54 (May 1967).

## REFERENCES(cont'd.)

17. A. Yariv, *Quantum Electronics*, 2nd ed., John Wiley and Sons, N.Y., 1975, p. 359.
18. W.P. Mason, ed., *Physical Acoustics*, Academic Press, N.Y., 1964, pp 220-22.
19. D.A. Jackson, A. Dandridge, and S.K. Sheem, "Measurements of Small Phase Shifts Using a Single-Mode Optical-Fiber Interferometer," *Opt. Lett.* 5, 139-41 (April 1980).
20. T. Tamir, ed., *Topics in Applied Physics, Integrated Optics*, Springer-Verlag, N.Y., 1975, p. 148.
21. W.G. Driscoll, ed., *Handbook of Optics*, McGraw-Hill Book Co., N.Y., 1978, pp 17.7-17.13.
22. J.H. Cole, Naval Research Laboratory, Washington, D.C., interview, 10 March 1981.
23. F.M. Gardner, *Phaselock Techniques*, McGraw-Hill Book Co., N.Y., 1978, p. 36.
24. S.L. Selby and B. Girling, eds., *CRC Standard Mathematical Tables*, 14th ed., The Chemical Rubber Co., Cleveland, Ohio, 1964, p. 409.
25. J.L. Melsa and D.G. Schultz, *Linear Control Systems*, McGraw-Hill Book Co., N.Y., 1969, p. 154.
26. Signetics Corp., *Applications*, Signetics Corp., Sunnyvale, Calif., 1974, p. 6.
27. J.L. Melsa and D.G. Schultz, *Linear Control Systems*, McGraw-Hill Book Co., N.Y., 1969, p. 301.
28. F.M. Gardner, *Phaselock Techniques*, McGraw-Hill Book Co., N.Y., 1978, p. 42.